Shape Control of Structures and Materials
with Shape Memory Alloys

Marc van der Wijst

Shape Control of Structures and Materials with Shape Memory Alloys

Shape Control of Structures and Materials with Shape Memory Alloys

Marc Wilhelmus Maria van der Wijst

geboren te Nuenen

Dit proefschrift is goedgekeurd door de promotoren:

prof.dr.ir. H.E.H. Meijer
en
prof.dr.ir. J.J. Kok

Copromotor:
dr.ir. P.J.G. Schreurs

voor Margot

Contents

1   Introduction

1.1   Adaptive materials and structures

The increasing requirements on materials for structural applications have led to a wide variety of new high performance materials, that exhibit, for example, a high specific stiffness, strength or toughness. Especially composites, consisting of a matrix material reinforced with fibers, can be found in many industrial applications. Recently, several materials have become available with actuator and/or sensor properties. An actuator is defined here as a device that can exert a force or moment as a reaction to a (controllable) stimulus. Composites containing such materials can be provided with new and additional functions. In the most advanced form, such *smart* materials or structures incorporate sensors, actuators, and controllers to sense both imposed loads and its environment, assess its response to the imposed loads and environment, assess its own health and take corrective actions (Agnes and Sendeckyj, 1991). These corrective actions may be changing the structures shape or stiffness, suppressing undesired vibration or guiding repairs. Until now, only very few really smart structures have been developed.

    Adaptive materials and structures form a subset. They integrate load-carrying actuators into the structure, and possibly (but not necessarily) also sensors, but depend on non-structural controllers (Rogers, 1988; Stevens, 1991; Wada, 1990). A limited number of materials is capable to act as integrated sensor or actuator. Optical fibers can be applied as integrated sensor: they are able to measure force, strain, temperature, changes in chemical composition, damage etc. Piezo-electric polymers and ceramics possess both sensing and actuating properties. They deform upon application of a voltage (actuator), or generate a voltage when loaded (sensor). Mainly used as actuators are electro-rheological fluids, that react to an electric field with a significant increase of viscosity, and *shape memory alloys* (SMA's), that remember their initial shape when their temperature is raised above a specific transition value. While piezo-electric materials are active in the small deformation - high frequency area, SMA's are rather slow, but can yield large deformations.

1.1.1   The shape memory effect

This thesis focuses on the use of SMA's as actuators. SMA's are a group of metal alloys exhibiting the shape memory effect: by raising the temperature of an unconstrained, previously deformed SMA specimen, its initial shape can be regained. Strains of about 8% can be recovered this way. If the shape recovery is constrained, large recovery stresses originate
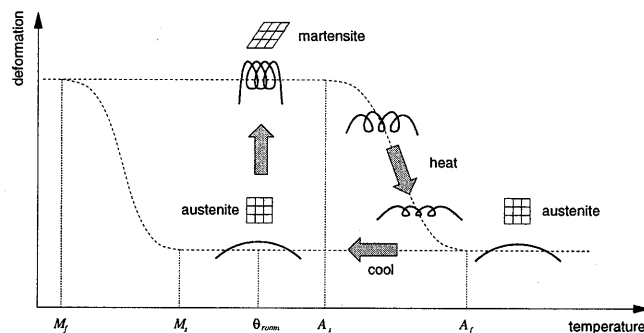
Figure 1.1: The shape memory effect

in the material, enabling the specimen to exert a high force. This makes SMA's suitable as actuators in many kinds of mechanical systems.

The behaviour of SMA's is due to a change of the microstructure, more specifically a phase transformation (Perkins, 1975; Funakubo, 1987; Duerig, 1989). The alloy used in this research was the Nickel-Titanium alloy NiTi, the most often studied and applied SMA. The principle of shape memory behaviour is explained schematically in Figure 1.1. Above a specific temperature M_s (Martensite Start temperature), the preferred crystal structure in an undeformed SMA is austenite. When the SMA is loaded, austenite transforms into martensite, a different crystal structure. This transition is accompanied by a large strain increase. If the loading takes place below a temperature A_s (Austenite Start temperature, $A_s > M_s$), martensite remains the preferred structure even after the load has been removed. The deformation remains present, but can be recovered by heating the material above A_s. Martensite starts to transform back into austenite, causing the deformation to disappear gradually. This process is completed when the temperature reaches A_f (Austenite Finish temperature). If no special treatments have been carried out on the material, cooling to a temperature above M_s has no effect: the crystal structure remains austenite. Such loading - heating - cooling cycle is repeatable for millions of times. The lifetime depends on the amount of deformation that is applied during each cycle. The shape memory behaviour is described in more detail in Chapter 2. Because of the fact that the shape memory effect only occurs during heating, it is called the One Way Memory Effect. SMA's can be 'trained' to exhibit the Two Way Memory Effect. Then martensite formation and deformation occur also during cooling when no load is applied. The SMA's used in this thesis only show the One Way Memory Effect.

1.2   Overview of SMA applications

SMA's are more and more regarded as an attractive solution for numerous problems. The number of commercial successes however is still limited. This section intends to give an idea of the applications that are already available, and that are currently subject of research.

1.2.1   Passive applications

The majority of commercial applications exploit the shape memory behaviour in a rather simple way. They utilize the shape memory effect only once for fastening, like pipe couplings for aircraft and naval hydraulic lines, and medical devices like bone plates, cervical fixtures, staples, and blood clot filters. Also applications that act in a simple on-off sense are more and more encountered. Thermal valves and safety switches find their way in automotive industry and domestic appliances. The temperature of the ambient medium is the driving force here. Externally applied heat activates the SMA's also in, e.g., greenhouse window openers and solar trackers. An overview of applications can be found in (Wayman, 1980; Jost and Hornbogen, 1989; Stöckel, 1990; Poulek, 1994; Besselink and Sachdeva, 1995; Kobayashi et al., 1995; Lipscomb and Nokes, 1996). Increased impact resistance of composite materials exploiting the energy absorption capability of SMA wires is also investigated currently (Paine, 1994).

1.2.2   Active control of SMA's

More sophisticated use of SMA's involves the possibility to actively control their temperature. Resistive heating with an electric current is the method most frequently encountered. The relatively low voltage requirements and the ability to generate large displacements (or forces) without any moving parts offer interesting possibilities in a wide range of applications. Applications that require continuous active control of the temperature are almost without exception still in the laboratory stage. An impression of research activities is given below.

Vibration control

Reduction of vibrations in structures has always been an important issue in mechanics. Lighter, more flexible constructions are more susceptible to oscillations, which often have to be eliminated as much as possible, since they can deteriorate performance and contribute to premature collapse. The feasibility of using SMA's to damp vibrations has been investigated by numerous research groups.

Baz et al. (1990), and Choi and Cheong (1996) applied SMA wires for active damping of flexural vibrations of a cantilever beam. Ikegami et al. (1990) combined SMA wires and piezoelectric ceramics. The SMA wires served both as sensors by measuring their resistance, and as actuators to damp low frequency vibrations. The piezoelectric ceramics were used to reduce high frequency vibrations. Rhee (1992), and Shahin et al. (1997), investigated the use of SMA tendons to reduce vibrations of a floor-mass structure. In all cases, a *control law* was selected to determine the electric current that is supplied to the SMA wires. Although

the results indicate that active vibration control is possible, some remarks should be made at this point. An important factor when using SMA's as actuators, that is absent in most other actuators, is the time needed for heating, and, especially, cooling. Vibrations with frequencies that are high with respect to this thermal time constant, are difficult to reduce; it just takes too much time to heat and cool the actuators. Reduction of high frequency vibrations is mainly due to the gradual temperature rise of, and therefore stress increase in the SMA wires, resulting in stiffening of the structure.

Stiffness control of SMA reinforced structures

A subject related to active vibration control is the active control of the bending stiffness of structures that are reinforced with SMA wires. Heating of the SMA wires yields large recovery stresses and increase of their elastic modulus, causing an increase of the bending stiffness and consequently also of the resonance frequencies of the structure. In this way vibration of the structure can be reduced by shifting the resonance frequencies away from the disturbance frequencies. Rogers et al. (1990, 1991), Baz and Ro (1994), Baz et al. (1995), and Bideaux et al. (1995) showed the possibility to shift resonance frequencies by heating the SMA wires embedded in a cantilever beam or plate. Saunders et al. (1991) used this method to attenuate the sound radiated by such a plate.

Active shape control

Since SMA's are not well-suited for the high frequency range, their attractiveness lies in low-frequency, or (quasi) static applications. In most of these applications it is not the main objective to reduce mechanical vibrations, but to (actively) change the configuration of a structure. This may be the geometry of an *adaptive* truss structure, the shape of a plate, wing, or antenna reflector, or (slow) motion of (a part of) a robot.

Adaptive truss structures, or variable geometry trusses, are generally very long, slender, lightweight, lightly damped, flexible constructions, that are for example used for space applications like antenna structures (Burdisso and Haftka, 1989; KrishnaKumar and Montgomery, 1992; Lammering, 1992; Lu et al., 1992; Yoshida and Umetani, 1992). Replacement of ordinary truss members by active, length-adjustable members, offers the opportunity to change the geometry of the structure by controlling the length of the active members, and to damp vibrations, which are generally of low frequency.

Embedding SMA wires in a host material in the proper way, enables control of the shape of the structure. Active shape control of such structure will be the subject of Chapter 5, and is discussed there in more detail.

Robotics

In robotics the objective is usually to have a certain point of the robot, the end-effector, follow a desired path in space, or to keep it at the same spot. The electric, pneumatic or hydraulic actuators that are used nowadays to drive robots satisfy in most cases. However, small robotic structures, like fingers of an artificial hand, require small actuators. SMA's are a

suitable solution for this kind of applications. The advantages of SMA's are their high power-to-weight ratio, silent functioning and minimum amount of moving parts, therefore reducing friction and wear. Besides, shape memory behaviour is an intrinsic property, which allows for complex actuator shapes and extreme miniaturization. In Chapter 4, a two-link robotic finger, driven by two pairs of SMA wires, will be described. Most of the literature on the use of SMA's in robotics focuses on a single SMA actuator. An overview is given in Chapter 4.

The remaining part of this section is used to give an idea of miniature applications. Ikuta (1990) developed a miniature gripper, actuated by SMA coils of about 10 mm length. Russell (1994) used a 0.3 mm thick U-shaped NiTi wire to open and close a gripper attached to a small robot. Aramaki et al. (1995) developed a tube type five-link manipulator of 1 mm in diameter, and a length of 80 mm. Experiments on position control of the tip were performed, using feedback control with strain as feedback variable. Real miniaturization was conducted by Kohl et al. (1995), who demonstrated the feasibility of cantilever beam devices made of thin NiTi sheets ($\pm 8 \mu$m), which can be used for micro-valves. Kuribayashi (1989) applied bending beams of dimensions $50 \times 500 \times 3000 \mu$m to actuate a multiple link rotary actuator. Researchers at the University of California, San Francisco, developed a silicon cantilever beam micro-gripper (thickness 12.5μm), driven by a 5 μm thick NiTi film, to position clot-inducing materials in narrow brain blood vessels (Ashley 1996).

1.3   Objectives and outline

Temperature is the driving force for SMA's. However, it is a quantity that cannot be imposed directly. Temperature depends on the amount of energy lost to the surroundings, and the energy supplied, usually by an electric current. Active control of SMA actuators in a structure implies adapting the electric currents, such that the structure takes a desired shape, an end-effector follows a desired path, a desired force is generated, etc. Numerous strategies can be selected to adapt the electric current, depending on the realized and desired motion. Each strategy results in a different *control law*. Over the years, *linear feedback* control laws have demonstrated their usefulness in a large variety of systems. However, performance can be improved in many cases, when knowledge about the system's behaviour is utilized, by including a model of the system in the control law. Examples of such *model-based control laws* can be found in for example (Slotine and Li, 1991).

Despite the successful application of model-based control strategies in many industrial systems, like robots, planes and satellites, it is a quite unexplored field of research concerning SMA actuators. The SMA actuated systems encountered in literature are almost exclusively controlled by linear feedback control laws. However, the constitutive behaviour of SMA's is highly nonlinear. It is therefore to be expected that accounting for this nonlinear behaviour will improve the performance of SMA actuators. None of the few model-based approaches that have been undertaken until now, uses a complete model of the thermo-mechanical behaviour of SMA actuators. One of the goals of this research is to apply model-based control to SMA actuators and to compare the performance with classical feedback control.

Many investigations on a single SMA actuator have been reported, discussing design rules or examining control methods. Application of SMA actuators to a mechanical system with

more than one degree of freedom, for example a robotic structure, has not been addressed extensively yet. Therefore a two-link robotic finger, driven by SMA actuators, was developed. The objective here was to investigate the ability of SMA actuators to achieve tracking control of the finger tip.

Research on active control of structures by integrated actuators is focused mainly on piezo-electric actuators. Investigations on shape control of SMA reinforced materials and structures have been restricted to the numerical and experimental determination of the shape change response to a prescribed electric current. Actual *shape control* has not been accomplished so far. The research presented in this thesis focuses on the active shape control of an SMA reinforced structure.

The thesis is organized as follows. In Chapter 2 the shape memory behaviour is explained in more detail, and a constitutive model describing the relation between stress, strain and temperature of an SMA wire is presented. Next, the control law applied for all systems in this thesis is derived. It uses an inverse model of the mechanical systems including SMA actuators. The SMA constitutive model is an important part of this inverse model.

In Chapter 3 three different SMA actuators are analyzed. SMA's usually need an external force to be deformed at a low temperature. Therefore SMA wires can in most cases not act as stand-alone actuators. The external force can be supplied either by the mechanical system (for example gravity), by a passive spring, or by another SMA wire.

Chapter 4 deals with a two-link robotic finger, driven by two pairs of SMA wires. Tracking control of the joint angles, of the finger tip and position control of the finger tip under a know disturbance load, are investigated.

Active shape control of a beam structure containing embedded SMA wires in a polypropylene matrix is the subject of Chapter 5. A finite element model has been developed to determine the shape change of the structure caused by an electric current. This model forms the model-based part of the control law. A method to measure the shape of the structure by means of a camera is described. Several time-varying shapes have been accomplished.

Chapter 6 discusses the results, with conclusions and recommendations for future research.

2   Control of SMA actuators

2.1   Introduction

Mechanical systems are actuated by actuators, the dynamics of which are often fairly simple, at least in the frequency range of interest. SMA actuators are different in two ways: first, their thermo-mechanical behaviour is complex and, second, SMA's are 'slow' actuators, meaning that their dynamics have a significant effect even for low frequencies. Therefore, the constitutive behaviour and heating dynamics of shape memory alloys play an important role in the analysis and design of mechanical systems actuated by SMA's. A constitutive model relating stress, strain and temperature must be available. It offers the opportunity to simulate the static and dynamic behaviour of SMA actuated systems. Moreover, it is an indispensable part of model-based control methods.

This chapter adresses the modeling of shape memory behaviour, and the control of SMA actuated systems. First the shape memory behaviour of a single wire is explained in more detail. Next, an overview of existing 1D and 3D constitutive models is presented. Section 2.3 discusses a one-dimensional constitutive model for a NiTi wire. Section 2.4 presents a general framework on the dynamics of the mechanical systems considered, and on the control strategy that has been selected to control these systems.

2.2   Constitutive modeling of the shape memory behaviour

The behaviour of shape memory alloys is due to a change of crystal structure from austenite to martensite and vice versa. When an austenitic SMA wire is subjected to a tensile test at a relatively low temperature (below A_s), a stress-strain curve like the left graph of Figure 2.1 is obtained. First the austenite deforms elastically. When the Martensite Start transition stress p_{ms} is reached, martensite starts to form. The martensite fraction, being the relative amount of martensite in the material, increases upon further loading. This Austenite to Martensite (AM) transformation is accompanied by a large strain increase. The AM transformation ends when the stress equals p_{mf}. Further loading results in elastic deformation of the completely martensitic wire. During unloading a different stress-strain curve is followed. After complete unloading, not all deformation has disappeared, but a transformation strain remains.
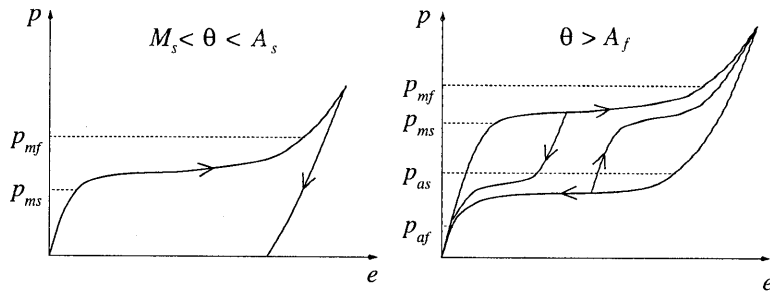
Figure 2.1: Stress-strain curves of a shape memory alloy at two temperatures

A tensile test performed at a temperature exceeding A_f yields a curve as shown in the right graph of Figure 2.1. The transformation stresses p_{ms} and p_{mf} have increased. Upon unloading from the martensitic state, the reverse Martensite to Austenite (MA) transformation starts when the stress has dropped below p_{as}. All martensite, and consequently the transformation strain, have disappeared when the stress equals p_{af}. After complete unloading the wire is austenitic. The stress-strain curve shows a closed hysteresis loop. This behaviour is referred to as *pseudoelasticity*. At temperatures below A_f (as is the case in the left graph), the reverse transformation stress p_{af} is negative, yielding a transformation strain remaining after unloading. It can be recovered by heating the martensitic specimen above A_f. This behaviour is called the Shape Memory Effect.

The right graph also shows two intermediate curves, that result when loading or unloading starts before a complete transformation has occured.

Numerous thermo-mechanical models have been proposed to capture the characteristics of shape memory alloys. Most of the models describe one-dimensional (1D) behaviour, firstly because it is less difficult than modeling 2D or 3D behaviour, secondly because the majority of SMA applications uses 1D elements like wires, and thirdly because experimental validation is easier. In this section an overview of existing 1D and 3D models is given.

2.2.1 One-dimensional constitutive models

Free energy based models

Several authors consider the transformation between austenite and martensite as free energy driven. Therefore they introduce an expression for the Helmholtz free energy. The stress, defined as the derivative of the free energy with respect to strain, is at certain temperatures non-monotonically increasing, see Figure 2.2. In these regions stress decreases with increasing strain, leading to unstable behaviour and resulting in a hysteresis. Müller (1991) derived expressions for the free energy, stress and martensite fraction as a function of strain and temperature based on micromechanics and statistics. This (complex) model is able to describe isothermal stress-strain curves both at high and low temperatures, both in tension
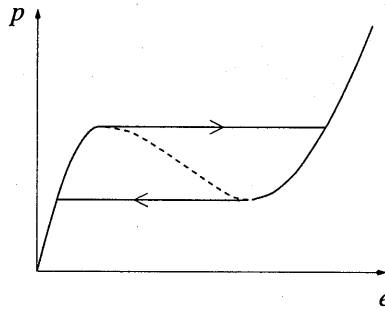
Figure 2.2: Non-monotonic stress-strain curve leading to hysteresis loop

and compression. Falk (1980) proposed a phenomenological, mathematical formula for the free energy to describe shape memory behaviour. The free energy has one minimum at high temperatures, corresponding to the austenite phase, two minima at large strains and low temperatures, corresponding to martensite in tension and compression, and three minima at intermediate temperatures, where all three phases can be present in the material. Stress influences the depth of the wells, and therefore the stability of the phases. Müller and Xu (1991), and Fu et al. (1993) focused on a CuZnAl single crystal. Their free energy consists of a set of parabolae, and therefore the stress strain curves are straight lines. Abeyaratne et al. (1994) also introduced a phenomenological expression for the free energy. Transformation is split in nucleation and growth of phases. Nucleation is assumed to take place when the stress exceeds a transformation stress. Speed of propagation of a phase boundary, i.e. growth of one phase at the expense of another, depends on the stress level. These kinetics are described by a time-dependent relation: a constant stress leads to a constant propagation speed.

The free energy based models are either too complicated, or are based on too many simplifications to be useful for practical applications.

History variable models

A second group of models uses *history* or *internal variables* to describe path dependent stress-strain curves, similar to plasticity models. While in plasticity the effective plastic strain is generally taken as an internal variable, in SMA models it is the martensite fraction m, with $0 \le m \le 1$. The one-dimensional constitutive behaviour is then given by the rate equation

$$\dot{p} = D(\dot{e} - \dot{e}^t) - D\alpha\dot{\vartheta} \tag{2.1}$$

where p represents stress, e is the total strain, e^t is the recoverable transformation strain, and ϑ the temperature. D is the elastic modulus, and α is the thermal expansion coefficient. Since e^t is the result of the formation of martensite, it is often assumed that

$$e^t = m \, e^t_{max} \tag{2.2}$$

where e^t_{max}, the maximum recoverable strain, is different for different shape memory alloys. Combining Equations (2.1) and (2.2) yields the following constitutive equation for SMA's:

$$\dot{p} = D(\dot{e} - e^t_{max}\dot{m}) - D\alpha\dot{\vartheta} \tag{2.3}$$

If the parameters D, α and e^t_{max} are constant, this equation can be integrated, yielding:

$$p = D(e - e^t_{max}m) - D\alpha(\vartheta - \vartheta_o) \tag{2.4}$$

where ϑ_o is a reference temperature. When the strain, temperature and the martensite fraction are known, the stress can be determined.

The dependence of the martensite fraction on the (rates of) constitutive variables like stress, strain and temperature must be defined with a so-called transformation kinetics relation. Such relation captures the main characteristics of shape memory behaviour, being pseudoelasticity at elevated temperatures, (quasi) permanent deformation at lower temperatures, recovery of the initial shape upon heating and the existence of a hysteresis loop. The models that use the history variable approach mainly differ in the transformation kinetics relation. Because the martensitic transformation is diffusionless, most of the models assume the martensite fraction to depend on the current value of stress and temperature only, and do not incorporate any rate dependence. The temperature has a strong effect on the transition stresses p_{ms}, p_{mf}, p_{as} and p_{af}:

$$m = m(p, p_{ms}(\vartheta), p_{mf}(\vartheta), p_{as}(\vartheta), p_{af}(\vartheta)) \tag{2.5}$$

Figure 2.3 shows schematically the dependence of the martensite fraction on stress, at two different temperatures. Also some intermediate loading and unloading curves are shown. Note that for this SMA, room temperature is between M_s and A_s (see the left curve, and compare with Figure 2.1), so that the martensite fraction does not decrease during unloading after loading (tranformation temperatures can be shifted by the manufacturer by varying the ratios of the shape memory alloy constituents).
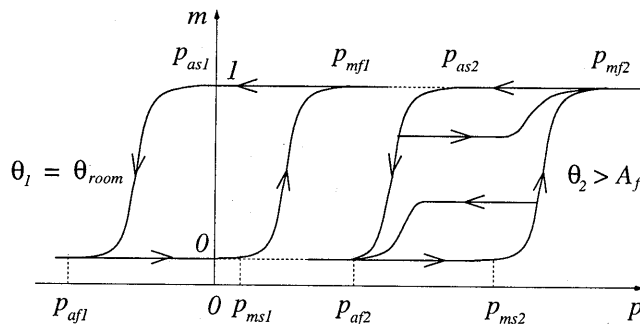
Figure 2.3: Martensite fraction vs. stress curves at two temperatures

Tanaka et al. (1986) and Tanaka (1990) introduced the exponential model, which followed from micromechanical considerations:

$$m = 1 - (1 - m_o)\exp[b_m(p - p_{ms})] \qquad \text{during AM transformation} \qquad (2.6)$$

$$m = m_o\exp[b_a(p - p_{as})] \qquad \text{during MA transformation} \qquad (2.7)$$

where m_o is the martensite fraction just before the AM or MA transformation starts. Parameters b_m and b_a depend on the transition temperatures. Based on experimental data, see e.g. Duerig (1989), a linear relationship between the transition stresses and temperature is assumed:

$$p_{ms} = c_m(\vartheta - M_s) \qquad\qquad ; \quad p_{mf} = c_m(\vartheta - M_f) \qquad (2.8)$$

$$p_{as} = c_a(\vartheta - A_s) \qquad\qquad ; \quad p_{af} = c_a(\vartheta - A_f) \qquad (2.9)$$

where c_m and c_a are constants. In subsequent papers (Tanaka, 1994; Tanaka, 1995), also a dependence of the transition stresses on m was added. Liang and Rogers (1990) modeled the transformation kinetics by a cosine function:

$$m = \frac{1 - m_o}{2}\cos[b_m(p - p_{mf})] + \frac{1 + m_o}{2} \qquad \text{during AM transformation} \qquad (2.10)$$

$$m = \frac{m_o}{2}\cos[b_a(p - p_{as})] + \frac{m_o}{2} \qquad \text{during MA transformation} \qquad (2.11)$$

They used Tanaka's linear relationships for the transition stresses. Van der Wijst and Schreurs (1993) modeled the kinetics equations by a linear relation, while Ivshin and Pence (1994) used tangent hyperbolic functions, that do not use transition stresses and temperatures as 'hard' limits for the start and finish of the evolution of m, but the parameters describing these curves are based on the transition temperatures. In their model, the transformation stresses depend non-linearly on temperature. However, for moderate temperatures linear relations similar to Equations (2.8-2.9) are valid.

Generally the material parameters of an austenitic and a martensitic specimen are different. Especially the decrease of the elastic modulus with the martensite fraction has received attention. Brinson (1993a) adapted Liang's model to include the change in elastic modulus during transformation. The elastic modulus is given by a rule of mixtures for parallel continua, such that the elastic modulus varies linearly with m from the austenitic elastic modulus D_a to the martensitic modulus D_m. Ivshin and Pence (1994) applied a series rule of mixtures. Similar relations are introduced for the expansion coefficient.

Geometrical models

Geometrical models do not include any physics, but consist of stress-strain-temperature relations that are based on fits of experimentally obtained curves. Spies (1996) approximated an isothermal stress-strain curve by straight lines. The outermost hysteresis loop is described by the stresses and strains of the four vertices, in other words, the transition stresses and strains. Paths inside the loop are parameterized by a scalar β, which only changes when the strain
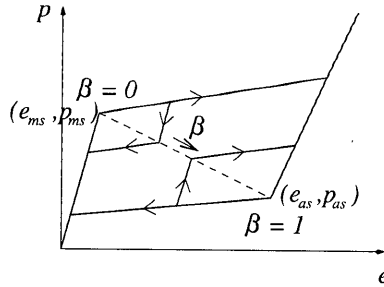
Figure 2.4: Geometric stress-strain curve

rate changes sign, see Figure 2.4. Only at these so-called *return points* a new value for β has to be determined. All paths followed inside the main loop contain an elastic part and an AM or MA transformation part. Both AM and MA transformation start when the diagonal line connecting the AM and MA starting points (e_{ms}, p_{ms}) and (e_{as}, p_{as}) is crossed. This behaviour is observed for some alloys, e.g. CuZnAl (see Fu, 1993). Unfortunately only stress-strain curves at a constant temperature are considered.

2.2.2   Three-dimensional constitutive models

Contrary to the 1D models, the development of 3D constitutive models is still in a very premature stage. Most of the 3D SMA models are either an extension of existing 1D models, or an adaptation of classical plasticity models.

Extended 1D models

Extended 1D models are generally quite simple, but fail almost without exception at the same point. Boyd and Lagoudas (1994) extended the Tanaka exponential relations (2.6-2.7) to 3D by simply replacing the 1D stress component in the martensite fraction kinetics equations by the effective (Von Mises) stress $\bar{p} = \sqrt{\frac{3}{2}\boldsymbol{P}^d : \boldsymbol{P}^d}$, with $\boldsymbol{P}^d$ the deviatoric part of the 3D stress tensor $\boldsymbol{P}$:

$$m = 1 - (1 - m_o)\exp[b_m(\bar{p} - p_{ms})] \qquad \text{during AM transformation} \qquad (2.12)$$
$$m = m_o\exp[b_a(\bar{p} - p_{as})] \qquad \text{during MA transformation} \qquad (2.13)$$

Another 3D extension of this type was proposed by Liang and Rogers (1992), who adapted their cosine relations:

$$m = \frac{1 - m_o}{2}\cos[b_m(\bar{p} - p_{mf})] + \frac{1 + m_o}{2} \qquad \text{during AM transformation} \qquad (2.14)$$
$$m = \frac{m_o}{2}\cos[b_a(\bar{p} - p_{as})] + \frac{m_o}{2} \qquad \text{during MA transformation} \qquad (2.15)$$

All models that use these kinetics laws are able to describe stress-strain curves at temperatures exceeding A_f, but fail at lower temperatures. This can be explained by a simple 1D tensile loading, unloading, and compressive loading cycle at a temperature just below A_s, see the left graph in Figure 2.3. Upon loading the effective stress $\bar{p}$ increases until it reaches the martensite start stress p_{ms1}. While the stress increases further, AM transformation advances, until the effective stress equals p_{mf1}. At this point the martensite fraction equals one. During unloading the effective stress decreases, until the SMA specimen is completely unloaded. Because the temperature is below A_s, no MA transformation has occurred yet. When the tensile loading is followed by compression, the martensite fraction should at a certain stress level $p_{as1} < 0$ start to decrease. This behaviour is observed in experiments and predicted by most of the one-dimensional models. But this is impossible with the kinetics equations of the form in Equations (2.12-2.13) and (2.14-2.15) because, although the axial stress becomes more and more negative, the effective stress increases again. Therefore the martensite fraction will never decrease during compression. This model flaw is the cause of many erroneous simulation results, as will also be explained in Chapter 5, where SMA actuators in composites are discussed. The compressive loading described here is likely to occur in SMA's that are embedded in a host material.

Plasticity based models

A second group of models is based on classical plasticity theory. In these models the onset of AM and MA transformation is governed by one or more yield criteria, that are strongly dependent on temperature. In general the yield criteria can be written as:

$$f(\boldsymbol{P}, \vartheta, m) = 0 \tag{2.16}$$

which in its simplest form is:

$$f = \bar{p} - p_y(\vartheta, m) = 0 \tag{2.17}$$

where the temperature dependence is contained in the scalar yield stress p_y. During AM transformation the yield stress p_y equals the martensite start stress p_{ms}, while during MA transformation it is equal to p_{as}. Pseudoelasticity at higher temperatures can be described with this criterion, as shown by Trochu and Qian (1997). But to obtain meaningful results at lower temperatures, the yield criterion has to be modified. A solution to this problem is the definition of a yield surface that can not only change size (isotropic hardening), but also location. The latter effect is called kinematic hardening in plasticity theory (see e.g. Atluri, 1984). The translation of the yield surface is described with a back stress tensor $\boldsymbol{V}$ and the yield function is generally written as

$$f = \sqrt{\tfrac{3}{2}(\boldsymbol{P}^d - \boldsymbol{V}) : (\boldsymbol{P}^d - \boldsymbol{V})} - p_y(\vartheta, m) = 0 \tag{2.18}$$

This approach is followed by Bondaryev and Wayman (1988), and Sun and Hwang (1993a, 1993b). The 3D model of Graesser and Cozarelli (1994) does not have such a clear link with

plasticity theory, but after some simplifications the correspondence is quite evident. Unfortunately their model does not contain temperature as an independent variable. Its influence is hidden in a few model parameters.

It may be clear that 3D modeling of the shape memory behaviour is still a largely unexplored area. Simulation and understanding of SMA's in more dimensions is still very limited due to the lack of applicable 3D models.

2.2.3   Requirements

The choice of a constitutive model depends on its purpose. Generally, a more detailed model requires more time for evaluation. When time is not a critical factor, for example in a FEM analysis, more emphasis can be put on the accuracy of the model. However, in a real-time control environment, the constitutive model may be part of a time critical loop in a control algorithm. This implies that all calculations have to be finished within a specific time period, given by the sample frequency. So from a control point of view, the complexity of the model must be limited.

Moreover, often an inverse model of the entire system, including actuators, is required. For SMA actuators this implies that stress and strain are given, and temperature must be determined. This reverse calculation on SMA's has not been encountered in literature so far. The models available in literature are either very complex, or in a form where stress and temperature are independent variables, mainly because the martensite fraction depends on them. This means that if strain and temperature, and also if strain and stress are prescribed, a solution has to be obtained iteratively, which puts a burden on computation time.

In the following section a constitutive model of the geometric type is derived. It is a trade-off between modeling accuracy and simplicity. It involves enough parameters to fit experimental curves adequately, and is able to describe the main shape memory characteristics, i.e. pseudoelasticity, shape memory effect and hysteresis loop. Both stress and temperature as unknown variables can be calculated analytically.

2.3   A one-dimensional model of shape memory behaviour

The deformation of an SMA wire is described with the Green-Lagrange strain e. The stress in the wire is represented by the 2$^{\text{nd}}$ Piola-Kirchhoff stress p. They are related to the wire length l, and the tensile force f in the wire by

$$e = \tfrac{1}{2}\left(\left(\frac{l}{l_{ref}}\right)^2 - 1\right) \quad ; \quad p = \frac{f \, l_{ref}}{A_{ref} \, l} \tag{2.19}$$

where l_{ref} and A_{ref} are the undeformed length and cross-sectional area of the wire, respectively. The choice for using the 2$^{\text{nd}}$ Piola-Kirchhoff stress and Green-Lagrange strain was originally motivated by the possibility to apply a 3D version of the constitutive model in a FEM package. The relatively large strains occuring in SMA's may result in large rotations,

which should be accounted for. For the applications described in this thesis, engineering stress and strain would satisfy as well.

Figure 2.5 shows three measured tensile curves of a NiTi wire. For modeling purposes
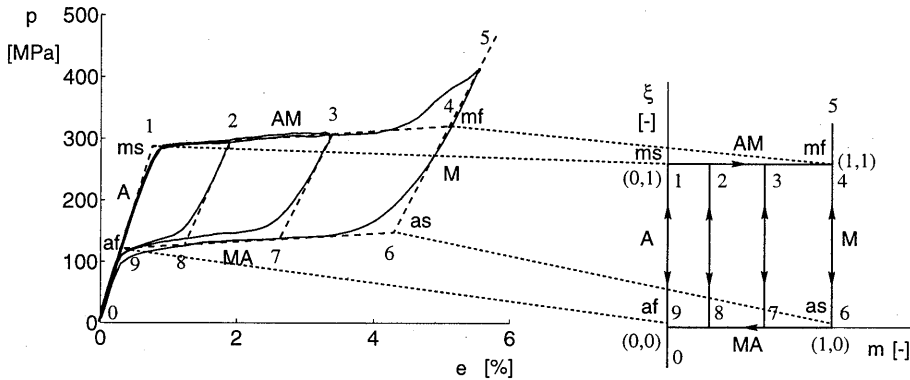
Figure 2.5: On the left: three experimentally obtained tensile curves of a NiTi wire (solid lines), and the approximating straight lines (dashed lines). On the right: alternative representation with variables m and ξ instead of e and p.

the curved lines in Figure 2.5 are approximated by straight lines. This is not a very restrictive simplification of the real behaviour, but makes the model less complicated.

The mathematical description of the SMA behaviour in terms of the stress p and the strain e is rather complicated. It can be simplified by using alternative variables. One of these variables is the martensite fraction m. The second alternative variable ξ is such that the quadrilateral with vertices 1, 4, 6 and 9 in the (e,p)-plane is mapped on a unit square in the (m,ξ)-plane.

Starting in point 0 ($m = 0$, $\xi < 0$), first the austenite deforms elastically. When the Martensite Start transition stress p_{ms} is reached (point 1, $m = 0$, $\xi = 1$), martensite starts to form ($\xi = 1$, $\dot{m} > 0$). The Austenite to Martensite (AM) transformation ends when the stress equals p_{mf} at point 4 ($m = 1$, $\xi = 1$). Further loading results in elastic deformation of the martensite ($m = 1$, $\dot{\xi} > 0$).

Unloading from point 5 does not yield the same curve as that followed during loading. The reverse MA transformation does not start until the stress has dropped to p_{as} (point 6, $m = 1$, $\xi = 0$), which is significantly lower than p_{mf}. During the MA transformation, which ends in point 9 ($m = 0, \xi = 0$), m decreases from 1 to 0. Continued unloading from point 9 results in elastic deformation of the austenite along the line through the points 9 and 0 ($m = 0, \dot{\xi} < 0$). Hence, a closed hysteresis loop occurs in such a loading cycle.

If unloading is started before the austenite has been transformed entirely into martensite ($0 < m < 1$, $\xi = 1$), e.g. in point 2 or 3, the material is unloaded elastically ($\dot{m} = 0$, $\dot{\xi} < 0$). If reloading is resumed before the lower MA side ($\xi = 0$) is reached, the same elastic path is followed ($\dot{m} = 0$, $\dot{\xi} > 0$) until the upper AM side ($\xi = 1$) is encountered. Continued

loading then involves continued AM transformation. The variables m and ξ cannot change simultaneously, i.e.

$$\dot{m}(t)\dot{\xi}(t) = 0 \quad \forall \ t \tag{2.20}$$

In fact, $\dot{m} \neq 0$ can occur only at the AM side ($\xi = 1$) and at the MA side ($\xi = 0$) of the hysteresis loop. At the AM side two situations may arise: either $\dot{m} > 0$ and $\dot{\xi} = 0$ (continued AM transformation), or $\dot{m} = 0$ and $\dot{\xi} < 0$ (elastic unloading). Similar remarks hold for the MA side. Then either $\dot{m} < 0$ and $\dot{\xi} = 0$ (continued MA transformation), or $\dot{m} = 0$ and $\dot{\xi} > 0$ (elastic loading). Summarizing:

$$\dot{m} = 0 \quad \text{unless} \quad (\xi = 1 \wedge \dot{\xi} > 0) \vee (\xi = 0 \wedge \dot{\xi} < 0) \tag{2.21}$$

The bilinear relation between the strain e and the stress p on the one hand and the alternative variables m and ξ on the other is given by

$$e = e_{af} + (e_{ms} - e_{af})\xi + (e_{as} - e_{af})m + (e_{mf} + e_{af} - e_{ms} - e_{as})\xi m \tag{2.22}$$
$$p = p_{af} + (p_{ms} - p_{af})\xi + (p_{as} - p_{af})m + (p_{mf} + p_{af} - p_{ms} - p_{as})\xi m \tag{2.23}$$

or alternatively by

$$e = e_1 + e_2\xi + e_3 m + e_4 \xi m \tag{2.24}$$
$$p = p_1 + p_2\xi + p_3 m + p_4 \xi m \tag{2.25}$$

where the definition of e_1 through p_4 is obvious.

Table 2.1: Constitutive parameters for a NiTi wire

strains			stresses		
parameter	value	unit	parameter	value	unit
e_{1a}	5.715	$\times 10^{-5} \mathrm{K}^{-1}$	p_{1a}	13.57	$\mathrm{MPa.K}^{-1}$
e_{2a}	0	$\times 10^{-5} \mathrm{K}^{-1}$	p_{2a}	0	$\mathrm{MPa.K}^{-1}$
e_{3a}	180.5	$\times 10^{-5} \mathrm{K}^{-1}$	p_{3a}	11.85	$\mathrm{MPa.K}^{-1}$
e_{4a}	0	$\times 10^{-5} \mathrm{K}^{-1}$	p_{4a}	0	$\mathrm{MPa.K}^{-1}$
e_{1b}	479.7	$\times 10^{-5}$	p_{1b}	-523.9	MPa
e_{2b}	362.1	$\times 10^{-5}$	p_{2b}	244.0	MPa
e_{3b}	-5260	$\times 10^{-5}$	p_{3b}	-466.7	MPa
e_{4b}	4514	$\times 10^{-5}$	p_{4b}	277.9	MPa

The transition strains e_{ms} through e_{af} and the transition stresses p_{ms} through p_{af} strongly depend on the temperature ϑ. It is assumed that this dependence is linear. Hence the parameters e_1 through p_4 are linear functions of temperature and can be written as

$$e_1 = e_{1a}\vartheta + e_{1b}$$

$$\vdots \qquad\qquad (2.26)$$

$$p_4 = p_{4a}\vartheta + p_{4b}$$

Experimentally obtained values for a NiTi wire are listed in Table 2.1. Figure 2.6 illustrates the constitutive model for a NiTi wire in the (e,p,ϑ)-space (left), and in the (m,ξ,ϑ)-space (right). Changes of state within the hysteresis loop are restricted to planes of constant martensite fraction. The shaded planes in Figure 2.6 represent two of these planes.
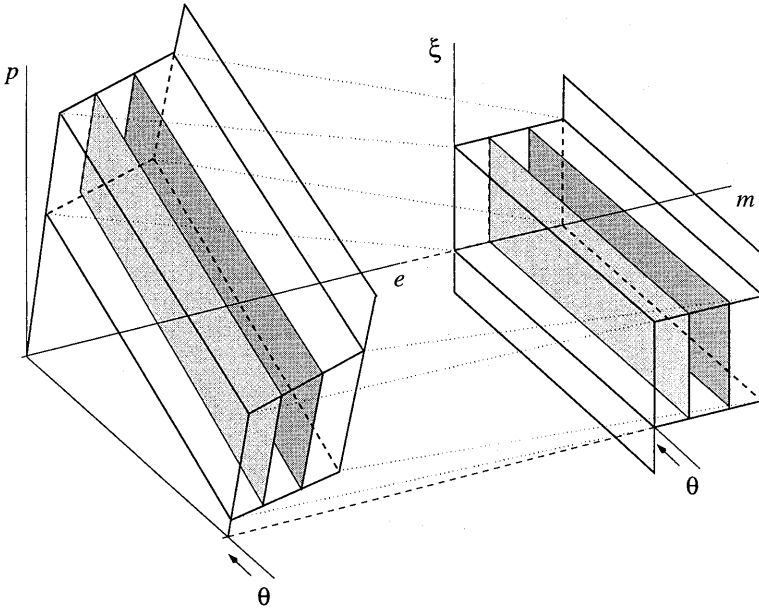
Figure 2.6: Three-dimensional representation of all possible states; on the left in (e,p,ϑ) coordinates, on the right in (m,ξ,ϑ) coordinates.

The rates $\dot{e}$ and $\dot{p}$ of respectively e and p, are related to $\dot{m}$, $\dot{\xi}$ and $\dot{\vartheta}$ by:

$$\dot{e} = e_{,m}\,(\xi,\vartheta)\dot{m} + e_{,\xi}\,(m,\vartheta)\dot{\xi} + e_{,\vartheta}\,(m,\xi)\dot{\vartheta} \qquad (2.27)$$

$$\dot{p} = p_{,m}\,(\xi,\vartheta)\dot{m} + p_{,\xi}\,(m,\vartheta)\dot{\xi} + p_{,\vartheta}\,(m,\xi)\dot{\vartheta} \qquad (2.28)$$

where $e_{,m}$ stands for the partial derivative of e with respect to m, etc. According to Equation (2.20) either $\dot{m} = 0$ or $\dot{\xi} = 0$. If $\dot{m} = 0$ then, using Equations (2.27) and (2.28), $\dot{\xi}$ and $\dot{p}$ can

be written as functions of the internal variables m, ξ and ϑ and the rates $\dot{e}$ and $\dot{\vartheta}$, resulting in

$$\dot{m} = 0 \tag{2.29}$$

$$\dot{\xi} = \frac{1}{e_{,\xi}}\dot{e} - \frac{e_{,\vartheta}}{e_{,\xi}}\dot{\vartheta} \tag{2.30}$$

$$\dot{p} = \frac{p_{,\xi}}{e_{,\xi}}\dot{e} + \left(p_{,\vartheta} - \frac{e_{,\vartheta}}{e_{,\xi}}p_{,\xi}\right)\dot{\vartheta} \tag{2.31}$$

Otherwise, if $\dot{\xi} = 0$ it is easily seen that

$$\dot{m} = \frac{1}{e_{,m}}\dot{e} - \frac{e_{,\vartheta}}{e_{,m}}\dot{\vartheta} \tag{2.32}$$

$$\dot{\xi} = 0 \tag{2.33}$$

$$\dot{p} = \frac{p_{,m}}{e_{,m}}\dot{e} + \left(p_{,\vartheta} - \frac{e_{,\vartheta}}{e_{,m}}p_{,m}\right)\dot{\vartheta} \tag{2.34}$$

If m, ξ and ϑ are known and $\dot{e}$ and $\dot{\vartheta}$ are specified then, using Equation (2.20), it can readily be decided which of these cases applies. In either case the rates $\dot{p}$, $\dot{e}$ and $\dot{\vartheta}$ are related by an equation of the form

$$\dot{p} = \pi_e \dot{e} + \pi_\vartheta \dot{\vartheta} \tag{2.35}$$

where the definition of π_e and π_ϑ for both cases is obvious.

The force f exerted by the SMA wire follows from Equation (2.19). In terms of the strain e and the stress p this force is given by

$$f = \sqrt{1 + 2e}\, p\, A_{ref} \tag{2.36}$$

Hence the rate $\dot{f}$ can be determined from

$$\dot{f} = F_e \dot{e} + F_\vartheta \dot{\vartheta} \tag{2.37}$$

where F_e and F_ϑ depend on m, ξ and ϑ and on e and f:

$$F_e = \frac{f}{1 + 2e} + \pi_e \sqrt{1 + 2e} A_{ref} \qquad ; \qquad F_\vartheta = \pi_\vartheta \sqrt{1 + 2e} A_{ref} \tag{2.38}$$

The temperature of a NiTi wire cannot be controlled directly, but is a consequence of the heat balance between stored, lost and generated power. The easiest way to heat SMA wires is by means of electric current. It is assumed that the temperature of a wire, that is not embedded in another material, satisfies (see e.g. Kreith and Bohn, 1986):

$$\tau\dot{\vartheta} + (\vartheta - \vartheta_\infty) = c\, I^2 \qquad \text{with} \qquad \tau = \frac{\rho c_p A}{H d_s} \qquad ; \qquad c = \frac{r_{el} l}{H A^2 d_s} \tag{2.39}$$

where ρ, c_p and r_{el} are the density, specific heat capacity, and specific electric resistance of NiTi respectively, A and d_s are the cross-sectional area and circumference of a wire respectively, and H is the average heat transfer coefficient, that depends on environmental circumstances. Furthermore, ϑ_∞ is the temperature of the surrounding medium, and I the electric current. The time constant τ of the thermal process is in the order of several seconds. The heat balance for embedded wires is different, and will be discussed in Chapter 5.

2.4   Control using SMA actuators

In general, a controlled (mechanical) system consists of a mechanical structure, actuators, and a controller, see Figure 2.7. Each of these parts will be discussed in this section.
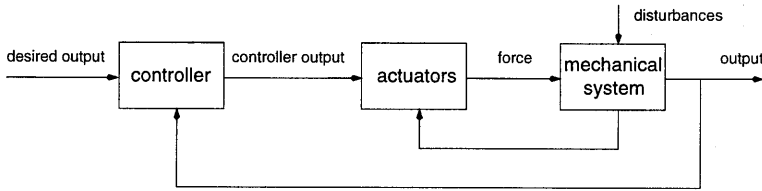
Figure 2.7: General structure of a controlled mechanical system

2.4.1   Mechanical system

In this section a general framework is presented for mechanical systems with SMA actuators. The kinematic behaviour of a (discretized) mechanical system is described with n degrees of freedom (DOF's) $q = [q_1 \ldots q_n]^T$. The dynamics are described by a set of differential equations, that relate q and the time derivates $\dot{q}, \ddot{q}$ to applied forces and/or torques. In the sequel no distinction will be made between torques and forces. The forces acting on the system are m actuator forces $f = [f_1 \ldots f_m]^T$, and (unknown) disturbance loads w. In this thesis the number of actuators is always equal to the number of DOF's, i.e. $m = n$. In general, the equations of motion read:

$$\underline{M}\ddot{q} + \underline{B}\dot{q} + g(q) = f + w \tag{2.40}$$

where $\underline{M} = \underline{M}(q)$, $\underline{M} = \underline{M}^T$ is the symmetric inertia matrix, $\underline{B} = \underline{B}(q, \dot{q})$ accounts for velocity effects, like viscous friction, centrifugal and Coriolis effects, and $g(q)$ represents elastic effects due to, e.g., springs and bending stiffness, and volume load effects like gravity. In the sequel it is assumed that the velocities $\dot{q}$ and the accelerations $\ddot{q}$ are small enough to neglect their influence in Equation (2.40). The model of the mechanical system, used as the *controller design model*, then becomes

$$g(q) = f \tag{2.41}$$

The output of the system is the column q of degrees of freedom. The desired output is given by an at least once differentiable function $q_d = q_d(t)$.

2.4.2   SMA actuators

In this thesis SMA wire actuators are applied. An important feature of SMA wires is that they can cause motion only in one direction. This restriction is due to the One Way Memory Effect and to the fact that wires cannot produce a compressive force. To obtain an actuator
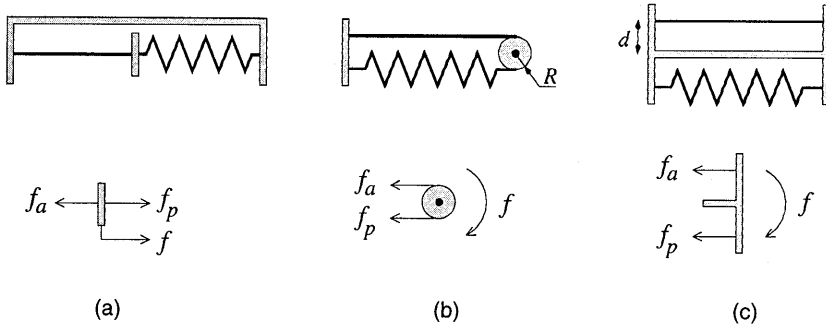
Figure 2.8: SMA actuators, consisting of an active element (SMA wire), and a passive element (spring or SMA wire), used for translation (a), rotation (b), and bending (c).

that is capable of moving in two directions, the SMA wire must be prestressed by a tensile force. This force may be exerted by the mechanical system, as is the case in the first system described in the next chapter. However, in most practical situations this is not the case, and the SMA wire must be combined with a second element, that provides the necessary tensile load. Since an SMA actuator needs a passive element to function properly, the combination of an *active* SMA wire and a *passive* element will be called *SMA actuator*. The majority of SMA actuators reported in literature use either a spring, or another SMA wire as the passive element.

Dynamics of SMA actuators

The goal of an SMA actuator is to generate a force f, that can be controlled by an input u. Depending on the design of the actuator, f can be a force, a torque, or a bending moment. The SMA actuators described in this thesis are all driven by SMA wires, that can exert tensile forces only. The actuator force f of an SMA actuator is the result of the tensile force f_a in the active SMA wire and the tensile force f_p in the passive element, and can be written as:

$$f = S(f_a - f_p) \tag{2.42}$$

Referring to Figure 2.8, $S = 1$ for the translational actuator (a), $S = R$ for the rotational actuator (b), and $S = d$ for the bending actuator (c).

The tensile force in an SMA wire depends on the wire length and its temperature. The wire length depends on the configuration (and therefore on q) of the mechanical system, so $l_a = l_a(q)$. The input u to the SMA wire actuator is the square of the electric current I through the wire.

The length of the passive element depends on q as well: $l_p = l_p(q)$. As stated before, the passive element is either a spring, or another (non-heated) SMA wire. If the element is a

spring with spring constant k_s, the spring force is

$$f_p = k_s \left(l_p(\underline{q}) - l_{s,ref} \right) \tag{2.43}$$

where $l_{s,ref}$ is the reference length of the spring. If the passive element is an unactivated SMA wire, the force is related to the temperature ϑ_p of the passive SMA wire and its length l_p.

Summarizing, the actuator dynamics of an SMA actuator consisting of an active and a passive element, are given by:

active SMA wire

$$\tau\dot{\vartheta}_a + (\vartheta_a - \vartheta_\infty) = c\,u \tag{2.44}$$

$$\dot{f}_a = F_e (\frac{\partial e}{\partial \underline{q}})^T \dot{\underline{q}} + F_\vartheta \dot{\vartheta}_a \tag{2.45}$$

passive element: SMA wire

$$\tau\dot{\vartheta}_p + (\vartheta_p - \vartheta_\infty) = 0 \tag{2.46}$$

$$\dot{f}_p = F_e (\frac{\partial e}{\partial \underline{q}})^T \dot{\underline{q}} + F_\vartheta \dot{\vartheta}_p \tag{2.47}$$

passive element: spring

$$f_p = k_s \left(l_p(\underline{q}) - l_{s,ref} \right) \tag{2.48}$$

actuator force

$$f = S(f_a - f_p) \tag{2.49}$$

Such set of equations holds for every SMA actuator in the system.

2.4.3   Controller

The main task of a controller is to obtain good tracking performance and attenuate disturbances, also in the presence of modeling errors. The contents of the controller block depend on the control strategy chosen. In general, controllers consist of two parts:

- a *feedback* or *closed loop* part: the actual q, $\dot{q}$ etc., are fed back to the controller, where they are compared with their desired values. If the control actions only depend on the tracking errors $\underline{e}_q = \underline{q}_d - \underline{q}$ and possibly their derivatives and integrals, the control is a pure feedback control. Perhaps the most widely used feedback controller is the classical PID controller. Its popularity is mainly due to its simplicity and low sensitivity to model uncertainties and disturbances. Alternative methods to design a feedback controller are for example LQG optimal control, and robust control. A (linearized) model of the mechanical system is often used off-line for the design of the controller, but the resulting control laws do not explicitly use a model of the system dynamics. However, trajectory tracking performance can be improved when knowledge about the (often non-linear) system and actuator dynamics is not ignored. Therefore often

- a *model-based* part is present in the control law as well. Many control methods are a combination of feedback and model-based control, such as computed torque control, sliding mode control, or adaptive control (see for example Slotine and Li, 1991).
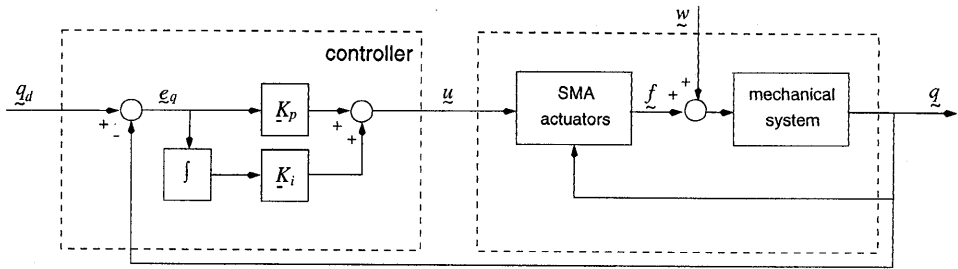
Figure 2.9: PI feedback control

A model describing the behaviour of SMA wire actuators is available. It can be used in many different ways yielding many different control laws. The model can be applied to form, e.g., a computed torque or sliding mode control law. In these methods the model is used on-line. *Measured* variables are fed into the (often non-linear) model to form the input $\underline{u}$.

The method used in this thesis is a combination of *open loop control* and PI feedback control. Open loop control alone does not require any measurement equipment, but demands an extremely precise model to be successful. Disturbances are also not accounted for. The open loop controller uses an inverse model of the mechanical system, including actuators, to approximate the control signal $\underline{u}_{ol}(t)$ necessary to follow a desired trajectory $\underline{q}_d(t)$. It is entirely based on the *desired* trajectory, and can therefore be computed off-line. Computing time is not an issue and the model can be very complex. This is the case in Chapter 5, where the temperature distribution in an SMA reinforced composite material must be determined. It is very difficult to perform such calculation on-line within one sample period. This remark does not hold for the relatively simple systems in Chapters 3 and 4. Other advanced control laws can be applied for those systems. This has not been done during this research, but is certainly recommended for future research.

In most control problems the actuators are regarded as an integral part of the system. However, this thesis discusses the use of SMA's as actuators in various mechanical systems. The emphasis is not on a specific system, but on the actuators.

Feedback control

The classical way to control a mechanical system is to adopt a control law that only uses the tracking error $\underline{e}_q$ (Proportional action), its derivative $\underline{\dot{e}}_q$ (Derivative action), and the integral $\int_0^t \underline{e}_q dt$ (Integral action), in the following way:

$$\underline{u} = \underline{K}_d \underline{\dot{e}}_q + \underline{K}_p \underline{e}_q + \underline{K}_i \int_0^t \underline{e}_q dt \qquad (2.50)$$

The derivative part adds artificial damping to the mechanical system. However, as will be demonstrated later, its effect is very small when applied to SMA actuators. Therefore in this thesis only PI control is used, with diagonal matrices $\underline{K}_p$ and $\underline{K}_i$, see Figure 2.9.
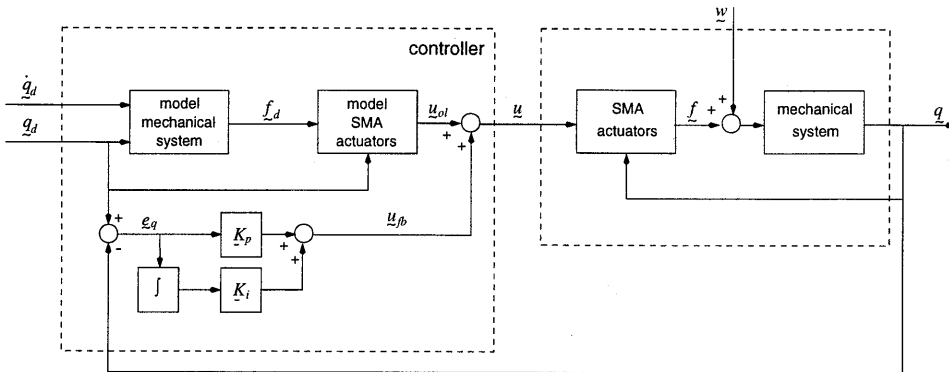
Figure 2.10: Open loop and feedback control

The most important demand on the control parameters in $\underline{K}_p$ and $\underline{K}_i$ is to guarantee system stability. Linear control theory provides guidelines to arrive at proper tuning of these parameters, see for example (Biernson, 1988; Martins de Carvalho, 1993). Since SMA actuators are strongly non-linear, the resulting model for the controlled system is non-linear and has to be linearized. The inertia and velocity terms are not neglected for the resulting linear *tuning* model, because they determine the resonance frequencies, and therefore restrict the attainable control gain. The derivation of the complete linearized model and tuning of the feedback parameters is different for every mechanical system, and is therefore performed in the concerning chapters.

Open loop control

An open loop (OL) controller determines a control input which, according to a model of the system and the actuators, guarantees perfect tracking of the desired trajectory $\underline{q}_d$, if the model is a perfect description of the system dynamics and disturbances are absent. The model is used inversely: the output $\underline{q}_d$ is known, and the input $\underline{u}_{ol}$ must be determined. Since motions are quite slow, the desired velocities $\dot{\underline{q}}_d(t)$ and accelerations $\ddot{\underline{q}}_d(t)$ are very small, and can be neglected in the determination of the open loop input. Unknown disturbances cannot be taken into account. In Chapter 4 compensation of *known* disturbance forces is applied. The desired actuator forces $\underline{f}_d$ are then:

$$\underline{f}_d = \underline{g}(\underline{q}_d) \tag{2.51}$$

The desired value of the DOF's also yields the desired force in the passive elements. This yields the required force in the active SMA wires. Since the desired force and length of the actuators are known, the desired temperature can be determined with the constitutive model. Since the heating and cooling is a first order process, the time derivatives of the variables are calculated as well. Finally, the desired or open loop input $u_{ol}(t)$ can be determined.

Summarizing, the open loop input of one actuator results from the following equations:

System dynamics

$$f_d = g(q_d) \qquad ; \qquad \dot{f}_d = (\frac{\partial g}{\partial q})^T \dot{q} \qquad (2.52)$$

Actuator dynamics

for all actuators

passive element: SMA wire

$$\tau \dot{\vartheta}_{pd} + (\vartheta_{pd} - \vartheta_\infty) = 0 \qquad\qquad\qquad (2.53)$$

$$\dot{f}_{pd} = F_e (\frac{\partial e}{\partial q})^T \dot{q}_d - \frac{F_\vartheta}{\tau}(\vartheta_{pd} - \vartheta_\infty) \qquad\qquad (2.54)$$

passive element: spring

$$f_{pd} = k_s (l_p(q_d) - l_{s,ref}) \qquad ; \qquad \dot{f}_{pd} = k_s (\frac{\partial l_p}{\partial q})^T \dot{q}_d \quad (2.55)$$

active SMA wire

$$f_{ad} = f_{pd} + S^{-1} f_d \qquad ; \qquad \dot{f}_{ad} = \dot{f}_{pd} + S^{-1} \dot{f}_d \quad (2.56)$$

$$\dot{\vartheta}_{ad} = \frac{1}{F_\vartheta} \dot{f}_{ad} - \frac{F_e}{F_\vartheta}(\frac{\partial e}{\partial q})^T \dot{q}_d \qquad\qquad (2.57)$$

$$u_{ol} = c^{-1}(\tau \dot{\vartheta}_{ad} + \vartheta_{ad} - \vartheta_\infty) \qquad\qquad (2.58)$$

The total control input is the sum of the open loop and feedback part:

$$u = u_{ol} + u_{fb} \qquad\qquad\qquad (2.59)$$

where u_{fb} is the PI controller. The two parts of this control law are clearly visible in Figure 2.10. At this point a distinction must be made between actuators consisting of an SMA wire and another element, e.g. a spring, and actuators consisting of two SMA wires, that can both be heated. In the first case the input can never be negative, because it is equal to the square of the electric current. When Equation (2.59) yields a negative input u_i for actuator i, it is set to zero. In case of two SMA wires, the sign of the input determines which wire must be heated.

Open loop part

This section presents the derivation of the open loop input u_{ol} for a single active SMA wire based on a desired force in the wire f_{ad}, as given in Equations (2.57-2.58), in detail. At this
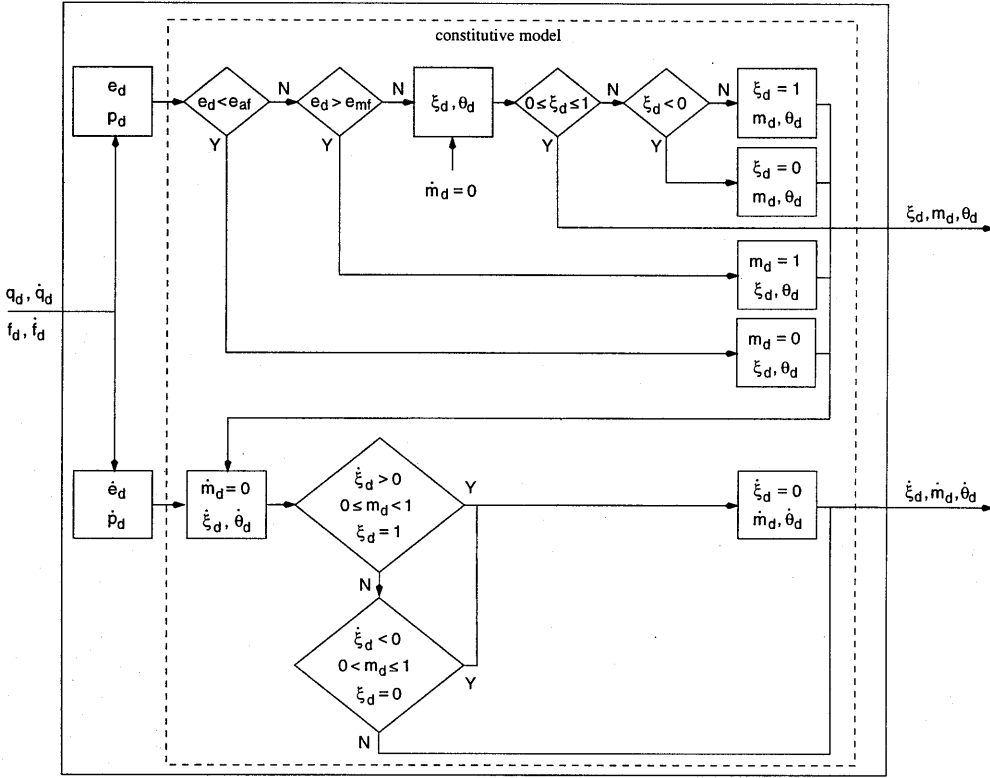
Figure 2.11: Determination of the desired state

stage it is assumed that the desired force f_{ad} is known. Figure 2.11 is a flow chart of this computation. At the initial time $t = 0$ the state of the actuator $(m_0, \xi_0, \vartheta_0)$ is assumed to be known (as will be shown later, the influence of a wrong estimate of the initial state vanishes rather quickly). Therefore also the strain e_0 and the stress p_0 are known. The desired strain $e_{ad}(t)$ and the desired stress $p_{ad}(t)$ in the active wire for $t \geq 0$ are given by

$$e_{ad} = \frac{1}{2}\left(\left(\frac{l_{ad}(\underline{q}_d)}{l_{ref}}\right)^2 - 1\right) \qquad ; \qquad p_{ad} = \frac{f_{ad}\, l_{ref}}{A_{ref}\, l_{ad}(\underline{q}_d)} \tag{2.60}$$

Since the open loop input requires the temperature rate, the desired strain and stress derivatives are also calculated:

$$\dot{e}_{ad} = \frac{l_{ad}}{l_{ref}^2}\left(\frac{\partial l_a}{\partial \underline{q}}\right)^T \dot{\underline{q}}_d \qquad ; \qquad \dot{p}_{ad} = \frac{l_{ref}}{A_{ref} l_{ad}^2}\left(l_{ad}\dot{f}_{ad} - f_{ad}\left(\frac{\partial l_a}{\partial \underline{q}}\right)^T \dot{\underline{q}}_d\right) \tag{2.61}$$

The subscript a will be omitted in the following for clarity. Substitution of these relations in Equations (2.27-2.28) results in two equations for the three unknown rates $\dot{m}_d$, $\dot{\xi}_d$ and $\dot{\vartheta}_d$,

with the condition $\dot{m}_d(t)\dot{\xi}_d(t) = 0$ for all $t \geq 0$. The desired state $\left(m_d(t), \xi_d(t), \vartheta_d(t)\right)$ for $t \geq 0$ can be determined by (numerical) integration. The adopted integration algorithm is based on the fact that $\dot{m}_d$ can be unequal to 0 only if $0 \leq m_d < 1$ and $\xi_d = 1$ or if $0 < m_d \leq 1$ and $\xi_d = 0$. Hence in each step of the integration algorithm it is assumed first that m_d remains constant. Then ξ_d and ϑ_d are solved from Equations (2.24-2.26). Next it is checked whether or not the assumption $\dot{m}_d = 0$ is justified; the assumption has to be rejected if $\xi_d \notin [0,1]$: this implies that the AM or MA boundary is encountered, and $\xi_d = 0$ or $\xi_d = 1$; m_d and ϑ_d then follow from Equations (2.24-2.26).

The temperature rate $\dot{\vartheta}_d$ is determined in a similar way. Assuming $\dot{m}_d = 0$, Equations (2.27-2.28) yield

$$\dot{\vartheta}_d = \frac{p_{,\xi}\,\dot{e}_d - e_{,\xi}\,\dot{p}_d}{p_{,\xi}\,e_{,\vartheta} - e_{,\xi}\,p_{,\vartheta}} \qquad ; \qquad \dot{\xi}_d = \frac{p_{,\vartheta}\,\dot{e}_d - e_{,\vartheta}\,\dot{p}_d}{p_{,\vartheta}\,e_{,\xi} - e_{,\vartheta}\,p_{,\xi}} \tag{2.62}$$

If the present state is either on the AM ($\xi_d = 1$) or on the MA boundary ($\xi_d = 0$), the assumption $\dot{m}_d = 0$ may not be correct. If either $0 \leq m_d < 1$, $\xi_d = 1$ and $\dot{\xi}_d > 0$, or, $0 < m_d \leq 1$, $\xi_d = 0$ and $\dot{\xi}_d < 0$, AM and MA transformation respectively takes place, which means that $\dot{m}_d \neq 0$, and at the same time that $\dot{\xi}_d = 0$. In that case $\dot{\vartheta}_d$ and $\dot{m}_d$ read

$$\dot{\vartheta}_d = \frac{p_{,m}\,\dot{e}_d - e_{,m}\,\dot{p}_d}{p_{,m}\,e_{,\vartheta} - e_{,m}\,p_{,\vartheta}} \qquad ; \qquad \dot{m}_d = \frac{p_{,\vartheta}\,\dot{e}_d - e_{,\vartheta}\,\dot{p}_d}{p_{,\vartheta}\,e_{,m} - e_{,\vartheta}\,p_{,m}} \tag{2.63}$$

With this algorithm, which resembles very much the well established integration algorithms for elastic-plastic material behaviour (Bathe, 1982), the desired temperature $\vartheta_d(t)$ and desired temperature rate $\dot{\vartheta}_d(t)$ can be determined for all $t \geq 0$. Finally, the open loop part of the input u_{ol} follows from the thermal equation (2.39):

$$u_{ol} = c^{-1}\left(\tau\,\dot{\vartheta}_d + \vartheta_d - \vartheta_\infty\right) \tag{2.64}$$

Figure 2.12 is an illustration of this procedure. A sawtooth trajectory is chosen for $q_d(t)$ (top left). The desired temperature $\vartheta_d(t)$ (middle), the desired temperature rate $\dot{\vartheta}_d(t)$ (bottom left), and the open loop input (bottom right) are shown. The desired temperature rate has a small value during AM or MA transformation, (Equation 2.63), e.g. between points 2 and 3, while the opposite is true during elastic deformation within the hysteresis loop (Equation 2.62), between points 1 and 2, and 3 and 4 respectively (dashed line). Upon switching from (2.63) to (2.62) and vice versa a large discontinuous step is encountered. As a result also the desired electric power changes discontinuously at these moments. This is a useful effect at the start of elastic deformation, i.e. at points 1 and 3, because the hysteresis loop is crossed faster this way and a higher response speed can be achieved. However, when the opposite side of the hysteresis loop is reached and AM or MA transformation starts, i.e. at points 2 and 4, a similar, opposite step in the electric power occurs. Such a sharp change is undesirable at these points because in reality the transition from elastic to transformation response is rather smooth. A sharp change in electric power then has a negative effect on the tracking error, because an SMA wire will contract or elongate very quickly as response to such a sudden change in electric current. To obtain a more gradually varying power at the start of AM and
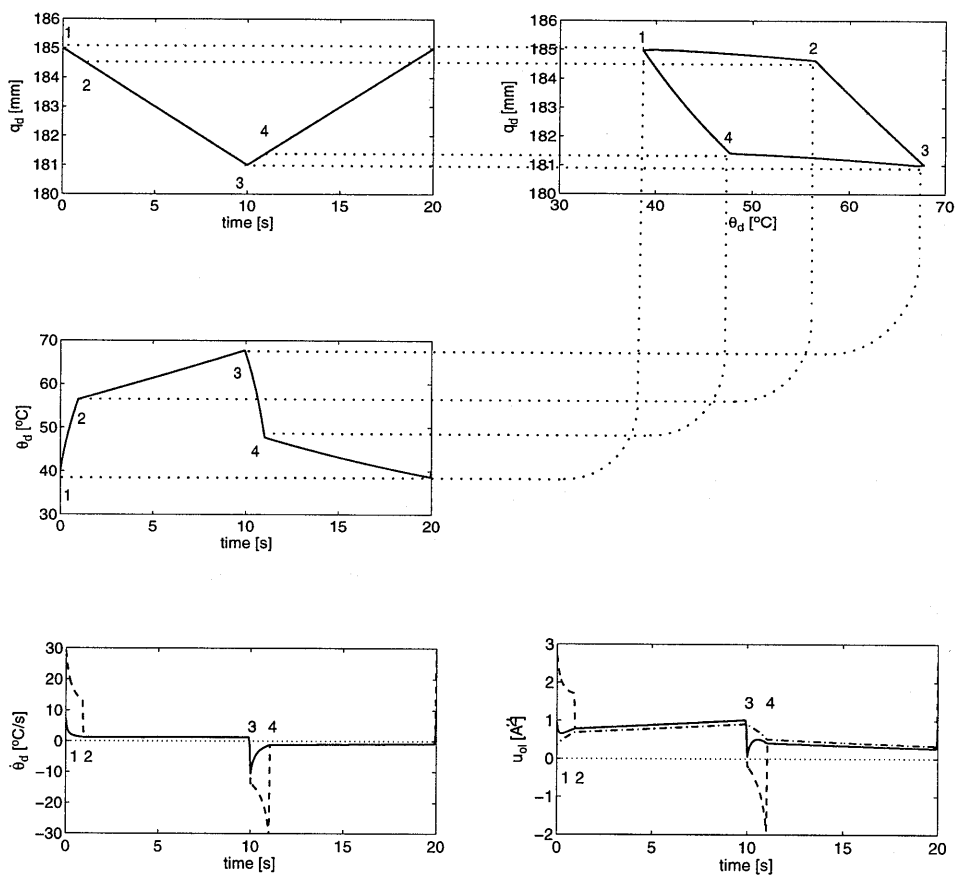
Figure 2.12: Desired trajectory (top, left); desired temperature (middle); desired temperature rate (bottom, left): with (solid), and without (dash) modification; open loop input (bottom, right): without (dashdot), with unmodified (dash) and modified (solid) temperature rate

MA transformation, the expression (2.62) for the desired temperature rate within the hysteresis loop is modified by means of linear interpolation, such that at the start of elastic deformation (2.62) is valid, and at the end (2.63):

$$\dot{\vartheta}_d = a \, \frac{p_{,\xi} \, \dot{e}_d - e_{,\xi} \, \dot{p}_d}{p_{,\xi} \, e_{,\vartheta} - e_{,\xi} \, p_{,\vartheta}} + (1 - a) \, \frac{p_{,m} \, \dot{e}_d - e_{,m} \, \dot{p}_d}{p_{,m} \, e_{,\vartheta} - e_{,m} \, p_{,\vartheta}} \tag{2.65}$$

with

$$a = \left\{ \begin{array}{ll} \xi & \text{if } \dot{\xi} < 0 \\ 1 - \xi & \text{if } \dot{\xi} > 0 \end{array} \right. \tag{2.66}$$

The solid line in Figure 2.12 (bottom, left) shows the desired temperature rate calculated using Equation (2.65) instead of (2.62). The solid line in Figure 2.12 (bottom, right) represents the corresponding electric power. The sharp changes at points 2 and 4 have disappeared, while at points 1 and 3 they are still present. The peaks completely disappear when the temperature rate is very small, i.e. in a quasi-static situation, see the dashdot line.

It now remains to explain what the forces in the passive elements are. For a spring, this is straightforward by inserting q_d in Equation (2.43). However, if the passive element is an SMA wire as well, the SMA constitutive model has to be used. The difference with the active SMA wire is, that now strain and temperature (rates) are input variables, and stress (rate) has to be calculated. Exactly the same procedure as described above can be applied, by just interchanging ϑ and $\dot{\vartheta}$ with respectively p and $\dot{p}$. The resulting force (rate) in the passive wire then follows immediately from Equations (2.60-2.61).

In practice the controlled system is a sampled data system. Let $f_s = 1/\Delta t$ be the sample frequency. It is assumed that Δt is small compared to the time constant τ of the thermal process. The input is constant per sample interval (zero order hold). In each sample interval, say the interval from $t = t_i$ to $t = t_{i+1} = t_i + \Delta t$, $\vartheta_d(t_{i+1})$, $m_d(t_{i+1})$ and $\xi_d(t_{i+1})$ and their rates $\dot{\vartheta}_d(t_{i+1})$, $\dot{m}_d(t_{i+1})$ and $\dot{\xi}_d(t_{i+1})$ are calculated, using the outlined integration algorithm.

The control strategies discussed in this chapter have been applied to several mechanical systems actuated by NiTi wires. The results of these investigations are the subject of the next chapters.

2.5   Conclusions

A control law for the input of SMA wire actuators is presented. The input consists of a feedback and a model-based open loop part, taking into account the stress-strain-temperature behaviour of an SMA wire, as well as the heating and cooling process. For this purpose a constitutive model is developed that matches the experimentally observed behaviour adequately, yet requires little computational effort.

3 Experimental evaluation of three SMA actuators

3.1 Introduction

In this chapter three different translational SMA actuators are investigated. As explained in the previous chapter, the active SMA wire must always be prestressed by a tensile force. In the first case, the weight of a mass provides the necessary force. In the second case, a spring serves as the passive element. The third actuator consists of two counteracting SMA wires, that can both be active and passive.

3.2 Case 1: Mass and SMA wire

The considered system consists of a rigid body with weight Mg, suspended by a NiTi wire (see Figure 3.1, left). The weight of the body is such that the wire is fully martensitic ($m = 1$) at room temperature. Upon heating MA transformation and shortening of the wire occurs. Temperature changes in the wire affect its length, and therefore the vertical position q of the body, which is equal to the elongation of the wire $l - l_{ref}$ (see Figure 3.1, right). The reference length l_{ref} is defined as the length of the unloaded, austenitic wire ($m = 0$) at room temperature. Since the weight provides the required tension in the wire, there is no need for a passive element. Following the general definitions in the previous chapter, we have $\underline{M} = M$, $\underline{B} = b$, $\underline{g} = -Mg$, $S = -1$ and $\underline{f} = -f_a$. The equation of motion (see Equation 2.40) of this system reads:

$$M\ddot{q} + b\dot{q} - Mg = -f_a \tag{3.1}$$

Since there is no passive element, the subscript a will be omitted in the following.

Actuator dynamics are quite simple in this case:

$$\tau\dot{\vartheta} + (\vartheta - \vartheta_\infty) = c\,u \tag{3.2}$$

$$\dot{f} = k_e\dot{q} + k_\vartheta\dot{\vartheta} \tag{3.3}$$
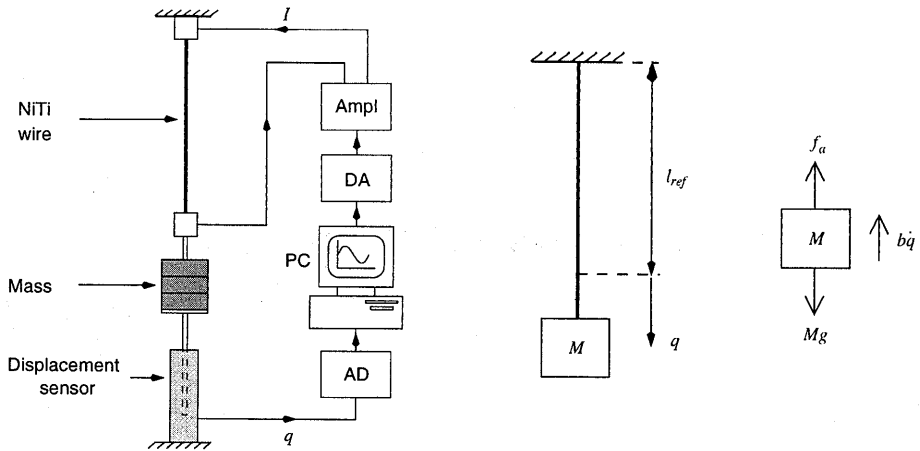
Figure 3.1: Mass attached to NiTi wire

where the moduli $k_e(m, \xi, \vartheta) = F_e(\partial e/\partial q)$ and $k_\vartheta(m, \xi, \vartheta) = F_\vartheta$ have been introduced (for the definition of F_e and F_ϑ see Equation 2.38). The strain $e(t)$ and the stress $p(t)$ corresponding to a position $q(t)$ follow from

$$e(t) = \tfrac{1}{2}\big(\big(\frac{q(t) + l_{ref}}{l_{ref}}\big)^2 - 1\big) \quad ; \quad p(t) = \frac{f\, l_{ref}}{A_{ref}(q(t) + l_{ref})} \tag{3.4}$$

At $t = 0$ the system is at rest. The elongation of the wire is $q_o = q(t = 0)$. The initial strain e_o and stress p_o at $t = 0$ are determined with Equation (3.4). The temperature is also known: $\vartheta_o = \vartheta_\infty$. The initial values for m_o and ξ_o can be calculated with the relations (2.24-2.26).

3.2.1 Controller

The control objective is to force the position q to follow a specified desired trajectory $q_d = q_d(t)$. This can only be achieved by changing the temperature of the wire, either actively or passively. In the first case the input $u = I^2$ differs from zero and, apart from current limitations, any temperature rate $\dot\vartheta$ greater than or equal to $-(\vartheta - \vartheta_\infty)/\tau$ can be realized. Passive control corresponds to $I = 0$, i.e. $u = 0$, and thus $\tau\dot\vartheta = -(\vartheta - \vartheta_\infty)$. It is impossible to realize any $\dot\vartheta$ smaller than $-(\vartheta - \vartheta_\infty)/\tau$.

The position q is measured by a Linear Variable Differential Transformer (LVDT), and converted to a digital value by a 12 bits AD converter, with a resolution of $6\mu m$. An AT 386 PC equipped with a PCL718 data acquisition card calculates the input $u = I^2$. The obtained value for I is converted to an analog signal, and transmitted to a servo amplifier. The resolution for the current is 0.5 mA. The maximum current I_{max} is 1.0 A. The software package Matlab (Matlab, 1994) is used for pre- and postprocessing. The on-line software is written in C in a TCE toolbox environment (TCE, 1994). This toolbox provides modules

for timing, communication with AD and DA cards, fetching of measurements and output of commands.

Open loop part

The inverse model of this system, neglecting higher order dynamics, see Equations (2.52-2.58), reads:

System dynamics

$$f_d = Mg \qquad ; \qquad \dot{f}_d = 0$$

Actuator dynamics

$$\dot{\vartheta}_d = -\frac{k_e}{k_\vartheta}\dot{q}_d$$

$$u_{ol} = c^{-1}(\tau\dot{\vartheta}_d + \vartheta_d - \vartheta_\infty) \qquad\qquad (3.5)$$

By means of Equation (3.4) every (e, p, ϑ) state can be transformed to a point in the (q, f, ϑ)
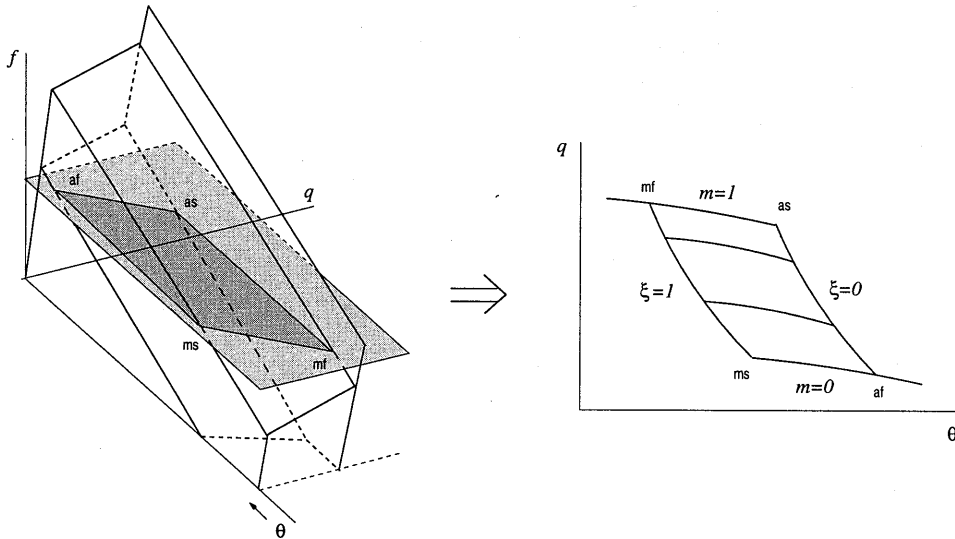

Figure 3.2: On the left: (ϑ, q, f) state space of an SMA wire, the plane of constant force Mg (light gray), and the intersection (dark gray). The intersection yields the hysteresis loop on the right

domain. Since the desired force in the wire is constant, the possible (q, f, ϑ) states are re-

stricted to a plane of constant force, that is the intersection of the three-dimensional SMA hysteresis loop in the (q, f, ϑ) domain and the plane $f = Mg$, as visualized in Figure 3.2. The dark gray area in the left figure is the intersection plane, resulting in the (ϑ, q) hysteresis on the right. Computation of the desired temperature and open loop current is performed following the rules given in the previous chapter.

Feedback part

The feedback part of the controller is based on a PI control law:

$$u_{fb} = -K_p e_q - \frac{K_p}{\tau_i} \int_0^t e_q \, dt \qquad (3.6)$$

where $e_q = q_d - q$ is the tracking error and $K_i = K_p/\tau_i$ the integral action parameter. As mentioned in the previous chapter, linear control theory provides guidelines for tuning of the controller parameters K_p and τ_i. However, the behaviour of SMA actuators is highly non-linear, and is linearized first. The non-linear behaviour is present in the moduli $k_e(m, \xi, \vartheta)$ and $k_\vartheta(m, \xi, \vartheta)$ in Equation (3.3), or alternatively in $\pi_e(m, \xi, \vartheta)$ and $\pi_\vartheta(m, \xi, \vartheta)$ in in Equation (2.35). A linearized model is obtained by assuming that both moduli are constant. The
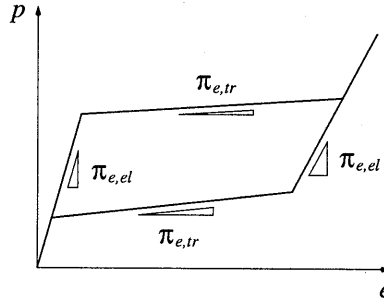
Figure 3.3: Isothermal stress-strain curve demonstrating the strong dependence of the momentary stiffness π_e on the state

moduli depend strongly on the state, and are very different during elastic behaviour ($\dot{m} = 0$) and transformation ($\dot{\xi} = 0$) respectively. Large values for $\pi_{e,el}$ and small values for $\pi_{\vartheta,el}$ occur during an elastic response of the wire, while small values for $\pi_{e,tr}$ and large values for $\pi_{\vartheta,tr}$ are found during transformation, see also Figure 3.3. Therefore two extreme cases are considered. The states where the maximum and minimum value of π_e and π_ϑ occur in the domain ($0 \leq m \leq 1, 0 \leq \xi \leq 1, 20°C \leq \vartheta \leq 100°C$) have been selected, and the values of the moduli at these states are used to construct two linearized models, and are listed in Table 3.2. Substitution of these two sets of (constant) moduli in Equation (3.3) results in two linearized SMA models, one describing elastic, the second transformation behaviour. The two linearized models give rise to different controller settings.

Table 3.2: Linearized constitutive parameters of NiTi wire

parameter	value		unit
	elastic	transformation	
π_e	16.4	2.9	GPa
π_ϑ	1.5	6.5	MPa.K^{-1}

To facilitate the tuning of the controller, analysis is usually not performed in the time domain, but in the frequency domain, by Laplace transformation of all variables. Then, input variables are related to output variables by an algebraic relation. The (linearized) relation between input $u(t)$ and output $q(t)$ can be derived by combining Equations (3.1), (3.2) and the linearized SMA model in Equation (3.3). The resulting third order differential equation is in the Laplace domain described as:

$$\frac{Q(s)}{U(s)} = \frac{ck_\vartheta}{(\tau s + 1)(Ms^2 + bs + k_e)} = G_s(s) \tag{3.7}$$

where $U(s) = \mathcal{L}\{u(t)\}$, $Q(s) = \mathcal{L}\{q(t)\}$ and $\mathcal{L}\{\cdot\}$ is the Laplace operator. When $k_{e,el}$ and $k_{\vartheta,el}$ are substituted, this transfer function represents elastic behaviour and is referred to as $G_{s,el}(s)$. Likewise, $G_{s,tr}(s)$ corresponds with transformation behaviour. Figure 3.4 shows bode plots of $G_{s,el}(s)$ and $G_{s,tr}(s)$. The effect of the thermal time constant $\tau = 4.0$ s is visible at $\omega = 0.25$ rad/s. Two differences between $G_{s,el}(s)$ and $G_{s,tr}(s)$ can be observed. First, the response of q to a low frequency sinusoidal input u is much smaller in the elastic regions, as expected. Second, the resonance frequency in the elastic regions is 61 rad/s, while it is only 25 rad/s during transformation. The feedback control law (3.6) can be described similarly:

$$\frac{U(s)}{E_q(s)} = K_p \frac{\tau_i s + 1}{\tau_i s} = G_c(s) \qquad ; \qquad E_q(s) = \mathcal{L}\{q_d(t) - q(t)\} \tag{3.8}$$

The *closed loop* transfer function $G_{cl}(s)$ of the entire controlled system relates the output $Q(s)$ to the desired signal $Q_d(s)$:

$$\frac{Q(s)}{Q_d(s)} = \frac{G_c(s)G_s(s)}{1 + G_c(s)G_s(s)} = G_{cl}(s) \tag{3.9}$$

Figure 3.5 shows the transfer functions in a block diagram. To obtain good tracking behaviour, $q(t)$ should be as close as possible to $q_d(t)$. This implies that the controller, i.e. $G_c(s)$, must be designed such that the closed loop transfer function $G_{cl}(s)$ is close to 'unity' up to a certain frequency. Additional demands on the controller are, that it must ensure the desired performance in the presence of modeling errors, it must have good stabilizing properties
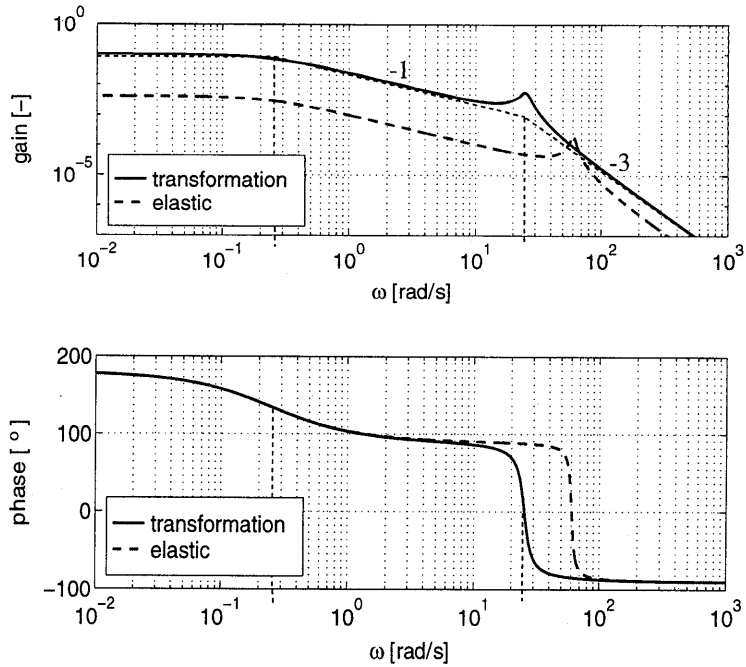
Figure 3.4: Bode plot of elastic and transformation transfer functions of mass-SMA system

and show good disturbance reduction. The controller parameters that have to be tuned to obtain the desired tracking behaviour, are the control gain K_p, and the integral time constant τ_i. Generally, increasing the control gain yields better tracking performance at higher frequencies, and better reduction of disturbances. However, the control gain must remain bounded in order to keep the system stable. Stability criteria that yield an upper bound for the control gain are the gain margin and the phase margin. The gain margin indicates how much the control gain must be raised to achieve an unstable system, i.e. to make $G_c(j\omega)G_s(j\omega)$ pass through point $-1 + 0j$ in the complex plane. The phase margin is the phase difference
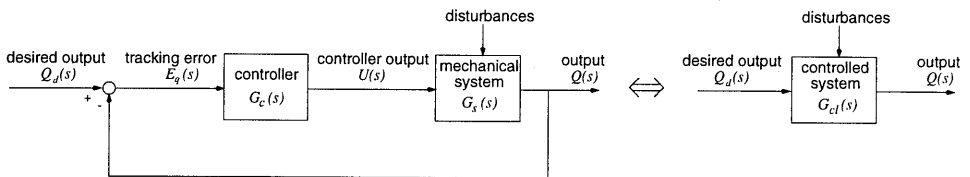
Figure 3.5: Block diagram of a feedback controlled mechanical system

between $-1 + 0j$ and the phase of $G_c(j\omega)G_s(j\omega)$ when its magnitude equals one. Sufficient robustness to modeling errors is generally achieved for a gain margin of 2.5, and a phase margin of 45°. Figure 3.6 shows the Nyquist plot of the transfer function $G_c(j\omega)G_{s,el}(j\omega)$.
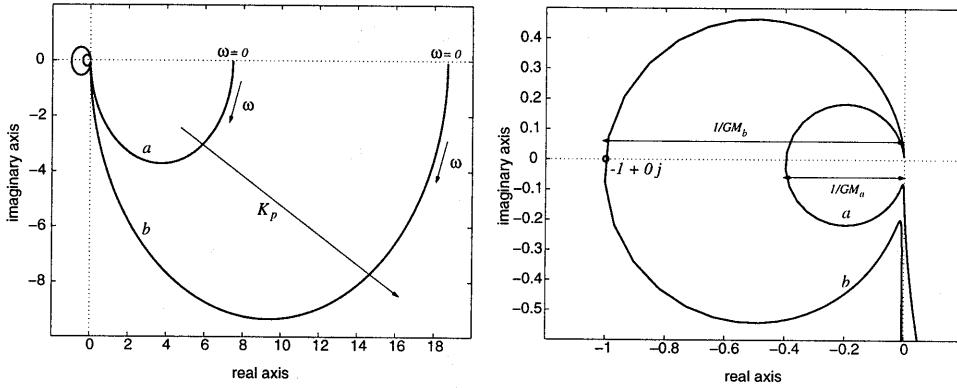
Figure 3.6: Nyquist plot of transfer function $G_c(j\omega)G_{s,tr}(j\omega)$ for two control gains K_p. The achieved gain margins are $GM_a = 2.5$ and $GM_b = 1$.

Frequency ω increases along the graphs. The distance from a point on one of the graphs to the origin is the magnitude $|G_c(j\omega)G_{s,el}(j\omega)|$ corresponding to the frequency in that point, and the angle between that point and the positive real axis is the phase lag. Two transfer functions are shown. Graph a corresponds to a gain yielding a gain margin of 2.5, while graph b passes through $-1 + 0j$, and is therefore on the verge of stability. For all systems described in this thesis the gain margin is the limiting factor, and a gain margin of 2.5 is aimed at. For the present system, this criterion is met for $K_p = 1800$ A^2/m for the elastic transfer function, but already at $K_p = 72$ A^2/m for the transformation transfer function. To have a stable system also during transformation, this last value must be used. The integral term of the control law serves to avoid a steady state position error. If the integral action is increased too much (by decreasing τ_i), the gain or phase margin may become too small. Therefore, the integral time constant is taken equal to the thermal time constant. This way the phase lag introduced by the integral action does not influence the gain margin.

For control of mechanical systems it is common practice to add a derivative action to enhance damping. Generally the upper limit of the control gain before the gain margin is reached can be increased this way. However, the presence of first order dynamics, in combination with a resonance frequency, causes a derivative action to be useless in this respect. Figure 3.7 explains why. It is a Nyquist plot of $G_{s,tr}(j\omega)G_c(j\omega)$ in the neighbourhood of $-1 + 0j$, showing the influence of increasing the derivative action. In contrast with second order mechanical systems, it is impossible to increase stablity. A larger value for τ_d yields an increase of the gain margin, but at the same time a decrease of phase margin. For even small values of τ_d the phase margin becomes the limiting factor concerning stability. The control gain can hardly be increased with a derivative action in the feedback loop. Therefore only a PI control law is applied for all systems in this thesis.

Figure 3.7: Nyquist plot of $G_c(j\omega)G_{s,tr}(j\omega)$ in the neighbourhood of -1, showing the effect of a derivative action

Figure 3.8 shows the gain and phase plot of the closed loop transfer function $G_{cl}(j\omega)$, for the elastic and for the transformation case. The closed loop bandwidth ω_b is defined as

Figure 3.8: Bode plot of closed loop elastic and transformation transfer functions
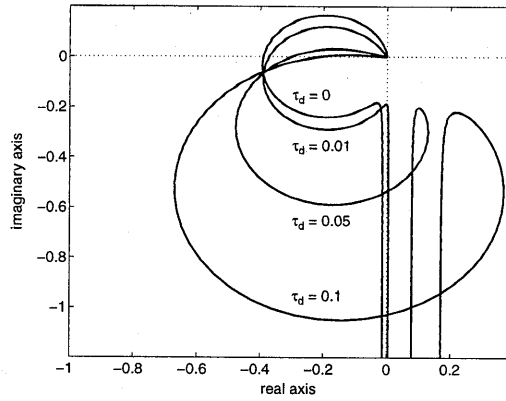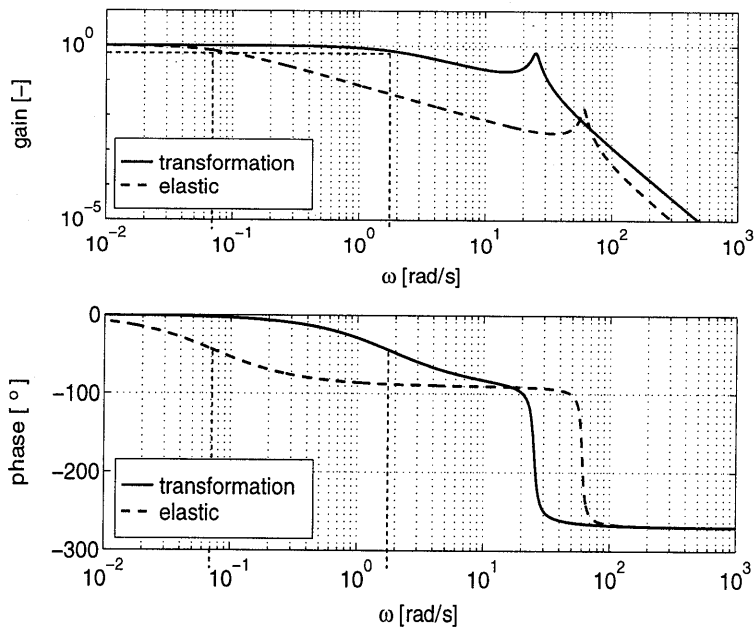
the frequency where the closed loop gain $|G_{cl}(j\omega)|$ has dropped 3 dB (or $1/\sqrt{(2)}$) below its steady state value. It indicates up to what frequency sinusoidal signals can be followed with reasonable accuracy. When signals with a higher frequency must be followed, large tracking errors occur. The closed loop bandwidth is 1.8 rad/s for $G_{s,tr}$, but only 0.07 rad/s for $G_{s,el}$. This clearly indicates one of the problems concerning control of SMA actuators. During AM and MA transformation, signals in the order of 1 rad/s can be followed. However, during crossing of the hysteresis, the gain at this frequency is -23 dB. So either command signals in the order of 0.01 rad/s must be supplied at maximum, or the amplitude of the trajectory to be followed must be kept so small, that motion is restricted to the elastic domain. In that case the control gain can be raised tremendously; applying the previously derived gain of 1800 A^2/m yields a bandwidth of 1.8 rad/s.

To prevent the integral action from excessive build up, an anti-windup mechanism (Martins de Carvalho, 1993) is introduced: the integral part is not allowed to change when the electric power is very large.

In practice the controlled system is a sampled data system, with sample frequency $f_s = 1/\Delta t = 20$ Hz. The sample frequency was chosen as high as possible, with the time necessary to compute the control input being the limiting factor. The input is constant during one sample period (zero order hold). Trajectories are restricted to frequencies below 0.2 Hz, to avoid saturation of the electric current. The selected sample frequency of 20 Hz is therefore more than sufficient. The phase lag introduced by the sampling time delay at 0.2 Hz is 0.03 rad (see e.g. Martins de Carvalho, 1993), and has therefore hardly any detrimental effect on system stability.

3.2.2   Results

The system in Figure 3.1 has been investigated both numerically and experimentally. Simulations have been performed with MATLAB. In the experiments MATLAB is used for the off-line computations during pre- and postprocessing, while the actual controller is implemented in C-code. The setup of the programs was the same for both cases. The values of the system parameters are listed in Table 3.3. The value for the damping coefficient b was obtained during free elastic vibration. The control gain used during the experiments is significantly higher than the theoretical value. A possible cause for this large difference is the fact that the theoretical gain margin depends heavily on the height of the resonance peak of the transformation transfer function $G_{s,tr}(s)$. The peak height depends on the amount of damping, and on the resonance frequency: a higher resonance frequency has a lower peak, because of the -20dB/decade roll-off rate caused by the first order thermal behaviour. The resonance frequency depends on the mass, which can be measured accurately, and the stiffness of the SMA wire during transformation. This value follows from the constitutive model, and is a 'worst case' value. It is the smallest stiffness, that according to the constitutive model, can occur. In practice, the SMA wire often experiences a higher stiffness, yielding a higher control gain.

Table **3.3**: System and control parameters

system			controller			
parameter	value	unit	parameter	calculated	used	unit
l_{ref}	178.5	mm	K_p	72	800	$A^2.m^{-1}$
A_{ref}	0.06	mm^2	τ_i	4.0	1.0	$A^2.m^{-1}.s^{-1}$
M	1.63	kg	I_{max}		1.0	A
b	7	$N.s.m^{-1}$	f_s		20.0	Hz
τ	4.0	s				
c	250	$°C.A^{-2}$				
ϑ_∞	22	°C				

Simulations

The control task that is taken as an example is to force the mass to track a sinusoidal trajectory with a period time of 20 s and an amplitude of 2 mm, during a total time of 40 s. The temperature rate is not included in the determination of the open loop input, i.e. it is based on quasi-static conditions:

$$u_{ol} = c^{-1}(\vartheta_d - \vartheta_\infty) \tag{3.10}$$

The simulation results are shown in Figure 3.9.

The mass of 1.63 kg is such that the wire consists entirely of martensite ($m = 1$) at room temperature; the strain equals 4.5% and ξ equals 2.5 (Figure 3.9c,e,f); The peak in the electric power during the first second (3.9d) is entirely due to the proportional action of the feedback controller. This causes the temperature of the wire to rise sharply (3.9b). As soon as ξ is zero, MA transformation starts, causing the wire to shrink. After 1 second the tracking error has vanished and the total power supplied to the wire corresponds to the calculated desired power. Meanwhile the martensite fraction decreases to 0.2 at $t = 10$ s (3.9e,f). At that moment the temperature must drop considerably, because then $\dot{m} = 0$ and $\dot{\xi} > 0$, i.e. the hysteresis loop has to be crossed. Because the necessary temperature fall cannot be accomplished, the wire elongates slower than it should (3.9a). The open loop input is based on steady state conditions, and does not predict such sharp drop. Between $t = 10$ s and $t = 13$ s ξ increases from zero to one, until at $t = 13$ s the opposite side of the hysteresis loop is reached (3.9c,f), and the realized trajectory catches up with the desired one (3.9a). The second cycle passes off in the same way.
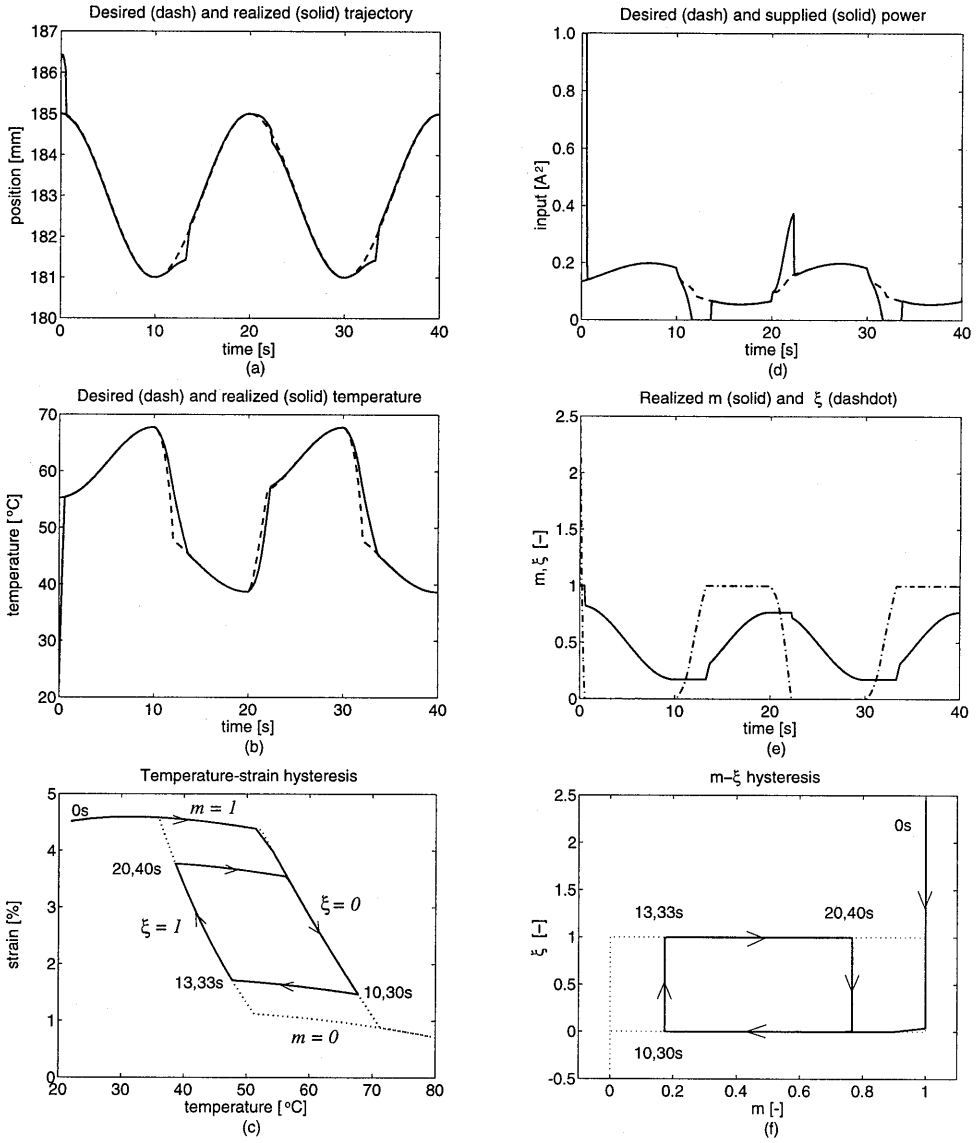
Figure 3.9: Simulation results for sinusoidal trajectory

Experiments

The proposed control method was also tested on the experimental system. The results of experiments with three different trajectories are presented, being a sawtooth, a sinusoid, and

a block wave, all with an amplitude of 1.5 mm. Period times of 5, 10 and 15 seconds were selected for each trajectory. Signals with a period time smaller than 5 seconds cannot be followed, because of the limited cooling rate of the wire. On the other hand, the performance of the controlled system did not benefit from the open loop control part for period times exceeding 15 seconds. The PI feedback controller alone is capable of tracking such slow movements.
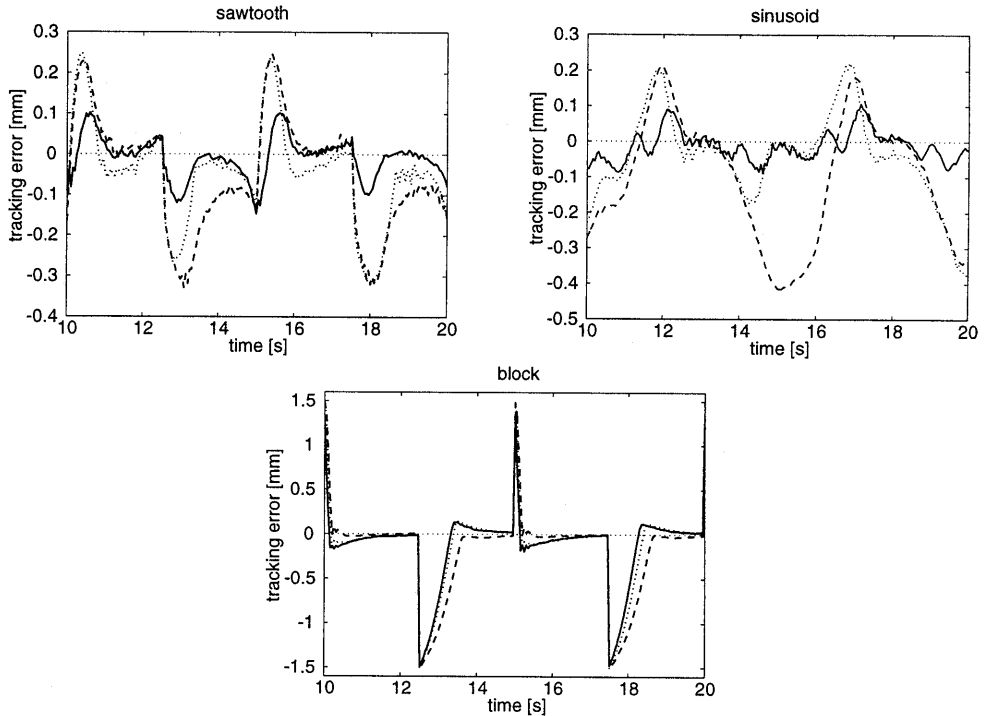
Figure 3.10: Tracking error for three different trajectories and three different controllers: only feedback (1, dashed), open loop without temperature rate (2, dotted), and full open loop with temperature rate (3, solid)

The performance of three controller settings was investigated. In all cases the PI feedback action was present, but the open loop component differed. The first controller consisted of the PI feedback part only. In the second case the open loop term was based on steady state conditions, i.e. the temperature rate was not used. The open loop component of the third controller was determined with Equation (3.5), where the temperature rate was included.

Some typical results are presented in Figure 3.10. The tracking error obtained with the three controller settings for trajectories with period time equal to 5 seconds is shown, during the third and fourth cycle. The results show that open loop control is an effective means to reduce the tracking error. However, if the desired temperature rate is not used to determine

the open loop part of the input (controller 2, dotted lines), a small improvement with respect to the controller with feedback only can be observed. The best results are obtained with the full open loop controller (3, solid lines). The peak values in the tracking error originated during hysteresis crossings are diminished considerably.

To compare the performance of the controllers, the Root Mean Square value of the tracking error during a number of cycles has been determined and is shown in Figure 3.11. These
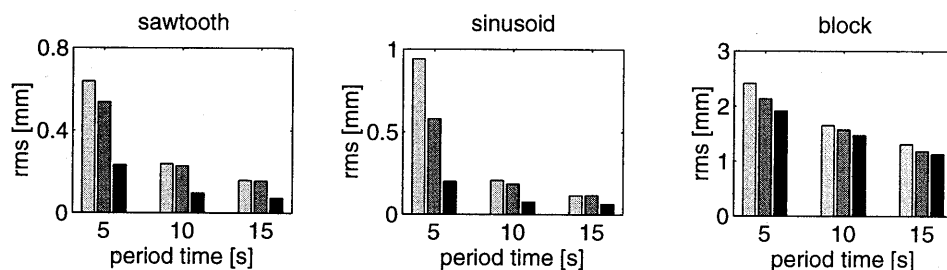
Figure 3.11: RMS value of tracking error obtained with: feedback only (1, left light coloured bars), open loop without temperature rate (2, middle medium coloured bars), and open loop with temperature rate (3, right dark coloured bars)

values show that the tracking error can be reduced by a factor 2 to 4 for the sawtooth and sinusoidal trajectories. The relatively small improvement for the block wave is not unexpected. The instantaneous changes in q_d yield a large tracking error and proportional feedback action, that exceeds the bounds of the electric power. Therefore an open loop term can hardly increase the reaction speed in this case.

3.3   Case 2: Bias spring SMA actuator

In this section the SMA actuator is combined with a helical spring. One end of the spring is attached to the SMA wire and the other to a frame. The experimental setup described in Section 3.2 was modified to investigate this so-called *bias spring* SMA actuator, see Figure 3.12. The spring stretches the SMA wire at room temperature, while heating the SMA wire results in shrinkage of the wire, and elongation of the spring. The spring is attached to the SMA wire by means of a Celeron block, which provides electrical insulation and withstands high temperatures (up to 120 °C). The displacement sensor is attached to the block by means of a counterbalanced traverse bar. To avoid rotational oscillations, a straight guide is installed. The fixation of the spring to the frame is adjustable, which allows changing of the pretension of the spring.
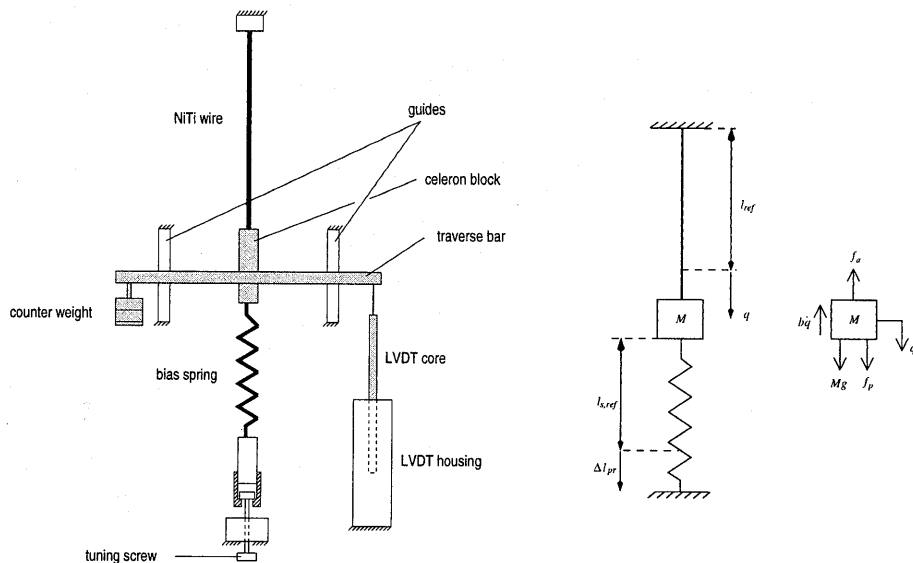
Figure 3.12: Experimental setup for bias spring SMA actuator and free body diagram

Spring design

The performance of the bias spring actuator strongly depends on the characteristics of the spring. A spring with high stiffness limits the stroke of the actuator, while a spring with low stiffness does not generate enough force to elongate the SMA wire at lower temperatures. The SMA constitutive model offers the opportunity to determine a suitable spring constant. At room temperature the spring must stretch the SMA wire to $m = 1$, and at 75°C the SMA wire must be completely austenitic ($m = 0$), despite the spring force. This way optimal use is made of the shape memory effect. Figure 3.13 shows the tensile curves of the SMA wire at 22°C and 75°C, as well as the elongation-force curve of the spring. Both the spring constant k_s and pretension length Δl_{pr} follow from the demand that the spring characteristic intersects the points $af\,(m = 0, \xi = 0)$ at 75°C and $mf\,(m = 1, \xi = 1)$ at 22 °C. The theoretical spring constant is 3800 N/m, and the pretension length is 9.6 mm. In practice the values are 3650 N/m, and 10.1 mm.

System equations

The equation of motion for this system reads (see Figure 3.12):

$$M\ddot{q} + b\dot{q} - Mg = f_p - f_a \tag{3.11}$$
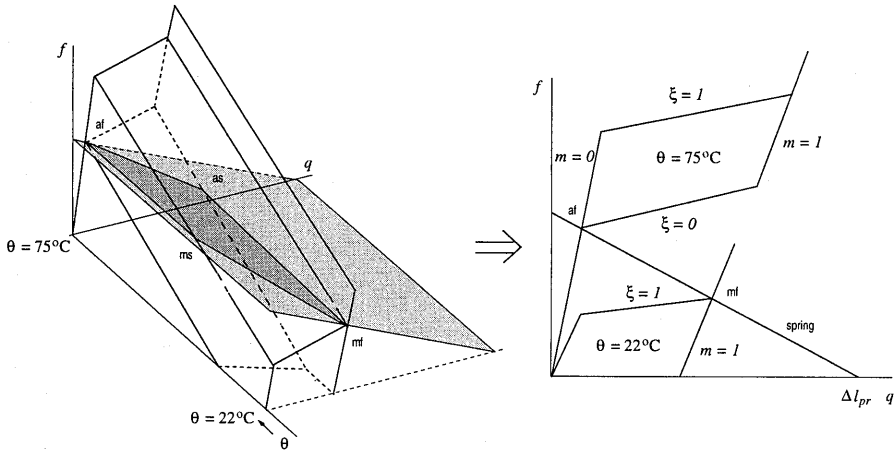
Figure 3.13: Design of the bias spring

where M is the mass of the celeron block, traverse bar, and LVDT core. The actuator dynamics are:

$$\tau\dot{\vartheta} + (\vartheta - \vartheta_\infty) = c\,u \tag{3.12}$$

$$\dot{f}_a = k_e\dot{q} + k_\vartheta\dot{\vartheta} \qquad\qquad f_p = k_s(\Delta l_{pr} - q) \tag{3.13}$$

The initial state is determined similarly to the mass-SMA system. The position $q_o = q(t = 0)$ determines the strain e_o and the spring force f_{po}. Then also the force f_{ao} and stress p_o are known. With temperature ϑ_o being equal to ϑ_∞ the entire initial state (m_o and ξ_o) can be determined.

3.3.1   Controller

Open loop

The inverse model of this system is:

System dynamics

$$f_d = -Mg \qquad ; \qquad \dot{f}_d = 0$$

Actuator dynamics

bias spring

$$f_{pd} = k_s(\Delta l_{pr} - q_d) \qquad ; \qquad \dot{f}_{pd} = -k_s \dot{q}_d$$

SMA wire

$$f_{ad} = f_{pd} - f_d \qquad ; \qquad \dot{f}_{ad} = \dot{f}_{pd}$$

$$\dot{\vartheta}_{ad} = \frac{1}{k_\vartheta} \dot{f}_{ad} - \frac{k_e}{k_\vartheta} \dot{q}_d$$

$$u_{ol} = c^{-1}(\tau \dot{\vartheta}_{ad} + \vartheta_{ad} - \vartheta_\infty)$$

Feedback

The transfer function of the linearized bias spring system is

$$G_s(s) = \frac{ck_\vartheta}{(\tau s + 1)(Ms^2 + bs + k_e + k_s)} \tag{3.14}$$

The difference with the transfer function of the mass SMA system in the previous section (Equation 3.7), is the extra stiffness introduced by the bias spring. The Bode plots of $G_{s,tr}(s)$ and $G_{s,el}(s)$ are shown in Figure 3.14. Because of the increased stiffness and the smaller mass, the transformation and elastic resonance frequencies are shifted to higher values (232 rad/s and 332 rad/s respectively) the damping coefficient is higher. Both effects are beneficial for the maximum control gain and attainable closed loop bandwidth. The control gain may be increased to 9400 A^2/m, yielding a bandwidth of 5.8 rad/s in the elastic regions, and 60.3 rad/s during transformation. This suggests an improved tracking capability compared to the mass system, as illustrated by Figure 3.15. The closed loop control gain and phase lag are close to unity and zero respectively at the maximum trajectory frequency of 1.2 rad/s.

3.3.2   Results

In Section 3.2 it was concluded that the addition of an open loop term is an effective means to reduce the tracking error. Besides, the desired temperature rate is an essential part of the open loop. To investigate whether or not these conclusions also hold for the bias spring actuator, similar experiments have been performed. Three different trajectory shapes have been supplied: a sawtooth, a sinusoid and a block wave. The performance of the same three
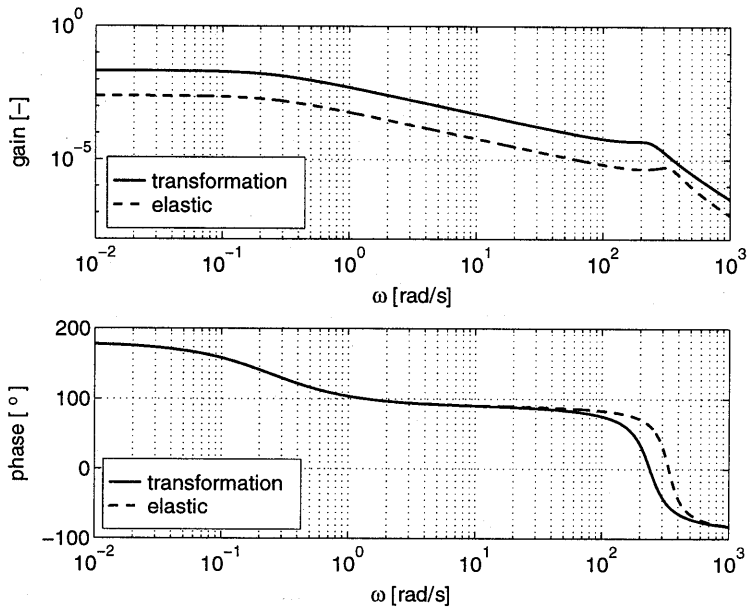
Figure 3.14: Bode plot of elastic and transformation transfer functions of bias spring system

controllers has been investigated: feedback alone (1), feedback with a steady state open loop part (2),

Table 3.4: System and control parameters

system			controller			
parameter	value	unit	parameter	value		unit
				calculated	used	
l_{ref}	209	mm	K_p	9400	2000	$A^2.m^{-1}$
M	0.080	kg	τ_i	4.0	1.0	$A^2.m^{-1}.s^{-1}$
b	10	$N.s.m^{-1}$				
k_s	3650	$N.m^{-1}$				

and feedback with complete open loop part (3). The experimental parameters are listed in Table 3.4.
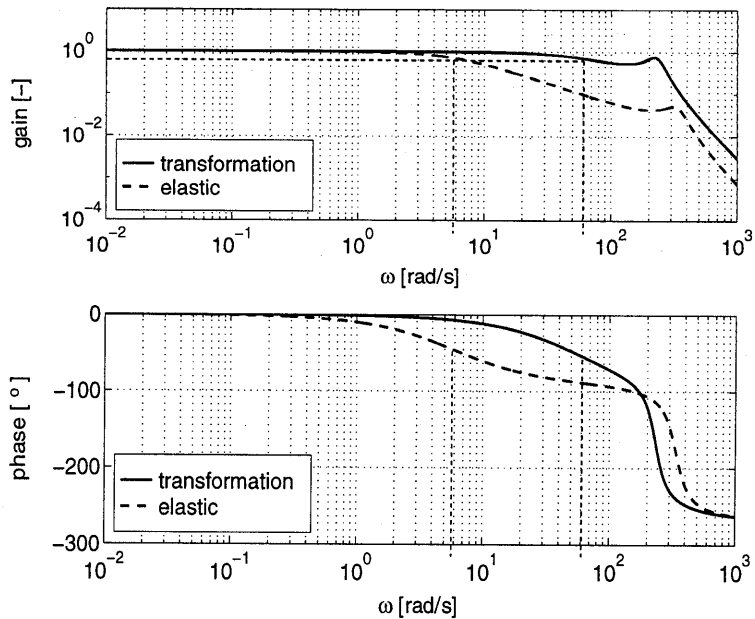
Figure 3.15: Bode plots of closed loop elastic and transformation transfer functions of bias spring system

Figure 3.16 summarizes the tracking results in terms of RMS values of the tracking error. In case of the sawtooth and the sinusoidal trajectory, the tracking error decreases if the open loop term is used. Again, heating dynamics are an essential part. However, the effect of the open loop is not as large as for the mass SMA system. This is due to the increased control gain of the feedback part. Similar to the mass SMA system, the open loop term has little effect for the block wave.

Figure 3.17 shows the tracking error for a block wave. The response time during heating (at $t = 10$ s) is considerably smaller than during cooling (at $t = 15$ s). Tracking is even worse during cooling than in case of the mass SMA system. This is due to the decreasing tensile spring force during cooling, yielding lower transformation temperatures. It takes more time to arrive at these lower temperatures.
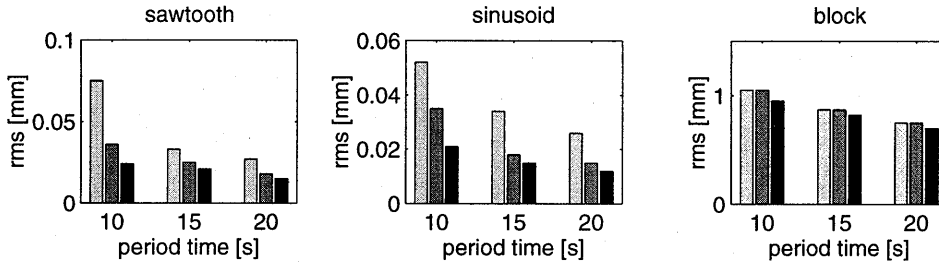
Figure 3.16: RMS value of tracking error obtained with: feedback only (1, left light coloured bars), open loop without temperature rate (2, middle medium coloured bars) and open loop with temperature rate (3, right dark coloured bars)
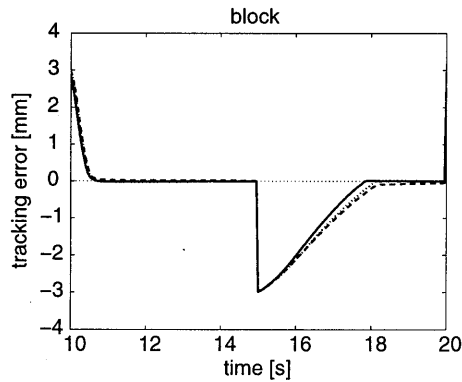
Figure 3.17: Tracking error for block wave: only feedback (1, dashed), open loop without temperature rate (2, dotted) and full open loop (3, solid)

3.4   Case 3: Differential SMA actuator

The third actuator setup investigated, is the *differential actuator*, where the passive spring is replaced by another SMA wire. Although both wires might be heated at the same time, always at least one wire is passive in this thesis and only one amplifier is used for the pair of SMA wires. Two diodes route the current to the appropriate SMA wire, see Figure 3.18. The sign of the total input u determines which wire is heated. The electric current is determined from u by

$$I = \text{sign}(u)\sqrt{|u|} \tag{3.15}$$

The current is automatically applied to the appropriate SMA wire. If the current is positive, wire 1 is heated, if it is negative, wire 2 is heated. Before installation, the wires are given a prestrain, such that they both have a martensite fraction of 0.5, so they both have maximum opportunity to shrink and elongate.
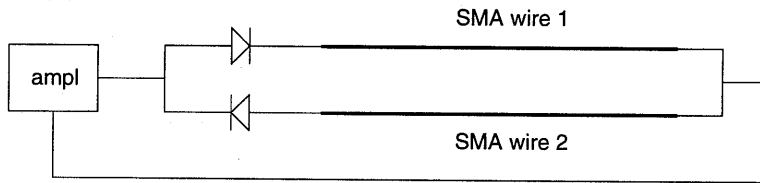
Figure 3.18: Electrical connection of differential actuator

3.4.1   System equations

The equation of motion is equal to Equation (3.11):

$$M\ddot{q} + b\dot{q} - Mg = f_p - f_a \tag{3.16}$$

However, the actuator dynamics have changed:

active SMA wire

$$\tau\dot{\vartheta}_a + (\vartheta_a - \hat{\vartheta}_\infty) = c\,u \tag{3.17}$$

$$\dot{f}_a = k_e\dot{q} + k_\vartheta\dot{\vartheta}_a \tag{3.18}$$

passive SMA wire

$$\tau\dot{\vartheta}_p + (\vartheta_p - \vartheta_\infty) = 0 \tag{3.19}$$

$$\dot{f}_p = k_e\dot{q} + k_\vartheta\dot{\vartheta} \tag{3.20}$$

The force in the passive wire does not only depend on the displacement, as is the case for the spring in the bias spring actuator, but also on its temperature and martensite fraction. The initial state is not uniquely defined for this system unless its history is known. This

is generally not the case. Therefore the initial state is estimated as follows. The position $q_o = q(t = 0)$ determines the initial strains e_{1o} and e_{2o}. The temperature of both wires is also known and equal to the ambient temperature. But contrary to the two systems in the previous sections the tensile forces are not known. It is assumed that the force in the lower wire is zero. The force and stress in the upper wire follows from Equation (3.16).

3.4.2 Controller

Open loop

The inverse model is:

System dynamics

$$f_d = -Mg \qquad ; \qquad \dot{f}_d = 0$$

Actuator dynamics

passive SMA wire

$$\tau \dot{\vartheta}_{pd} + (\vartheta_{pd} - \vartheta_\infty) = 0$$
$$\dot{f}_{pd} = k_e \dot{q}_d + k_\vartheta \dot{\vartheta}_{pd} \qquad\qquad\qquad (3.21)$$

active SMA wire

$$f_{ad} = f_{pd} - f_d \qquad ; \qquad \dot{f}_{ad} = \dot{f}_{pd}$$
$$\dot{\vartheta}_{ad} = \frac{1}{k_\vartheta} \dot{f}_{ad} - \frac{k_e}{k_\vartheta} \dot{q}_d$$
$$u_{ol} = c^{-1}(\tau \dot{\vartheta}_{ad} + \vartheta_{ad} - \vartheta_\infty)$$

It is generally not possible to determine directly from $q_d(t)$ and $\dot{q}_d$ which wire, according to the model, will be active and passive respectively. Therefore in the calculation of u_{ol}, as a first attempt, wire 1 is always assumed to be the active wire. The open loop input is then computed following the relations shown above. If the computed open loop input is negative, obviously the wrong wire was selected (since this is physically impossible), and wire 2 is assumed to be active. Ideally the calculated open loop input should be positive the second time. However, it may happen that even then a negative input is computed. This is entirely due to the fact that the temperature rate in the last of the above equations is calculated according to the interpolation in Equation (2.65), yielding a value (during elastic crossing of the hysteresis loop) that is somewhat different from the exact value. In these cases the open loop input is set to zero. This does not mean that the total input u is zero, because a feedback part is present as well. The feedback part of the input u_{fb} may be larger then and of opposite sign with respect to u_{ol}. Then the actually heated wire is not the one that was predicted by the model.

Feedback

The transfer function of the linearized differential system is

$$G_s(s) = \frac{ck_{\vartheta,a}}{(\tau s + 1)(Ms^2 + bs + k_{e,a} + k_{e,p})} \qquad (3.22)$$

It looks very similar to the bias spring transfer function. The spring constant has been replaced by the stiffness of the passive SMA wire. The Bode plots of $G_{s,tr}(s)$ and $G_{s,el}(s)$ are shown in Figure 3.19. They represent the linearized behaviour of the actuator, when *both* wires are in a transformation region, and in an elastic region respectively. The transfer function corresponding to one wire being elastic, while the other is transforming, is in between $G_{s,tr}(s)$ and $G_{s,el}(s)$ and is not considered. Because of the lower stiffness of an SMA wire
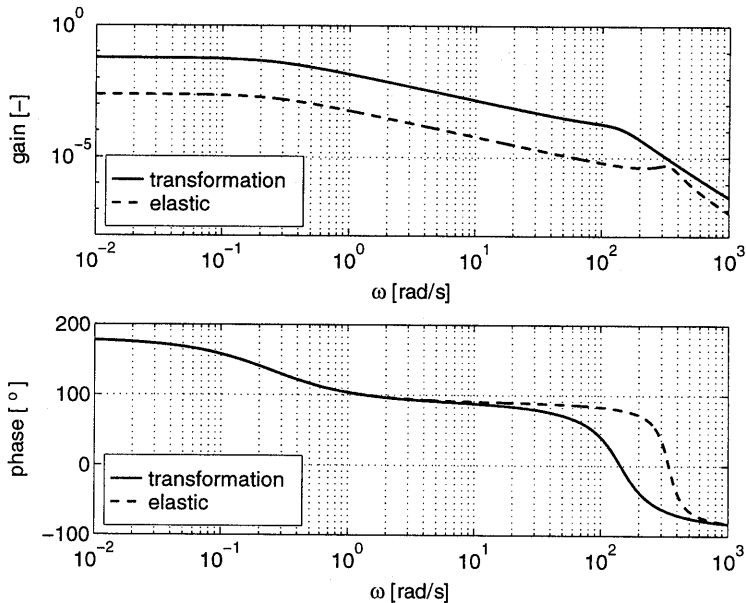
Figure 3.19: Bode plot of elastic and transformation transfer functions of differential system

compared with the spring, the control gain can only be increased to 3400 A²/m, yielding a bandwidth of 2.0 rad/s in the elastic regions, and 140 rad/s during transformation. Figure 3.20 shows the closed loop control gain and phase.

Table 3.5 lists the calculated and used values of the control parameters.

3.4.3 Results

The tracking performance was investigated for the same trajectories and controllers as the bias spring actuator. In Figure 3.21 the RMS value of the tracking error for different frequencies
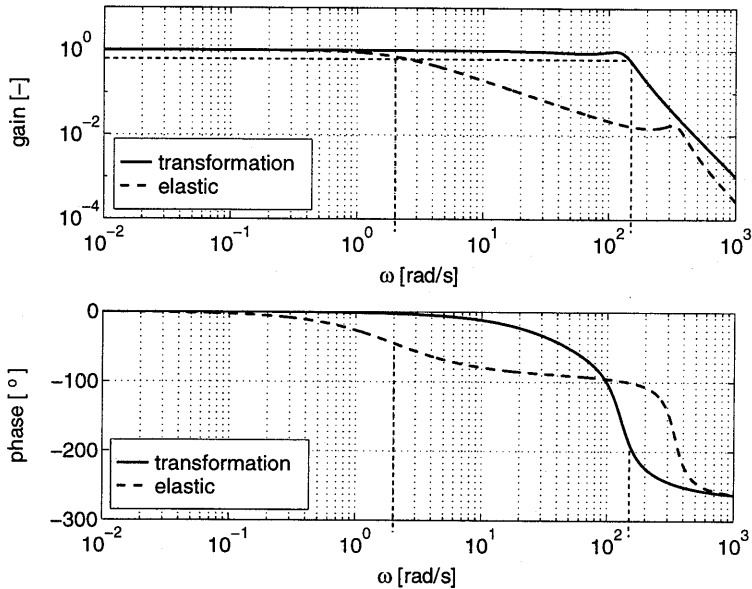
Figure 3.20: Bode plot of closed loop elastic and transformation transfer functions of differential system

is shown. The results show the same trend as Figure 3.16.

Figure 3.22, showing the tracking error for a block wave trajectory, is illustrative for the difference between a bias spring actuator and a differential actuator. The slow response during cooling with the bias spring actuator, see Figure 3.17, has improved considerably (see tracking result at $t = 15$ s). On the other hand, the response speed has deteriorated during movement in the opposite direction (at $t = 10$ s): the previously active, heated wire must cool down first, before it can elongate without a huge force increase.

Table 3.5: Control parameters

parameter	value		unit
	calculated	used	
K_p	3400	3000	$A^2.m^{-1}$
τ_i	4.0	3.8	$A^2.m^{-1}.s^{-1}$
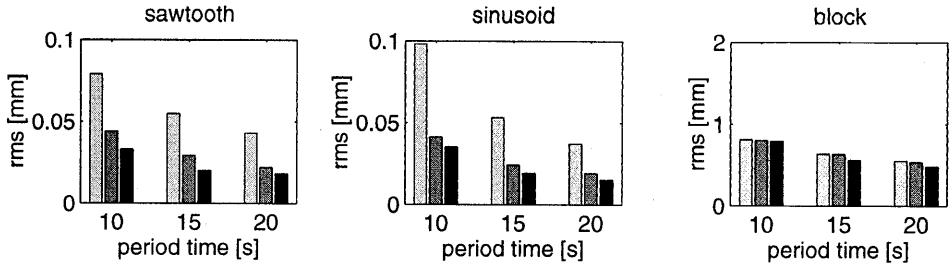
Figure 3.21: RMS value of tracking error obtained with: feedback only (1, left light coloured bars), open loop without temperature rate (2, middle medium coloured bars) and open loop with temperature rate (3, right dark coloured bars)
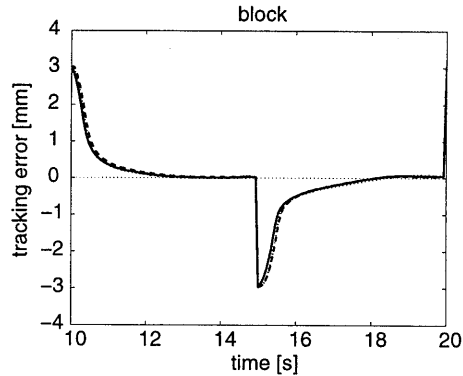
Figure 3.22: Tracking error for block trajectory: only feedback (1, dotted), open loop without temperature rate (2, dashed) and full open loop (3, solid)

3.5   Evaluation of bias spring actuator and differential actuator

In this section several properties of the bias spring actuator and the differential actuator are compared. The single wire actuator used in the mass SMA system is difficult to apply in practical applications, and is not evaluated here. The actuators are compared on tracking performance, closed loop bandwidth and attainable stroke. The tracking performance of each actuator has already been presented in the previous sections, and is compared in Table 3.6.

Closed loop bandwidth

In Sections 3.3.1 and 3.4.2, theoretical values for the closed loop bandwidth were derived based on linearized models, and theoretically obtained control parameters. During experiments lower values for the control parameters were used. The theoretical closed loop band-

width corresponding to these parameter values is 2.1 rad/s for the bias spring actuator, and 1.8 rad/s for the differential actuator. The bandwidth obtained during experiments depends on the amplitude and displacement range of the desired trajectory, due to the nonlinear SMA behaviour. It is therefore impossible to specify the actuator bandwidth with a single value. However, applying the same trajectory to different actuators gives (qualitative) comparable information. The reference trajectory applied was a sinusoid with an amplitude of 1.5 mm and an average of 5.4 mm. The RMS value of the tracking error was determined for increasing trajectory frequency, and is plotted for both actuators in Figure 3.23.
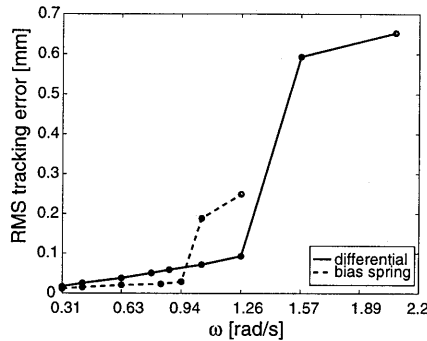
Figure 3.23: RMS error vs. frequency for sinusoid with amplitude of 1.5 mm

The tracking error obtained with the bias spring actuator increases sharply at frequencies exceeding 0.9 rad/s. The experimental bandwidth of the differential actuator is higher. It is capable to track trajectories up to 1.3 rad/s.

Actuator stroke

The stroke of an SMA actuator depends on the maximum recoverable transformation strain in the active SMA wire, and on the characteristics of the passive element. The stroke Δq_{max} is defined here as the difference between the displacement when the wire is in the martensitic state ($m = 1, \xi = 1, \vartheta = 22°C$), and when the wire is in the austenitic state ($m = 0, \xi = 0, \vartheta = 75°C$). The required SMA wire length can be calculated, when the desired maximum displacement range Δq_{max} is specified. The bias spring actuator stroke according to the model $\Delta q_{max,th}$ is $q(75°C) - q(22°C) = 6.3$ mm. The experimentally determined $\Delta q_{max,exp}$ is smaller: 5.3 mm. The values for the differential actuator are $\Delta q_{max,th} = 6.2$ mm and $\Delta q_{max,exp} = 7.4$ mm respectively. The difference between theory and experiment is probably caused by a discrepancy between the SMA model and the real behaviour. Accumulated plastic deformation, resulting in a smaller recoverable transformation strain may also be a cause.

Table 3.6 summarizes the actuator characteristics for the bias spring and differential actuator. The quantities $\overline{RMS}$ are the RMS values of the tracking error obtained for the three trajectory shapes, with the full open loop controller (3), averaged over the trajectory period

Table **3.6:** Comparison of bias spring and differential actuator

	bias spring	differential	unit
$\overline{RMS}_{saw}$	0.060	0.072	mm
$\overline{RMS}_{sin}$	0.049	0.058	mm
$\overline{RMS}_{block}$	0.81	0.58	mm
$\omega_{b,th}$	2.1	1.8	rad/s
$\omega_{b,exp}$	0.9	1.3	rad/s
$\Delta q_{max,th}$	6.3	7.4	mm
$\Delta q_{max,exp}$	5.3	6.2	mm

times. Both actuators are quite comparable. Smooth trajectories that do not require an extreme control input (sawtooth, sinusoid) are tracked slightly better by the bias spring actuator. However, the differential actuator performs better when extreme inputs are required (block wave), especially at the moments where the bias spring actuator is limited by the cooling rate. The differential actuator has a higher bandwidth and stroke, although the differences are small.

An aspect that has not been discussed yet, is the tensile force in the SMA wires. Because of the low stiffness of a (passive) SMA wire in the transformation regions, the tensile force experienced by the active SMA wire of a differential actuator is much lower than in case of a bias spring actuator. Especially at higher temperatures this difference is evident.

3.6   Conclusions

In this chapter three different actuator setups have been investigated. The control method proposed in Chapter 2 has been tested both numerically and experimentally. With respect to the feedback part of the control law, it was shown that a derivative action does not increase the attainable bandwidth. Theoretical values for the proportional and integral control parameters were derived based on linearized models in the elastic and transformation region. The applicability of the theoretical values in practice was limited.

With respect to the open loop part, experiments with a number of test trajectories point out that adding an open loop term diminishes the tracking error in all cases. For the mass SMA system, a decrease of the tracking error by a factor 4 in comparison with feedback control only could be obtained. The effect was not that large for the bias spring and the differential actuator, because of the increased control gain that could be applied. The first order dynamics of the heating and cooling process form an indispensable part of the open loop part. An open loop part based on steady state conditions has little effect. The overall performance of the bias spring actuator and the differential actuator is comparable.

4   An SMA actuated robotic finger

4.1 Introduction

In many automated industrial processes, robotic systems driven by electric, pneumatic or hydraulic actuators are used. However, actuation of small robotic structures, such as the fingers of an artificial robotic hand, requires small, light-weight actuators. Until now, most robotic hands and fingers are actuated by a combination of relatively large actuators, positioned at a distance from the fingers, and tendons for power transmission to the fingers (Reynaerts, 1995). Shape memory alloys are an interesting alternative for actuation of robotic fingers, because miniaturization can be carried out to a high level. Besides, there is no need for tendons, since the SMA's can be applied as active tendons themselves.

To investigate the applicability of SMA's as actuators in a robotic finger, a threelink robotic finger with two rotational joints has been developed. Each rotary joint is actuated by a pair of SMA wires acting in an antagonistic manner. This principle is the rotational variant of the differential translational actuator described in the previous chapter.

4.1.1 The role of shape memory alloys in robotics

Practical applications of SMA actuators in robotics are not widespread. Most examples reported in literature are for demonstration purposes. Furuya and Shimada (1991) used SMA wires and a bias spring to actuate the legs of a submarine, crab-resembling robot. Jost et al. (1992) proposed to exploit the two way memory effect in a robot, including a gripper mechanism. No experimental results were reported. Kuribayashi (1989b) developed a rotational servo motor.

Several authors focused attention on a single actuator, that can be incorporated in a robotic device. The actuators are either translational or rotational. All translational actuators are of the bias spring type. Rotary actuators are either of the bias spring or the differential type.

One of the first translational actuators reported was developed by Honma et al. (1984). They used an SMA spring not only as actuator, but also as a (position) sensor, by measuring the electric resistance. The resistance varies with the length of the SMA spring. However, it also depends in a complex way on the crystal structure and temperature (see e.g. Harrison, 1989). It is very difficult, if not impossible to find a one-to-one relationship between

resistance and position in different loading and thermal conditions. A translational actuator consisting of 24 parallel SMA wires and a bias spring was developed by Maclean et al. (1991b). They used a proportional feedback control. Both position and force control experiments were performed. The authors recognize the large difference in performance between cooling and heating stages of the SMA elements. This is a consequence of using a bias spring type actuator at lower temperatures. Reynaerts (1995) solved this problem by oil cooling. The actuator consists of a set of parallel SMA wires in an oil filled housing. Grant and Hayward (1995) developed a translational actuator that combines the advantages of helical springs (large stroke), and of wires (efficient use of the material). The stress in SMA helical springs is not uniform; therefore not all material contributes equally to the shape memory effect.

Reynaerts and Van Brussel (1991a, 1991b) developed a bias spring type rotary robotic actuator, that can be integrated in a robotic finger. As with the translational actuator, the wires are oil cooled to increase the bandwidth. A differential actuator was developed by Kuribayashi (1991). He applied a proportional control law and a Pulse Width Modulation amplifier. To be able to increase the amplitude of the current pulses and obtain a faster response, while avoiding excessive heating of the SMA wires, a temperature sensor serving as a safety device, was attached to the wires. Gorbet and Russell (1995a) increased the bandwidth of a rotary differential actuator from 0.08 Hz to 0.3 Hz by applying a mobile heat sink, however at the expense of compactness and weight.

4.1.2   Control methods

The majority of the actuators is controlled by classical P, PI, PD or PID feedback. A few alternative control strategies have been reported. Grant and Hayward (1995) applied *variable structure control*. In that case the control input can have a limited number of discrete values. Switching between the values depends on the tracking error. Nakazato et al. (1993a, 1993b) investigated the feasibility of *fuzzy control* for position control of a differential SMA actuator.

Very few attempts have been reported to use a model of the entire system to derive optimal robust controller settings for a feedback control law or to apply model-based control concepts. Tuning of the feedback control parameters is almost exclusively done on a trial-and-error basis. A few authors used a model to derive feedback controller settings. Madill and Wang (1994) derived a stability criterium for proportional SMA feedback controllers, based on a thermomechanical model of an SMA wire, including heating dynamics and hysteresis behaviour. However, inertia effects were not taken into account. Their conclusion that any proportional feedback controller with finite gain yields a stable system must therefore be considered with care: for all actuators described in this thesis, the control gain is limited. Gorbet and Wang (1995b) considered stability criteria for a large class of feedback controllers. Experiments with a theoretically stable PI controller, and a trial-and-error (theoretically unstable) PI controller, revealed that the theoretical upper bound for the control gain was too conservative. Lashlee et al. (1993, 1994), Rhee (1992), and Rhee and Koval (1993) used the *LQG/LTR method* to design a feedback controller for vibration control of flexible systems. The design of the controller was based on a linear model of the SMA actuators and the flexible system.

Model-based concepts are still very rarely used to control SMA actuators. Arai et al. (1994) modeled the SMA behaviour by a nonlinear relation between strain, stress and temperature. Hysteresis effects were accounted for by addition of a strain rate term. Arai et al. (1995) used this model to construct a *computed torque* control law (see e.g. Slotine and Li, 1991). The results obtained with this control law were comparable to results obtained with a PID controller. It should be emphasized that strains remained within a few tenths of percents, and no load was applied. Model uncertainties are therefore expected to be quite small. It is not clear if the two control methods are competitive in different (e.g. loading) situations. Choi and Cheong (1996) made this kind of control law more robust by adding a *sliding mode* term to the computed torque input, for vibration control of a cantilever beam. Modelling errors, introduced e.g. by using a linearized model of the SMA behaviour to compute the computed torque input, were successfully handled by the sliding mode term. Reynaerts and Van Brussel (1991a, 1991b, 1995) proposed a combination of PID feedback control with a model-based open loop term. The open loop term was based on a measured strain vs. electric power curve, in quasi-stationary conditions. This curve was stored as a table. The electric power necessary to obtain a prescribed strain could then be read from the table. The main limitations of this approach are the inability to predict the electric power during crossing of the hysteresis loop, or in different conditions (e.g. loading, surrounding temperature, convective conditions), and to take into account the first order heating dynamics of an SMA wire. Therefore the authors proposed to use a mathematical model instead of a measured curve. This strategy is a main issue in this thesis.

4.2   Design of a robotic finger

To investigate the possibilities and problems associated with the application of shape memory alloy wires as actuator in a robotic structure, a robotic finger with two identical links has been developed. Usually a robot consists of several links, connected to one another by rotary joints. Large links are driven by actuators in the joints, while small links (fingers) are usually actuated with tendons.

The robotic finger developed for this research consists of three links and two joints, see Figure 4.1. The two joints allow motions in the vertical plane. Each joint is actuated by a differential SMA actuator. The joint angles between successive links, φ_1 and φ_2, are used as degrees of freedom. The finger tip is called end-effector, and its position is characterized by $\underline{r} = [r_x \quad r_y]^T$. Figure 4.2 shows two views of a link. Instead of connecting two separate wires, one wire is divided into two parts. Both ends are attached to the link. A total of nine pulleys guides the wire. All pulleys can rotate freely, except for one, which is fixed to the joint shaft. The wire is attached at one spot to this pulley, such that both wire parts have the same initial length l_m. If one half of the wire contracts (for example due to heating), the joint shaft is rotated, and also the next link, that is rigidly connected to this shaft. At the same time, the other half of the wire is elongated. Despite the fact that we are dealing with one wire divided in two parts, the two halves will be treated as separate wires from now on. Ball bearings have been applied for all rotating parts to diminish friction as much as possible. A simple experiment was performed to investigate the amount of damping. The transient
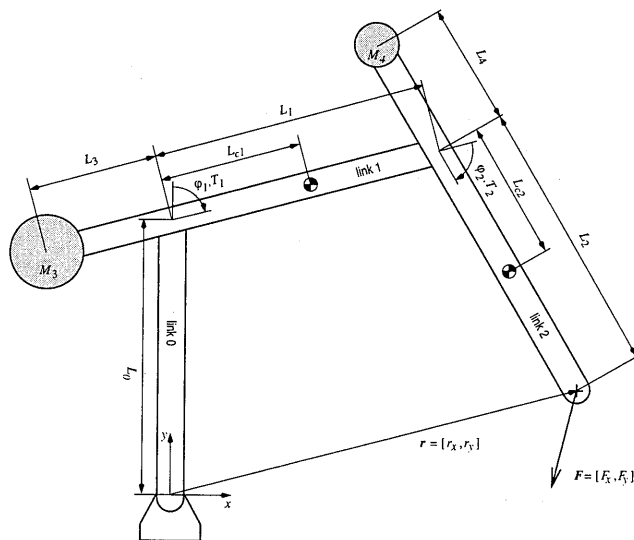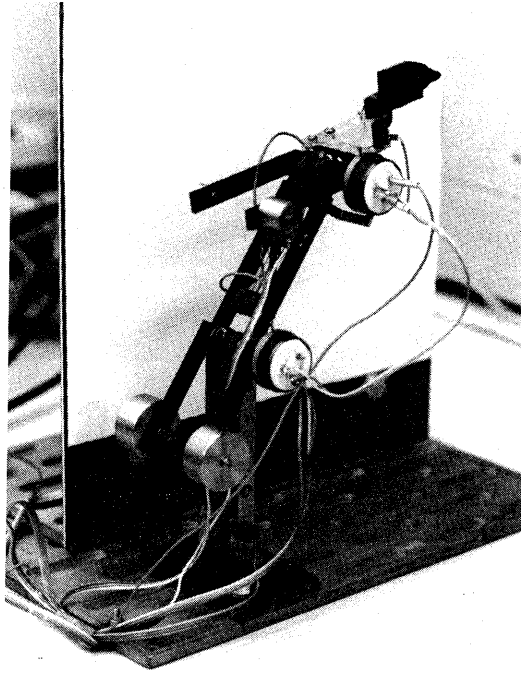
Figure 4.1: The SMA driven robotic finger

response to an impulse of both joints was recorded. The responses were smooth and showed
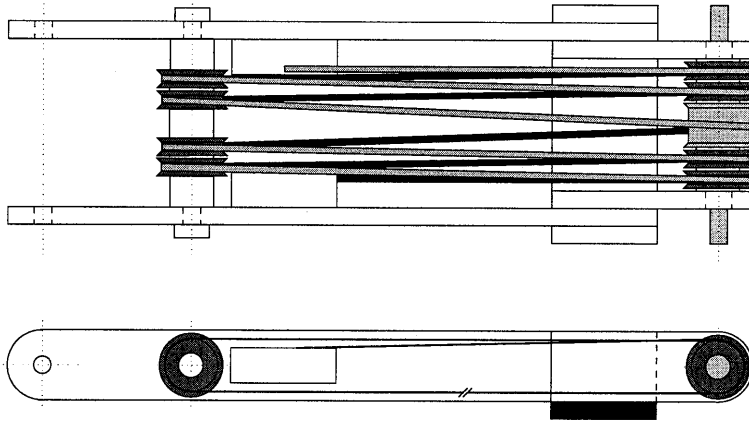
Figure 4.2: One link of the robotic finger

damping factors of 0.08 and 0.09 respectively. The damping is assumed to be caused mainly by material damping and is modeled as viscous friction.

4.2.1   Kinematics

Considering joint i ($i = 1, 2$), the wire causing a positive rotation when contracting is called wire 1, the other one is called wire 2. The lengths of the two wires l_{1i} and l_{2i} are related to the joint angle φ_i by:

$$l_{1i} = l_m - R(\varphi_i - \varphi_{mi}) \qquad ; \quad l_{2i} = l_m + R(\varphi_i - \varphi_{mi}) \qquad i = 1, 2 \qquad (4.1)$$

where R is the pulley radius, and φ_{mi} is the joint angle when both wires have length l_m. The angle φ_{mi} can be chosen arbitrarily for each joint and determines the workspace of the end-effector. The position of the end-effector is related to the joint angles by

$$\begin{bmatrix} r_x \\ r_y \end{bmatrix} = \begin{bmatrix} L_1 s_1 + L_2 s_{12} \\ L_0 + L_1 c_1 + L_2 c_{12} \end{bmatrix} \qquad (4.2)$$

where $s_1 = \sin(\varphi_1)$, $s_{12} = \sin(\varphi_1 + \varphi_2)$, $c_1 = \cos(\varphi_1)$ and $c_{12} = \cos(\varphi_1 + \varphi_2)$. See Figure 4.1 for the definition of link lengths L_0, L_1 and L_2. The end-effector velocity reads

$$\begin{bmatrix} \dot{r}_x \\ \dot{r}_y \end{bmatrix} = \begin{bmatrix} L_1 c_1 + L_2 c_{12} & L_2 c_{12} \\ -L_1 s_1 - L_2 s_{12} & -L_2 s_{12} \end{bmatrix} \begin{bmatrix} \dot{\varphi}_1 \\ \dot{\varphi}_2 \end{bmatrix} \qquad \text{or} \qquad \underline{\dot{r}} = \underline{J}(\varphi)\underline{\dot{\varphi}} \qquad (4.3)$$

$\underline{J}(\underline{\varphi})$ is called the Jacobian matrix (Asada and Slotine, 1986) of the robot.

4.2.2   Dynamics

The dynamics of the robot relating all forces and torques acting on the robot can be derived using Lagrange's method (Asada and Slotine, 1986). They can be put in the general form

$$\underline{M}\ddot{\underline{q}} + \underline{B}(\dot{\underline{q}}) + \underline{g}(\underline{q}) = \underline{f} + \underline{w} \tag{4.4}$$

with

$$\underline{M} = \begin{bmatrix} M_{11} & M_{12} \\ M_{12} & M_{22} \end{bmatrix} \quad ; \quad \underline{B} = \begin{bmatrix} b_1\dot{q}_1 - 2h\dot{q}_1\dot{q}_2 - h\dot{q}_2^2 \\ h\dot{q}_1^2 + b_2\dot{q}_2 \end{bmatrix} \tag{4.5}$$

$$\underline{g} = \begin{bmatrix} g_1 \\ g_2 \end{bmatrix} \quad ; \quad \underline{f} = \begin{bmatrix} T_1 \\ T_2 \end{bmatrix} \quad ; \quad \underline{w} = \underline{J}^T \begin{bmatrix} F_x \\ F_y \end{bmatrix} \tag{4.6}$$

where M_{ij} represents inertia terms, b_i viscous friction coefficients, h centrifugal and Coriolis coefficients, g_i torques due to gravity, and w disturbance torques due to a tip force $F = [F_x \quad F_y]^T$. Expressions for these parameters are given in Appendix A. The joint torques T_1
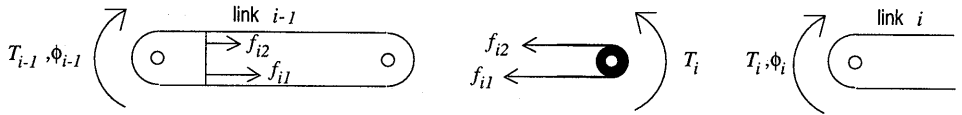
Figure 4.3: Free body diagrams of a joint and the two corresponding links

and T_2 result from the tensile forces exerted by the SMA wires, see Figure 4.3:

$$T_i = R(f_{i1} - f_{i2}), \qquad i = 1, 2 \tag{4.7}$$

The nonlinear velocity terms as well as the gravity torques can be eliminated by appropriate counterbalance masses (Ropponen, 1993). The terms h and g_2 vanish when L_{c2} equals zero, which can be achieved by mounting a counterbalance mass on link 2, such that the centre of gravity corresponds with joint 2. The gravity torque g_1 disappears when the centre of gravity of the combination of links 1 and 2 coincides with joint 1. Without counterbalance masses the gravity torque g_1 may become quite large. If the centres of gravity of the links are assumed to coincide with the geometrical centres, i.e. $L_{ci} = L_i/2$, the maximum value of g_1 equals 0.08 Nm ($R = 3$ mm). The force in the loaded wire is then 27 N; the stress equals 450 MPa. Since the force of the opposing wire may reach 10 N, it is obvious that the wires are loaded unnecessarily severely without counterbalance masses. Therefore the robot links have been counterbalanced. Table 4.7 contains the values of all relevant kinematic and dynamic parameters of the robotic finger.

4.3   Experimental setup

The experimental setup is similar to the setup described in the previous chapter. Differences are the number of input and output channels (2x2), and position sensors. Low friction servo

Table **4.7**: Kinematic and dynamic parameters of the robotic finger

link 0		link 1		link 2		
parameter	value	parameter	value	parameter	value	unit
L_0	80.0	L_1	77.0	L_2	85.0	mm
		L_{c1}	46.1	L_{c2}	31.5	mm
		M_1	31.5	M_2	20.7	g
		J_1	1.556	J_2	1.246	$\times 10^{-5}$ kg.m^2
		R	3.0	R	3.0	mm
		φ_{m1}	45	φ_{m2}	45	°
		L_3	44.0	L_4	44.0	mm
		M_3	95.2	M_4	14.8	g
		J_3	0.685	J_4	0.0185	$\times 10^{-5}$ kg.m^2

potentiometers (R.S. Components Ltd. 173-580) are mounted on the joint shafts to measure the joint angles. After AD conversion the resolution of both sensors is 7.6×10^{-4} and 7.2×10^{-4} rad respectively.

4.4   Response to prescribed input

Before any control experiments were performed, the response of the two joints to a prescribed current was investigated. If the wires of joint 1 were activated, then the wires of joint 2 were not, and vice versa. A sinusoidal current with a period time of 10 seconds and amplitudes of 0.25, 0.35 and 0.50 A respectively was supplied to the SMA wires. Figure 4.4 shows the joint angles during 40 seconds. Friction effects are not noticeable: the joints move quite smoothly. The hysteresis behaviour of the SMA wires results in a nonlinear response. For small current amplitudes (0.25 A and 0.35 A), the resulting temperature range is too narrow to reach either side of the hysteresis, i.e. always $0 < \xi < 1$, therefore restricting strains and joint angles to small variations. For larger current amplitudes (0.50 A), the transformation regions of the wires are reached ($\xi = 0$ or $\xi = 1$), yielding large strains and joint angles This explains why the joint angle amplitudes do not increase proportionally with applied electric power. Crossing of the hysteresis can also be observed in the response to a current of 0.50 A. After each extremum the joint angles change very little, until at a certain point the other side of the hysteresis is encountered, resulting in a steep curve.

The difference in amplitude between φ_1 and φ_2 may have several causes. Different amounts of unrecoverable (plastic) strain may have accumulated in the SMA wires in the past, limiting the amount of recoverable strain. As explained before, strain is very suscepti-
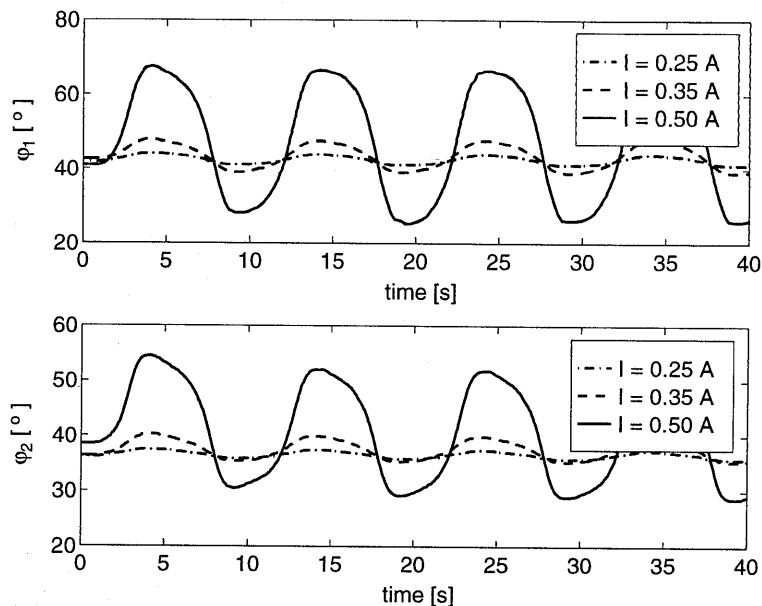
Figure 4.4: Response of both joints to a sinusoidal electric current

ble to temperature variations at the transformation regions. A small difference in temperature (because of differences in convective and conductive heat loss) has therefore a big effect on the strain and joint angle attained.

4.5   Controller

It is assumed that, despite the fact that the equations of motion are coupled, the joints of the robotic finger can be controlled independently, so the input for each actuator only depends on the desired and measured trajectory of the associated joint angle. Similar to the actuators analysed in the previous chapter, two control approaches were applied. First, individual (local) PI feedback control laws were used for trajectory tracking. To improve the performance, an open loop control term was added.

4.5.1   Open loop

The open loop input for each joint is determined analogously to the differential actuator analysed in the previous chapter. The inertia torques $\underline{M}\ddot{q}$ and velocity terms $\underline{B}(\dot{q})$ are very small compared to the static forces in the SMA wires, and are therefore neglected in the derivation of the open loop inputs. The relations between the joint angles and the desired

lengths of the opposing wires, as well as their rates are:

$$
\begin{aligned}
l_{1i} &= l_m - R(\varphi_i - \varphi_{mi}) \quad ; \quad \dot{l}_{d1i} = -R\dot{\varphi}_{di} \\
l_{2i} &= l_m + R(\varphi_i - \varphi_{mi}) \quad ; \quad \dot{l}_{d2i} = R\dot{\varphi}_{di}
\end{aligned}
\qquad i = 1,2
\tag{4.8}
$$

The inverse model of the robotic finger is:

System dynamics

$$
\underset{\sim}{f}_d = \underset{\sim}{0} \qquad\qquad ; \qquad\qquad \dot{\underset{\sim}{f}}_d = 0 \tag{4.9}
$$

Actuator dynamics

    for $i = 1,2$

        passive SMA wire

$$
\tau\dot{\vartheta}_{pd,i} + (\vartheta_{pd,i} - \vartheta_\infty) = 0
$$

$$
\dot{f}_{pd,i} = k_e\dot{\varphi}_{d,i} + k_\vartheta\dot{\vartheta}_{pd,i} \tag{4.10}
$$

        active SMA wire

$$
f_{ad,i} = f_{pd,i} \qquad ; \qquad \dot{f}_{ad,i} = \dot{f}_{pd,i}
$$

$$
\dot{\vartheta}_{ad,i} = \frac{1}{k_\vartheta}\dot{f}_{ad,i} - \frac{k_e}{k_\vartheta}\dot{\varphi}_{d,i}
$$

$$
u_{ol,i} = c^{-1}(\tau\dot{\vartheta}_{ad,i} + \vartheta_{ad,i} - \vartheta_\infty)
$$

    end

4.5.2   Feedback

The transfer function of joint i relating $\Phi_i(s) = \mathcal{L}(\varphi_i)$ to $U_i(s) = \mathcal{L}(u_i)$ is

$$
G_{s,i}(s) = \frac{ck_{\vartheta i}R}{(\tau s + 1)(M_{ii}\tau s^2 + b_i s + (k_{e1,i} + k_{e2,i})R^2)} \tag{4.11}
$$

The main difference between the two joints is the inertia term M_{ii}. Because of the larger inertia of joint 1, the resonance frequency of joint 1 in the transformation region is at 3.9 rad/s, while for joint 2 it is at 13.5 rad/s, see Figure 4.5, where the Bode plots of $G_{s,tr}(s)$ and $G_{s,el}(s)$ of both joints are shown. The controller parameters were determined similar to the procedure followed in the previous chapter. The higher resonance frequency for joint 2 results in a higher control gain: $K_{p1} = 0.14$ against $K_{p2} = 0.5$. The closed loop bandwidth is consequently lower for joint 1. The bandwidth during transformation is 0.76 rad/s, and 0.028 rad/s in the elastic regions for joint 1. The values for joint 2 are 2.76 rad/s and 0.1 rad/s, see Figure 4.6. It is therefore expected that joint 2 has better tracking capabilities.

During the experiments higher values for K_p could be applied, see Table 4.8. The calculated and applied values are of the same order of magnitude, but still differ considerably. The linearized models used to derive the controller parameters do not describe the real behaviour well enough to achieve good tuning of the controller parameters. However, they are able to give an indication of the order of magnitude.
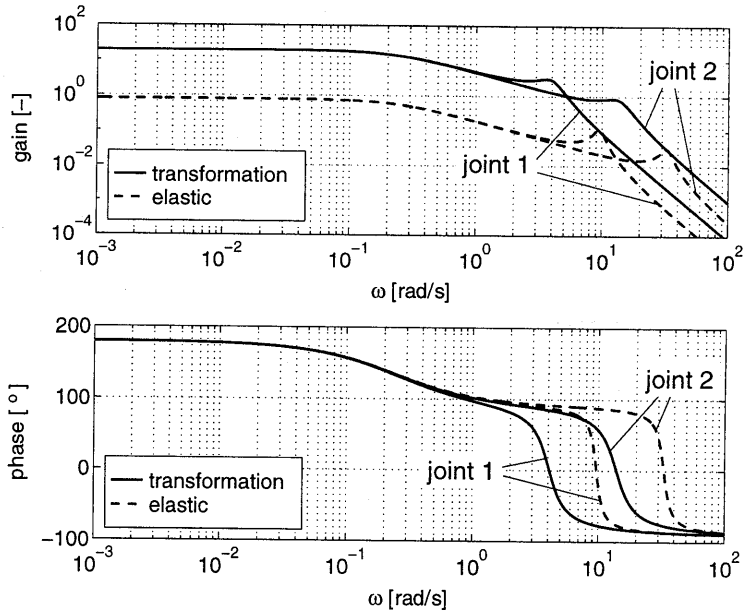
Figure 4.5: Bode plot of elastic and transformation transfer functions of joint 1 and 2

Table 4.8: Control parameters

parameter	value				unit
	joint 1		joint 2		
	calculated	used	calculated	used	
K_p	0.14	1.0	0.5	2.0	$A^2.m^{-1}$
τ_i	4.0	1.0	4.0	1.0	$A^2.m^{-1}.s^{-1}$
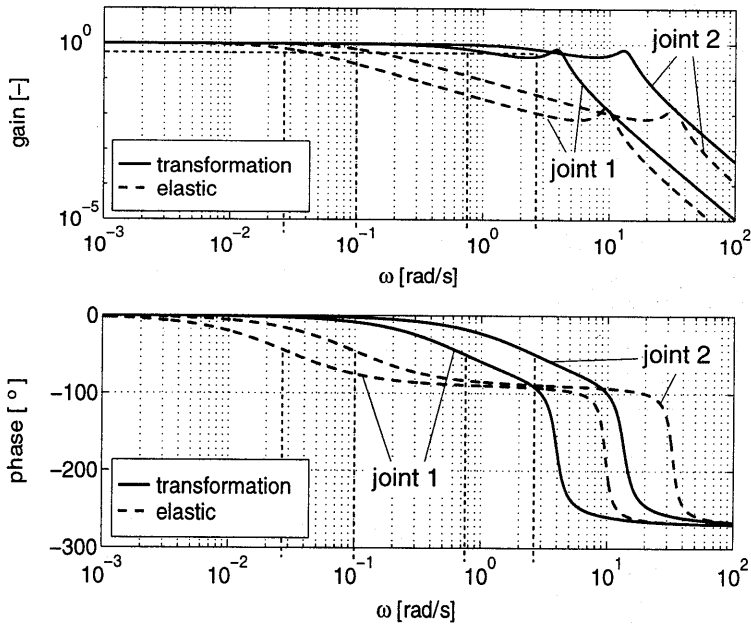
Figure 4.6: Bode plot of closed loop elastic and transformation transfer functions of joint 1 and 2

4.6 Influence of initial state estimate

To be able to compute an open loop current, the initial state, i.e. m_o, ξ_o and ϑ_o, of each SMA wire must be known at the start. Special initialisation procedures, e.g. one or more heating cycles, may provide a quite good estimate of the initial state. However, in this section it will be demonstrated that:

- the possible initial states of a wire in terms of strain, stress and temperature, are limited

- an erroneous estimate of the initial state does not influence the calculated open loop current very much

- all estimated states starting from different initial states converge to a single state after a short period of time

Consider two SMA wires of a joint. Figure 4.7 shows tensile curves of the wires (with the joint angle to describe elongation) at room temperature (lower two graphs), and at 60 °C (upper two graphs). If both wires are at room temperature, the possible angle of the actuator

and the tensile force in the wires must be in the gray area where both tensile curves overlap. The same holds for both wires at 60 °C: the angle and force must be in the area between point 3 and 4. Usually the initial temperature of the wires, being room temperature, is known as is the strain in the wires, which follows from the joint angle. The force in both wires is not known, but must be equal because of equilibrium. All possible initial states must therefore
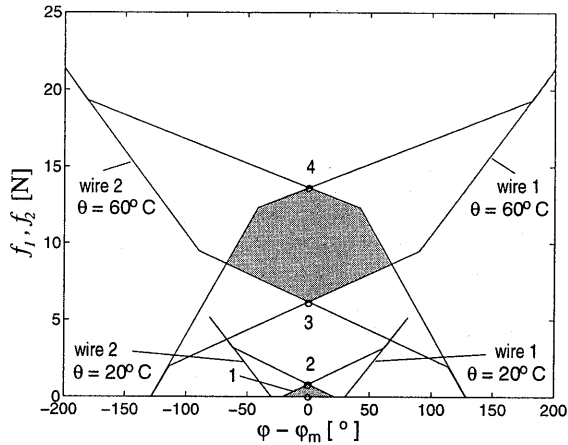
Figure 4.7: Tensile curves of two opposing SMA wires at room temperature (lower two graphs), and at 60 °C (upper two graphs). Points 1 to 4 represent four possible initial states.

be somewhere in the small, shaded area. This means that an actuator at room temperature, whatever its loading and temperature history, must have a joint angle that is at most 20° from the offset angle φ_m (when the force in both wires is zero). This is also observed in practice. Supposing that the initial (measured) joint angle is equal to φ_m (which is assumed only for convenience), the initial state of both wires must be somewhere between point 1 and 2.

To illustrate the influence of different initial estimates on the calculation of the open loop current, the open loop current is computed for the desired trajectory in Figure 4.8a, starting from the initial states 1 to 4 in Figure 4.7. For initial state 1 for both wires holds $e_o = e(\varphi_m)$, $p_o = 0$, and $\vartheta_o = \vartheta_{room}$. State 2 is defined by $e_o = e(\varphi_m)$, $\xi_o = 1$, and $\vartheta_o = \vartheta_{room}$. State 3 is defined by $e_o = e(\varphi_m)$, $\xi_o = 0$, and $\vartheta_o = 60°C$, and state 4 by $e_o = e(\varphi_m)$, $\xi_o = 1$, and $\vartheta_o = 60°C$. The desired strain and temperature for the two wires are shown in graphs (b) and (c), the open loop current in graph (d). The small horizontal parts of the open loop current at e.g. $t = 17$ s are caused by the interpolation procedure explained in Sections 2.4.3 and 3.4.2. States 1 and 2 are realistic states, while states 3 and 4 assume an initial temperature of 60 °C. Comparison between case 1 and 2 reveals that the difference in the value of all variables is quite small, and most important, that the open loop current only differs slightly during the first half period of the trajectory. But also the results for case 3 and 4 with a quite unrealistic initial state, show that after one period the differences are negligible, especially for the open loop current. Summarizing, the computed open loop current is not very sensitive to the initial

state estimate m_o, ξ_o and ϑ_o, and it is therefore not necessary to take special conditioning measures.
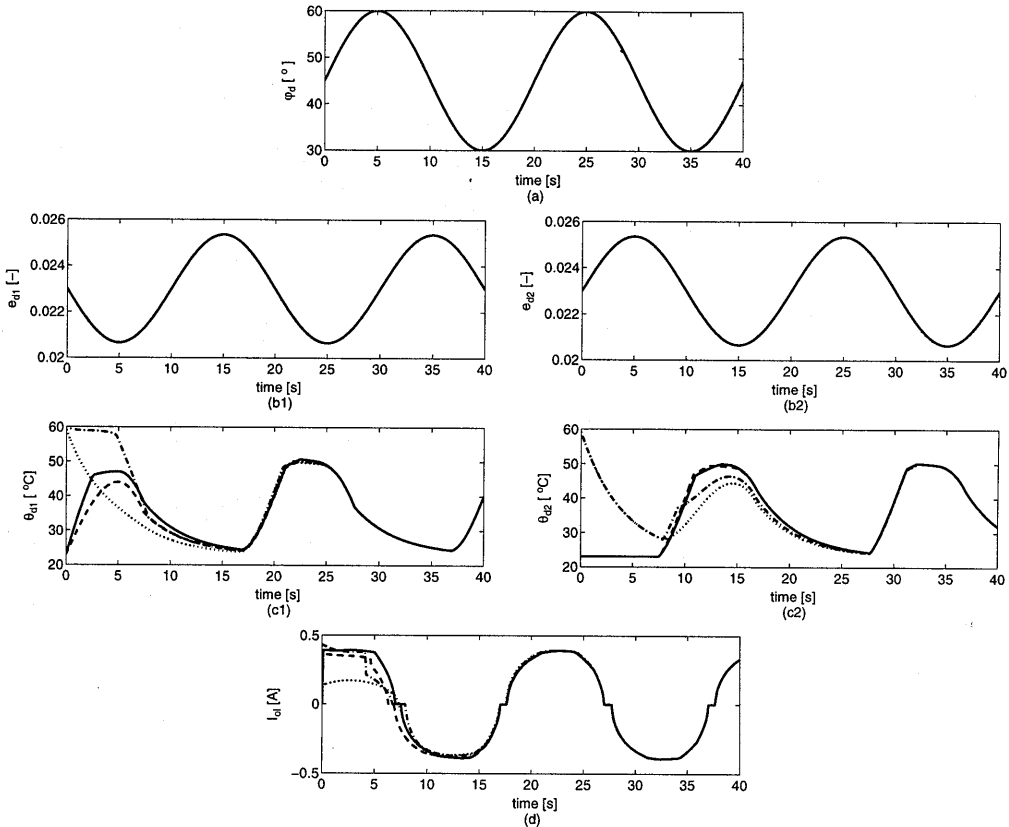
Figure 4.8: Computation of open loop current, starting from four different initial states: case 1 (solid), case 2 (dash), case 3 (dashdot), and case 4 (dot); (a) desired trajectory, (b) desired strain in wire 1 (left), and wire 2 (right), (c) desired temperatures, (d) open loop current

4.7 Tracking results

The performance of the robotic finger has been tested for three different control tasks:

- tracking of a prescribed joint trajectory $\varphi_{d1}(t)$ and $\varphi_{d2}(t)$ for each joint separately
- tracking of a prescribed end-effector trajectory $r_d(t) = [r_{dx}(t) \quad r_{dy}(t)]^T$
- position control of the end-effector under a varying tip load $F(t) = [F_x(t) \quad F_y(t)]^T$

Based on the results of Chapter 3, only two control methods were compared, unless stated otherwise: feedback alone, and feedback plus open loop, including heating dynamics.

4.7.1   Joint trajectory tracking

The control objective is to have each of the joint angles $\varphi_1(t)$ and $\varphi_2(t)$ track a desired path
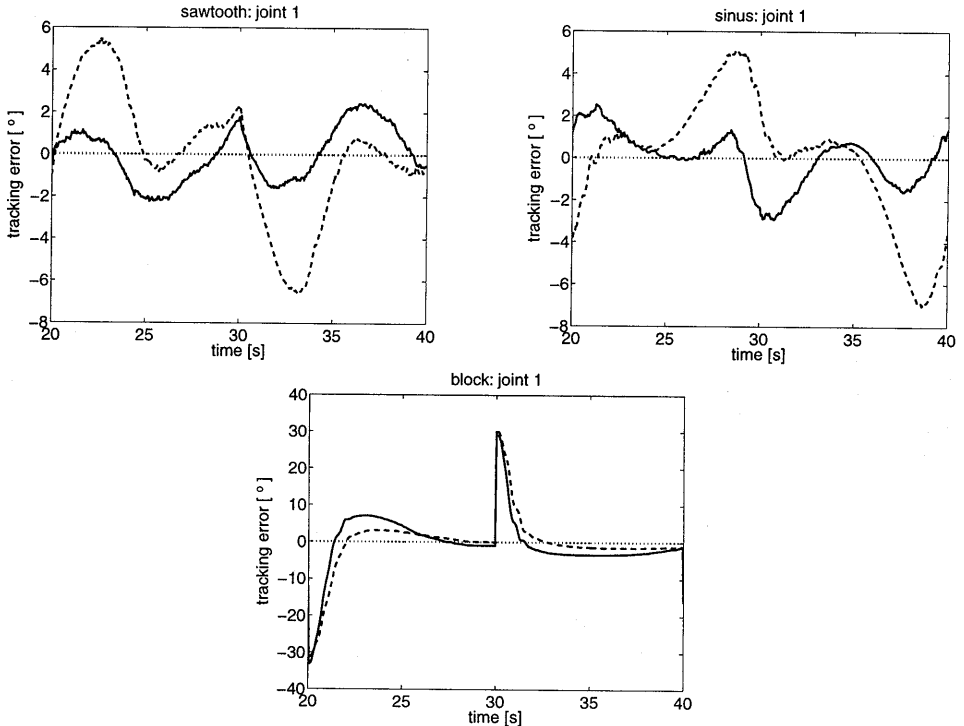
Figure 4.9: Results of three different trajectories with two different controller settings for joint 1: only feedback (1: dashed), full open loop (2: solid)

$\varphi_d(t)$, one at a time. While one joint was controlled, the other was not. Similar to the SMA actuators in the previous chapter, three trajectory shapes were applied: a sawtooth, a sinusoid, and a block shaped trajectory, with period times of 10, 20, 30 and 100 s. Figure 4.9 presents some representative results for joint 1 for a period time of 20 s. The effect of the open loop term is quite clear. The large tracking errors occurring during crossing of the hysteresis ($\dot{m} = 0$, $0 < \xi < 1$), where the PI controller has little effect, can be diminished effectively by the open loop term. The tracking results are summarized in Figure 4.10 in terms of RMS values of the tracking errors. The conclusions for each joint are equivalent to the conclusions derived for the translational actuators. The open loop term yields better tracking performance for gradual trajectories like a sawtooth and a sinusoid. However, the effect is negligible, in
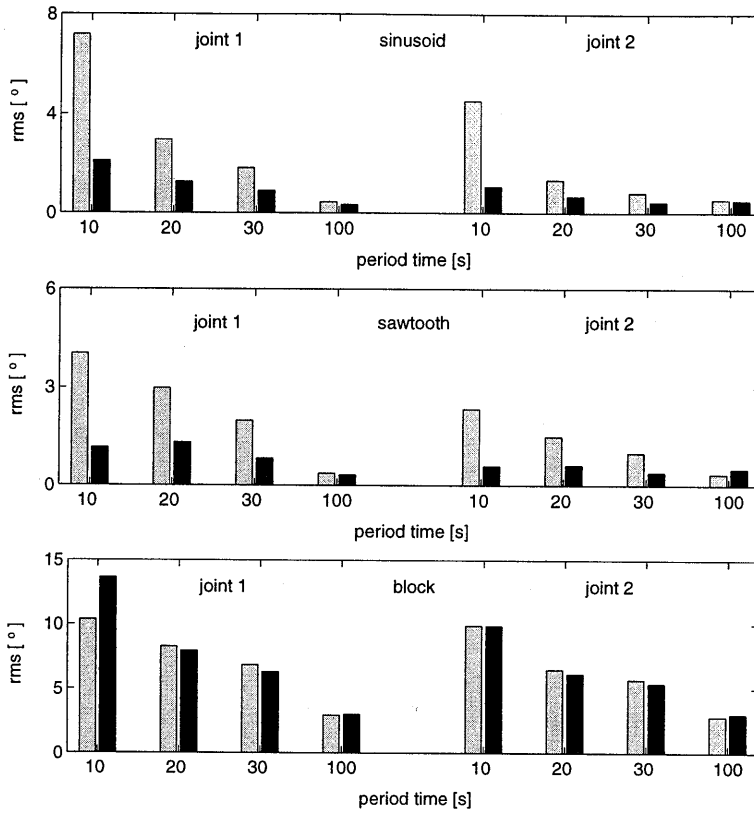
Figure 4.10: Tracking errors for three different trajectories, and two control methods; feedback alone (1: light) and open loop plus feedback (2: dark)

some cases even disadvantageous, for the block trajectory. For very slow motions (100 s), the open loop term is also of no use. The bandwidth of the PI controller is high enough to yield accurate results. Joint 2 shows a better tracking performance than joint 1, for all cases. The superior tracking capability of joint 2 resulting from its higher control gain is verified by the tracking experiments.

Position control

Tracking accuracy in the above experiments was among others limited by the measurement resolution of the AD convertor. To investigate the positioning accuracy of the robotic finger, the resolution of the angle measurements was reduced to 2.4×10^{-3} °, by decreasing the measurement range of the AD convertor. The control objective was to keep both joints at

a fixed position of 45°. Figure 4.11 shows the tracking errors during 100 seconds on an enlarged scale. Both joint angles stay within a bound of about 0.04°. This range corresponds to wire length changes of 2.1 μm. The fact that the tracking error does not converge to zero is mainly caused by thermal disturbances. A slight change in convection conditions, like a tiny breeze, has effect on the wires temperature, and therefore on the actual joint angle. The origin of the peaks in the trajectory of joint 2 is unknown; they may be caused by friction. This result demonstrates the ability to obtain small tracking errors during position control.
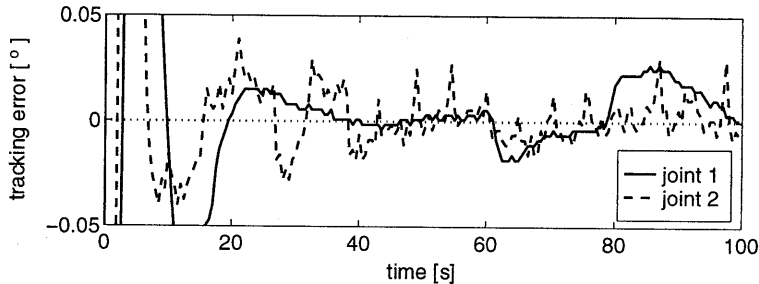
Figure 4.11: Joint position control

4.7.2   End-effector trajectory tracking

In most applications, the motion of the end-effector, instead of the joint angles, is prescribed. The joint trajectories are derived from the end-effector trajectory, using the inverse relation of Equation (4.2). Since not the end-effector coordinates are measured, but the joint angles, the feedback inputs are based on joint tracking errors. The trajectory that must be followed by the finger tip is a circle, as follows:

$$
\begin{bmatrix} r_{xd} \\ r_{yd} \end{bmatrix} = \begin{bmatrix} 135 + 10 \, \cos(2\pi t/T) \\ 145 + 10 \, \sin(2\pi t/T) \end{bmatrix}
\tag{4.12}
$$

Figure 4.12 shows tracking results for three different period times $T = 20$ s, 60 s, and 100 s. The finger tip position was not measured but reconstructed from the measured joint angles with Equation (4.2). The robotic finger is clearly unable to track a circle within 60 seconds. The tracking errors seem to be concentrated in two regions. This is only partially true. Figure 4.13 shows the desired and realized joint angles for the circle tracked in 20 seconds (left circle in Figure 4.12). Between 10 and 17 s the joint errors are large. Both joints are behind the desired path. The configuration of the robotic finger is such that if both joint angles are behind, the finger tip moves inside the circle. Between 17 and 20 s errors are smaller, resulting in better tracking of the circle. Between 20 and 25 s joint angles are large again. In this region the finger tip moves tangential to the circle, yielding apparently better tracking. However, the end-effector tracking errors are as large as in the region at the top of the circle. Finally, between 25 and 30 s, the finger tip moves inside the circle again. The largest joint
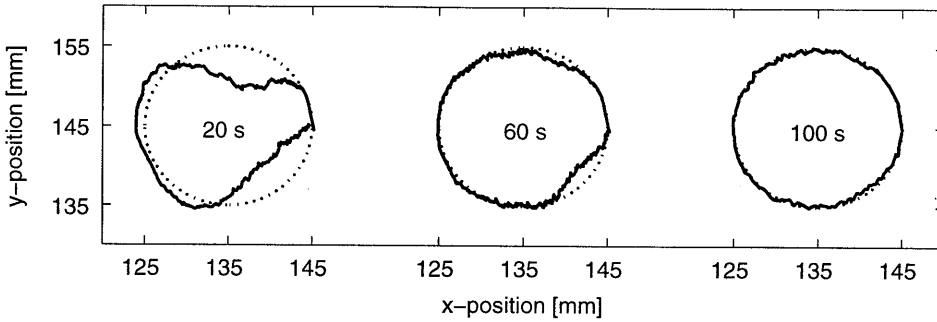
Figure 4.12: Desired (dashed) and realized (solid) end-effector trajectory with feedback controller
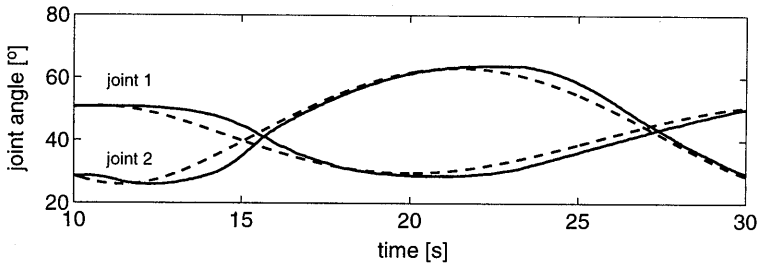
Figure 4.13: Desired (dashed) and realized (solid) joint trajectories with feedback controller ($T = 20$ s)

tracking errors occur when the joint velocity changes sign. At these moments the SMA wires behave elastically ($\dot{m} = 0$), and the feedback controller has little effect.

Figure 4.14a shows the RMS value of the joint tracking errors. At a period time of 60 seconds the RMS value is still almost 1°, which corresponds to finger tip displacements of several millimeters, depending on the exact configuration. A horizontal configuration (φ_1 close to 90°, φ_2 close to 0°) yields larger end-effector tracking errors in y-direction; in a vertical configuration the x-direction becomes worse. The position of the circle corresponds to a more or less horizontal configuration of the robotic finger. Figure 4.12 shows that indeed tracking errors especially occur in the y-direction. This is also confirmed by the RMS values of the end-effector tracking errors in Figure 4.14b. Comparison between the tracking errors in joint and end-effector space in Figure 4.14 reveals that although addition of an open loop term is beneficial for reducing the joint tracking errors, this does not automatically imply improved tracking of the end-effector. The tracking performance in y-direction becomes even worse when an open loop term is applied. The open loop term diminishes on average the joint angle tracking errors, but increases the angle tracking errors in the range where a small angle tracking error has a large effect on the y-position of the finger tip, resulting in
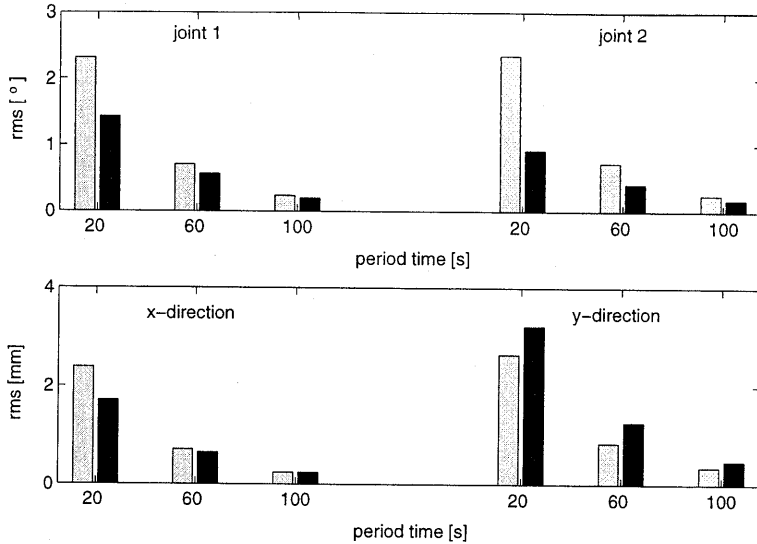
Figure 4.14: Tracking errors in joint (top) and end-effector space (bottom), using feedback (1: light) and open loop plus feedback (2: dark)

an increase of the RMS value of the y-position tracking error. It is therefore concluded that addition of the open loop term does not improve tracking performance of the robotic finger.

4.7.3 Position control with load disturbance

Until now the open loop input was based on the desired trajectory. Disturbances was taken care of by the feedback part. However, if (part of) the disturbances acting on the system are known, the open loop input can take these disturbances into account, providing the opportunity to diminish the effect of the disturbances on the tracking performance. Such disturbance attenuation is the subject of this section.

The disturbance regarded here consists of a load $\underline{F}(t) = [F_x(t) \quad F_y(t)]^T$ acting at the finger tip, see Figure 4.1. The tip load is transferred to joint torques $\underline{w}$. If the tip load is known, then the SMA actuator torques required to counterbalance the disturbance torques can be determined, see the equation of motion (4.4):

$$\underline{f}_d = -\underline{w} \tag{4.13}$$

When computing the open loop input, the system dynamics in Equation (4.9) must be substituted by Equation (4.13).

Results

The tip load is applied by means of a spring with one end attached to the tip and the other end to a driving mechanism, see Figure 4.15. The objective is to keep the tip at a fixed position
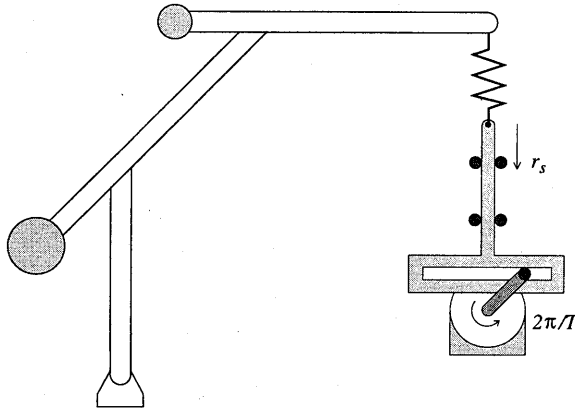
Figure 4.15: Tip load applied by means of a spring and driving mechanism

$\underline{r}_d = [r_{xd} \quad r_{yd}]^T$, corresponding to joint angles $\varphi_{1d} = 45°$ and $\varphi_{2d} = 45°$. The mechanism moves the spring end up and down in time as follows:

$$r_s(t) = 120 + 4\sin(2\pi t/T) \tag{4.14}$$

The tip load is then given by

$$\underline{F}(t) = \begin{bmatrix} 0 \\ k_s\left(r_s(t) + l_{s,ref} - r_{yd}\right) \end{bmatrix} \tag{4.15}$$

The spring properties are $k_s = 4$ N/m and $l_{s,ref} = 50$ mm.

Figure 4.16 shows the response of the joint angles, when the robotic finger is subjected to a disturbance with a period time of 10 seconds. The dashdotted line represents the uncontrolled response. Joint 1 is disturbed more than joint 2, because of the larger distance of the tip load to joint 1. Also shown are the joint motions of the controlled robotic finger. Both control laws succeed in keeping the joint angles around their desired value. The open loop plus feedback controller is more successful in reducing the disturbance amplitude than the feedback controller.

Figure 4.17 demonstrates the positive effect of adding an open loop term on the tracking error for different period times. Especially joint 1 benefits from the open loop term. The effect is smaller for joint two, probably because the disturbance torque resulting from the tip load is higher for joint one than for joint two.
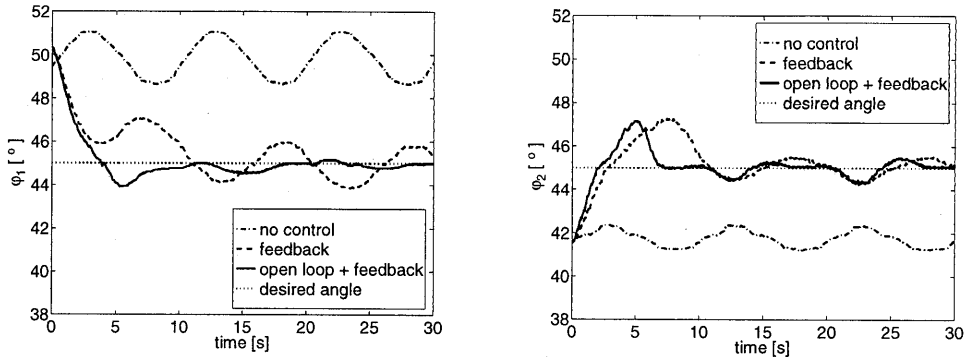
Figure 4.16: Response of robotic finger to tip load
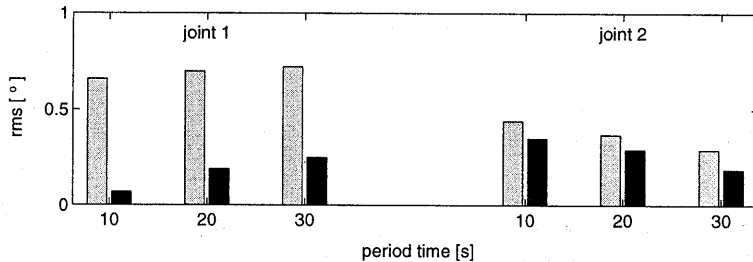
Figure 4.17: Position errors during disturbance attenuation, using feedback control (1: light), and open loop plus feedback control (2: dark)

4.8   Conclusions

In this chapter the performance of an SMA driven, two joint robotic finger was investigated. Both joints are actuated in a differential way. Joint trajectory tracking and disturbance attenuation is improved by adding an open loop term to the PI feedback controller. However, this does not hold for end-effector tracking. The closed loop bandwidth of the robotic finger is seriously limited by the relatively large link inertias, which combined with the elasticity of the SMA wires yield resonance frequencies which are quite low. To avoid instability the control gains must remain quite small.

5   Active shape control of SMA reinforced materials

5.1   Introduction

Active shape control of flexible structures offers the opportunity to change the shape at any moment during service, and correct shape errors caused by external disturbances or imperfect production. Examples of applications with these so-called *adaptive* materials are wings to improve aerodynamic lift and reduce drag (Barrett, 1992; Austin et al., 1994), submarine fins to improve the lift (Beauchamp et al., 1992), (helicopter) rotor blades to increase hub lift and reduce vibrations due to imbalance (Chen and Chopra, 1997), and reflector surfaces to improve the antenna performance by optimizing the reflector shape despite mechanical and thermal disturbances (Paradies et al., 1996). Depending on the time scale, active shape control of structures and materials can be regarded either as vibration control or as quasi-static shape control. The latter is the subject of this chapter.

5.1.1   Property control

Most of the research on SMA reinforced materials focuses on property control, like variable stiffness, and therefore on the dynamic behaviour of the composite materials. The (numerical) investigations on this subject are either based on a micromechanical basis or the SMA actuators and the host material are considered as separate parts. While the micromechanical approach is able to predict average material properties, like elastic modulus and transformation temperatures, macroscopic models are able to describe changes in shape and dynamic properties. Both approaches will be discussed here.

    Several authors used micromechanical averaging techniques to arrive at constitutive relations describing the thermo-mechanical behaviour of SMA composite materials. The SMA component is regarded as an indistinguishable part of the material. The differences between the models are found in the averaging techniques applied. They all need a three-dimensional SMA constitutive model, at which point they all fail for the reasons explained in Section 2.2.2. When the SMA is subjected to a compressive load, for example during unloading after stretching (and AM transformation of the SMA), all models yield incorrect results because of

the chosen constitutive models. Boyd and Lagoudas (1994) used such an averaging approach to determine the overall properties of an SMA composite material. Their three-dimensional SMA model is an extension of Tanaka's exponential 1D model, see Equations (2.12-2.13). The isothermal shape recovery reported by Boyd and Lagoudas is purely the result of the earlier mentioned model flaw. Also the absence of shape recovery during transverse loading found by Lagoudas et al. (1994), is due to this flaw. Saravanos et al. (1995) applied an alternative homogenisation method, but the same transformation kinetics law for the martensite fraction. They found a non-monotonic stress-strain curve during isothermal unloading, where it should be monotonically decreasing. Sullivan (1994) used a third averaging method, and adapted the cosine kinetics law of Liang and Rogers, but encountered the same problems as the previous authors.

Macroscopic property changes can also be modeled by regarding the SMA actuators as a separate part of the structure. Ro and Baz (1995a,b,c) investigated the buckling properties and resonance frequencies of a NiTi-glass/polyester plate. The plate was modeled with shell elements. The temperature distribution in the plate caused by heating several wires was supposed to be uniform over the thickness. The NiTi wires were modeled as external forces. Experimentally obtained recovery force - temperature curves were used to prescribe the magnitude of the forces. Brinson and Lammering (1993) presented a FE formulation for SMA wires, considering them as one-dimensional trusses, and combined these truss elements with beam elements to calculate the dynamic properties of a cantilever beam as a function of temperature.

Very few models consider the three- or even two-dimensional temperature distribution in an SMA composite material. Most of the models assume a prescribed temperature distribution, or assume temperature to be uniform over the thickness. One of the exceptions is given by Baz and Chen (1993), who studied the properties of a polyurethane shaft reinforced with SMA wires. They assumed the temperature distribution to be two-dimensional in the cross-section. The temperature field resulting from resistive heating of the SMA wires was used to compute the torsional stiffness of the shaft.

5.1.2   Shape control

Piezo-electric materials

Both piezoelectric patches and shape memory alloy wires or plates may serve as inplane actuators. They are either attached to the surface, or embedded in the host material. The use of piezoelectric actuators for shape control is investigated more extensively than the use of shape memory alloys. Possible reasons for this are, e.g. the less complicated constitutive behaviour of piezoelectric materials compared to shape memory alloys and the fact that control of the input variable of piezoelectric materials (voltage) is easier than the input variable of shape memory alloys (temperature). Barrett (1992) succeeded in changing the twist and lift coefficient of a wing using piezo actuators. He analyzed the shape change as a function of the voltage applied, but did not really control the shape. Chaudhry and Rogers (1993) investigated the bending of a cantilever beam actuated by piezoelectric patches. Chandra and Chopra (1993), and Donthireddy and Chandrashekhara (1996) presented a FE model and nu-

merical results for a composite beam with embedded piezoelectric layers. The shape change as a function of applied voltage was computed. Similar computations on a plate were performed by Ghosh and Batra (1995). Koconis et al. (1994a) derived analytical relations to determine the shape change of sandwich structures with piezoelectric actuators as a function of applied voltage.

The inverse problem, i.e. the determination of voltages needed to achieve a specified shape, was investigated by Agrawal and Tong (1994). They focused on shape control of a cantilever beam with several piezoceramic patches. The voltages to be applied were derived with a finite difference model. Koconis et al. (1994b) solved the inverse problem analytically. Paradies et al. (1996) focused on shape control of an adaptive mirror using piezoelectric patches to compensate gravity distortion. The voltages to be applied for different gravity conditions were derived with a FE model. The validity of this method was tested in practice, and showed a 80% shape error reduction.

Shape control of SMA reinforced materials

Research on shape control with SMA's is still quite limited. Chaudhry and Rogers investigated experimentally the bending of a cantilever beam actuated by externally applied SMA wires (1991), and SMA wires inside sleeves (1992). Brinson et al. (1997) calculated the shape change of a cantilever beam with an externally attached SMA wire with temperature as input variable. Hebda et al. (1995) measured deflections of a NiTi-epoxy/carbon composite upon heating.

It can be concluded that accurate modeling of the shape change of SMA reinforced materials as a result of heating of the SMA wires is not yet investigated thoroughly. This is even more true for active shape control of SMA reinforced materials. This chapter will address both topics.

The mechanical behaviour of SMA composites depends heavily on the temperature field in the matrix material. This temperature field is the result of electrical heating of the SMA wires. To accurately describe the shape change of an SMA composite as function of the electrical current applied, a finite element model was developed and implemented in the package MARC (MARC, 1994). It serves not only to determine the response of an SMA composite to an electric current, but also offers the possibility to calculate the electric current necessary to obtain a desired shape. This model-based open loop current is determined off-line and can be used to improve active shape control in experiments.

This chapter presents the FEM equations to be solved. Special emphasis is put on the implementation of the SMA wire elements. The model is used to calculate the shape change of a cantilever beam. It will be shown that an acceptable approximation of the deformation can be determined with a simplified model. The determination of the open loop current is based on this simplified model. Active shape control of an SMA composite frame is the subject of the remaining part of the chapter. The experimental setup and results will be presented.

5.2   Model equations

Consider a body Ω with a boundary Γ with unit outward normal $\vec{n}$. The position vector of a material point in Ω in the undeformed configuration is denoted by $\vec{x}_o$, and in the current configuration by $\vec{x}$. The deformation of the body with respect to the undeformed reference configuration is described with the deformation tensor $\boldsymbol{F}$:

$$\boldsymbol{F} = \boldsymbol{F}(\vec{x}_o, t) = (\vec{\nabla}_o \vec{x})^c = \boldsymbol{I} + (\vec{\nabla}_o \vec{q})^c \tag{5.1}$$

where $\vec{\nabla}_o$ is the gradient operator with respect to the undeformed configuration (Chadwick, 1976), and $\vec{q} = \vec{x} - \vec{x}_o$ is the displacement of the material point $\vec{x}_o$. In every material point the balance laws of mass, momentum, moment of momentum, and energy must be satisfied. When inertia terms and body forces like gravity are neglected, they are given by:

$$J\rho = \rho_o \tag{5.2}$$

$$\vec{\nabla}.\boldsymbol{\sigma} = \vec{0} \tag{5.3}$$

$$\boldsymbol{\sigma} = \boldsymbol{\sigma}^c \tag{5.4}$$

$$\rho\dot{e} + \vec{\nabla}.\vec{h} = r \tag{5.5}$$

where $J = \det(\boldsymbol{F})$ is the volume change factor, $\vec{\nabla}$ is the gradient operator with respect to the current configuration, $\boldsymbol{\sigma}$ is the Cauchy stress tensor, e the internal energy, $\vec{h}$ the heat flux, and r the generated heat per unit volume. Because of the possibly large deformations and rotations, the chosen strain measure is the rotation invariant Green-Lagrange strain tensor $\boldsymbol{E}$:

$$\boldsymbol{E} = \tfrac{1}{2}(\boldsymbol{F}^c.\boldsymbol{F} - \boldsymbol{I}) \tag{5.6}$$

To arrive at a complete set of equations, constitutive relations for $\boldsymbol{\sigma}$, e and $\vec{h}$ have to be specified.

5.2.1   Constitutive equations

Mechanical part

For the thermo-elastic matrix material the Cauchy stress tensor $\boldsymbol{\sigma}$ is given by:

$$\boldsymbol{\sigma} = \tfrac{1}{J}\boldsymbol{F}.\boldsymbol{P}(\boldsymbol{E}, \vartheta).\boldsymbol{F}^c \tag{5.7}$$

where $\boldsymbol{P}$, the second Piola-Kirchhoff stress tensor, depends on $\boldsymbol{E}$ and the temperature ϑ. The matrix material is assumed to be isotropic and linear, so

$$\boldsymbol{P} = \frac{D}{1+\nu}\left\{\boldsymbol{E} + \frac{\nu}{1-2\nu}\text{tr}(\boldsymbol{E})\boldsymbol{I} - \frac{1+\nu}{1-2\nu}\alpha\,(\vartheta - \vartheta_o)\boldsymbol{I}\right\} \tag{5.8}$$

where D, ν and α are the elastic modulus, Poisson's ratio and thermal expansion coefficient.
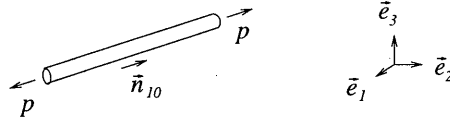
Figure 5.1: Definition of stress and heat flux in an SMA wire

The stress field in the SMA wires is assumed to be one-dimensional, meaning that $\boldsymbol{P}$ can be written as $\boldsymbol{P} = p\,\vec{n}_{10}\,\vec{n}_{10}$, where $\vec{n}_{10}$ is the unit vector tangent to the wire in the reference configuration, see Figure 5.1. Furthermore, it is assumed that the 2nd Piola-Kirchhoff stress p, called the axial stress, is related to the Green-Lagrange strain e and the temperature ϑ by the constitutive model outlined in Chapter 2.

Thermal part

The thermal behaviour of both matrix material and SMA wires is assumed to be isotropic, and can be described by the same relations. The heat flux in a solid is related to the temperature gradient by Fourier's law

$$\vec{h} = \tfrac{1}{J}\boldsymbol{F}.\vec{h}_o \qquad ; \qquad \vec{h}_o = -\kappa\vec{\nabla}_o\vartheta \tag{5.9}$$

where κ is the thermal conductivity. Besides, it is assumed that the rate of internal energy is given by

$$\dot{e} = c_p\dot{\vartheta} \tag{5.10}$$

where c_p is the specific heat.

Because of the high conductivity and small dimensions of the SMA wires with respect to the matrix material, the temperature distribution in a cross-section of an SMA wire is almost uniform. It is assumed that the heat transfer between SMA wires and matrix material is perfect.

5.2.2   Finite Element formulation

In general it is impossible to find a solution $(\vec{q}, \vartheta)$ such that the balance equations are satisfied in every point. To arrive at a solvable set of equations, the balance laws and constitutive relations are transformed into a weak form using the weighted residuals approach. The weak form of the balance laws Equations (5.3) and (5.5) is

$$\int_\Omega \vec{w}_q.\vec{\nabla}.\boldsymbol{\sigma}\,d\Omega = 0 \qquad\qquad \forall\,\vec{w}_q \tag{5.11}$$

$$\int_\Omega w_\vartheta\{\rho\dot{e} + \vec{\nabla}.\vec{h} - r\}d\Omega = 0 \qquad\qquad \forall\,w_\vartheta \tag{5.12}$$

with weighting functions $\vec{w}_q$ and w_ϑ. Applying Gauss' theorem yields:

$$\int_\Omega (\vec{\nabla}\vec{w}_q)^c : \boldsymbol{\sigma}\, d\Omega = \int_\Gamma \vec{w}_q.\vec{t}\, d\Gamma \qquad\qquad ; \qquad \vec{t} = \boldsymbol{\sigma}.\vec{n} \quad \forall\, \vec{w}_q \quad (5.13)$$

$$\int_\Omega \{w_\vartheta \rho\dot{e} - \vec{\nabla}w_\vartheta.\vec{h}\}\, d\Omega = \int_\Omega w_\vartheta r\, d\Omega - \int_\Gamma w_\vartheta \pi\, d\Gamma \qquad ; \qquad \pi = \vec{h}.\vec{n} \quad \forall\, w_\vartheta \quad (5.14)$$

where $\vec{t}$ and π are the mechanical and thermal boundary loads respectively. These equations are discretized in space by means of the finite element method. First the integrals on the left hand side are transformed to the reference configuration. Next the reference volume Ω_o is subdivided in n_e elements. Using Galerkin's approach, the displacement vector $\vec{q}$, temperature ϑ, and corresponding weighting functions $\vec{w}_q$ and w_ϑ in each element Ω_o^e are discretized as

$$\begin{aligned}
\vec{q}(\vec{x}_o, t) &= \underset{\sim}{N}_q^T(\vec{x}_o)\vec{q}^e(t) \quad ; \quad &\vec{w}_q(\vec{x}_o, t) &= \underset{\sim}{N}_q^T(\vec{x}_o)\vec{w}_q^e(t) & &\\
\vartheta(\vec{x}_o, t) &= \underset{\sim}{N}_\vartheta^T(\vec{x}_o)\underset{\sim}{\vartheta}^e(t) \quad ; \quad &w_\vartheta(\vec{x}_o, t) &= \underset{\sim}{N}_\vartheta^T(\vec{x}_o)\underset{\sim}{w}_\vartheta^e(t) & &\forall\, \vec{x}_o \in \Omega_o^e \quad (5.15)
\end{aligned}$$

where $\vec{q}^e$ and $\underset{\sim}{\vartheta}^e$ are columns of nodal displacements and temperatures at element level, and $\underset{\sim}{w}_q^e$ and $\underset{\sim}{w}_\vartheta^e$ are columns of nodal weighting functions. The components of $\underset{\sim}{N}_q$ and $\underset{\sim}{N}_\vartheta$ are the chosen shape functions. Using these expressions, the integrals in Equations (5.13-5.14) can be written as

$$\sum_{e=1}^{n_e} \vec{w}_q^{e\,T}\cdot \int_{\Omega_o^e} \vec{B}_q.\boldsymbol{P}.\boldsymbol{F}^c\, d\Omega_o = \sum_{e=1}^{n_e} \vec{w}_q^{e\,T}\cdot \int_{\Gamma^e} \underset{\sim}{N}_q\, \vec{t}\, d\Gamma \qquad\qquad \forall\, \vec{w}_q^e \quad (5.16)$$

$$\sum_{e=1}^{n_e} \underset{\sim}{w}_\vartheta^{e\,T} \int_{\Omega_o^e} \left\{ \underset{\sim}{N}_\vartheta \rho_o c_p \underset{\sim}{N}_\vartheta^T \underset{\sim}{\dot{\vartheta}}^e + \kappa \vec{B}_\vartheta.\vec{B}_\vartheta^T \underset{\sim}{\vartheta}^e \right\} d\Omega_o =$$

$$\sum_{e=1}^{n_e} \underset{\sim}{w}_\vartheta^{e\,T} \left\{ \int_{\Omega^e} \underset{\sim}{N}_\vartheta\, r\, d\Omega - \int_{\Gamma^e} \underset{\sim}{N}_\vartheta\, \pi\, d\Gamma \right\} \quad \forall\, \underset{\sim}{w}_\vartheta^e \quad (5.17)$$

where $\vec{B}_q$ and $\vec{B}_\vartheta$ contain the gradients $\vec{\nabla}_o \underset{\sim}{N}_q$ and $\vec{\nabla}_o \underset{\sim}{N}_q$ of the shape functions respectively. Introducing the global counterparts of the element nodal variables

$$\underset{\sim}{q} = [\vec{q}_1 \ldots \vec{q}_n]^T \qquad\qquad ; \qquad\qquad \underset{\sim}{w}_q = [\vec{w}_{q1} \ldots \vec{w}_{qn}]^T \qquad\qquad (5.18)$$

$$\underset{\sim}{\vartheta} = [\vartheta_1 \ldots \vartheta_n]^T \qquad\qquad ; \qquad\qquad \underset{\sim}{w}_\vartheta = [w_{\vartheta 1} \ldots w_{\vartheta n}]^T \qquad\qquad (5.19)$$

with n the number of nodes, the global set of finite element equations can be obtained from Equations (5.16-5.17) by assembly, yielding

$$\underset{\sim}{w}_q^T \cdot \vec{f}_{in} = \underset{\sim}{w}_q^T \cdot \vec{f}_{ex} \qquad\qquad \forall\, \vec{w}_q \qquad\qquad (5.20)$$

$$\underset{\sim}{w}_\vartheta^T \{\underset{\sim}{C}\underset{\sim}{\dot{\vartheta}} + \underset{\sim}{A}\underset{\sim}{\vartheta}\} = \underset{\sim}{w}_\vartheta^T \{\underset{\sim}{R} + \underset{\sim}{Q}\} \qquad\qquad \forall\, \vec{w}_\vartheta \qquad\qquad (5.21)$$

where the definitions of the introduced columns and matrices are obvious. These relations must hold for arbitrary values of $\vec{w}_q$ and w_ϑ, so $\vec{f}_{in} = \vec{f}_{ex}$ and $\underset{\sim}{C}\underset{\sim}{\dot{\vartheta}} + \underset{\sim}{A}\underset{\sim}{\vartheta} = \underset{\sim}{R} + \underset{\sim}{Q}$. Writing

the force vectors with respect to an orthonormal base $\vec{e} = [\vec{e}_1 \ \vec{e}_2 \ \vec{e}_3]^T$ finally yields

$$\underset{\sim}{f}_{in} = \underset{\sim}{f}_{ex} \tag{5.22}$$

$$\underline{C}\dot{\underset{\sim}{\vartheta}} + \underline{\Lambda}\underset{\sim}{\vartheta} = \underset{\sim}{R} + \underset{\sim}{Q} \tag{5.23}$$

Equations (5.22-5.23) represent a set of $3n$ (in a 3D space) algebraic, and n first order differential equations. To arrive at a set which can be solved, they have to be supplemented with an appropriate set of initial and boundary conditions.

For the initial conditions it is assumed that

$$\underset{\sim}{q}(0) = \underset{\sim}{0} \qquad ; \qquad \underset{\sim}{\vartheta}(0) = \underset{\sim}{\vartheta}_\infty \tag{5.24}$$

where ϑ_∞ is the temperature of the surrounding medium.

Mechanical boundary conditions are either external loads or prescribed displacements. Thermal boundary conditions consist of zero heat fluxes at insulation boundaries, e.g. because of symmetry, or of convective heat loss to the surrounding medium. The corresponding boundary condition relates the normal heat flux to the surface temperature ϑ_s:

$$\pi = H(\vartheta_s - \vartheta_\infty) \tag{5.25}$$

where H is the convective heat transfer coefficient.

Solution procedure

Time integration is performed with a first order implicit Euler scheme with time step $\Delta t = t_i - t_{i-1}$, $i = 1, \ldots, n_{inc}$. Suppose the displacements $\underset{\sim}{q}_{i-1} = \underset{\sim}{q}(t_{i-1})$ and temperatures $\underset{\sim}{\vartheta}_{i-1} = \underset{\sim}{\vartheta}(t_{i-1})$ are known. Then $\underset{\sim}{\vartheta}_i$ has to be determined using

$$\underset{\sim}{\vartheta}_i = \underset{\sim}{\vartheta}_{i-1} + \Delta t \dot{\underset{\sim}{\vartheta}}_i \qquad ; \qquad \underline{C}\dot{\underset{\sim}{\vartheta}}_i = \underset{\sim}{R}_i + \underset{\sim}{Q}_i - \underline{\Lambda}\underset{\sim}{\vartheta}_i \tag{5.26}$$

The backward difference algorithm is unconditionally stable, and yields accurate results if the time step is not too large (Zienkiewicz and Taylor, 1989). After some rearrangement the Equations (5.22) and (5.26) can be written as

$$\underset{\sim}{f}_{in,i}(\underset{\sim}{q}_i, \underset{\sim}{\vartheta}_i) = \underset{\sim}{f}_{ex,i} \tag{5.27}$$

$$\{\tfrac{1}{\Delta t}\underline{C} + \underline{\Lambda}\}\underset{\sim}{\vartheta}_i = \underset{\sim}{R}_i + \underset{\sim}{Q}_i + \tfrac{1}{\Delta t}\underline{C}\underset{\sim}{\vartheta}_{i-1} \tag{5.28}$$

with unknowns $\underset{\sim}{q}_i$ and $\underset{\sim}{\vartheta}_i$. These equations are solved in two stages. First the temperature distribution at t_i is solved with Equation (5.28). This equation is linear and solution is therefore straightforward. Next, the displacement field must be determined from Equation (5.27) using the temperatures $\underset{\sim}{\vartheta}_i$. Equation (5.27) is non-linear due to, for instance, the non-linear constitutive behaviour of the SMA wires. Therefore it is solved in an iterative way, using the Newton-Raphson procedure.

The unknown displacements q_i are written as the sum of an estimate $q_{i,j-1}$ obtained in the previous iteration step, and an error $\delta q_{i,j}$. Taylor series expansion of the internal forces f_{in} results in

$$f_{in,i}(q_i, \vartheta_i) = f_{in,i,j-1}(q_{i,j-1}, \vartheta_i) + K_{i,j-1}\delta q_{i,j} + O(\delta q_{i,j}^2) \qquad (5.29)$$

where $K_{i,j-1}$ is the stiffness matrix

$$(K_{i,j-1})_{m,n} = \left.\frac{\partial f_{in,m}}{\partial q_n}\right|_{q_{i,j-1}, \vartheta_i}$$

Substitution of Equation (5.29) in Equation (5.27) and neglecting higher order terms yields

$$K_{i,j-1}\delta q_{i,j} = f_{ex,i} - f_{in,i,j-1} \qquad (5.30)$$

Solving this set yields a new approximation for the displacements: $q_{i,j} = q_{i,j-1} + \delta q_{i,j}$. The iteration process has converged when some measure of $\delta q_{i,j}$ and the residuals, i.e. the right hand side of Equation (5.30) is below a specified limit.

5.2.3   SMA element contribution to the FEM equations

The SMA wires are modeled as two node, one-dimensional trusses. The matrix material is modeled with three-dimensional, twenty node, quadratic brick elements. The nodes of the SMA truss elements are attached to nodes of brick elements. Figure 5.2 shows the FEM model of an SMA composite. The presence of SMA elements affects the equations (5.30).
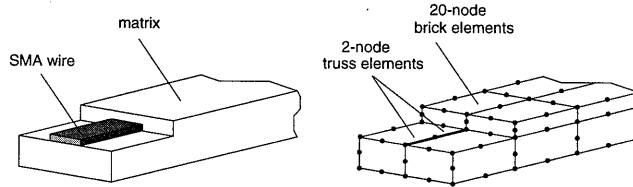
Figure 5.2: SMA composite in reality (left), and in FEM (right)

When a new estimate of the nodal displacements $q_{i,j}$ has been determined, the strain $e_{i,j}$ in each SMA element is computed. The stress $p_{i,j}$ and internal variables $m_{i,j}$ and $\xi_{i,j}$ in each SMA truss element are then determined using the algorithm explained in Chapter 2. The contribution of an SMA truss element to the global stiffness matrix $K_{i,j}$ consists of the momentary modulus $C_{i,j} = \partial p/\partial e$, that follows from Equations (2.24-2.25):

$$C_{i,j} = \frac{p_2(\vartheta_i) + p_4(\vartheta_i)m_{i,j}}{e_2(\vartheta_i) + e_4(\vartheta_i)m_{i,j}} \qquad \text{during elastic response} \qquad (5.31)$$

$$C_{i,j} = \frac{p_3(\vartheta_i) + p_4(\vartheta_i)\xi_{i,j}}{e_3(\vartheta_i) + e_4(\vartheta_i)\xi_{i,j}} \qquad \text{during AM and MA transformation} \qquad (5.32)$$

With these values for the stress and modulus the element stiffness matrix and the internal forces are updated at the end of each iteration. At the first iteration of each increment, the stress is based on the strain e_{i-1} at the end of the previous increment and the temperature ϑ_i at the end of the current increment. A special subroutine has been developed to determine the stress p and momentary modulus C in every SMA element at each iteration step.

5.3 SMA composite cantilever beam

The SMA composite structure that was used for the experimental and numerical investigations is a flexible cantilever beam, consisting of two pairs of NiTi wires embedded in a polypropylene (PP) matrix, as shown in Figure 5.3. The beam dimensions are $L = 166$ mm, $W = 8.5$ mm, and $T = 1.6$ mm. The polypropylene was modified with 10 weight % maleic acid to improve the bonding with the NiTi wires. The NiTi wires have a rectangular cross-section of 0.1x0.6 mm^2, and are positioned approximately 0.1 mm below the surface of the beam. The offset distance from the neutral axis d is therefore 0.7 mm. Before embedding
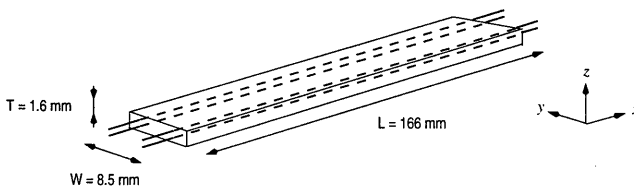
Figure 5.3: Flexible SMA composite cantilever beam

the NiTi wires, they are stretched to a strain e_o of 2.2%. According to the constitutive model this strain corresponds with a martensite fraction of 0.5. The upper two wires are connected in series electrically. This is the case also for the lower two wires. When for example the upper wires are heated, they try to return to their original, smaller, length. However, because the wires are embedded in the matrix material, contraction is accompanied with a considerable increase of the force in the wires. Since the wires are located at an offset distance from the neutral axis, a bending moment is exerted on the beam, which causes the beam to bend upwards. Because of this, the wires at the lower side of the beam are stretched, yielding a resisting moment. When the wires at the lower side are heated, the beam bends downwards. Thus, by supplying the wires with an appropriate electric current, the shape of the beam can be controlled actively.

5.3.1 FEM simulations

The FEM model described in the previous section is used to examine the thermo-mechanical behaviour of the cantilever beam. The beam is divided in $10 \times 4 \times 5$ matrix elements in, respectively, the x, y and z direction, and each of the SMA wires consists of 20 truss elements.

5.3.2   Determination of thermal parameters

The value of the specific heat and thermal conductivity of the matrix material, and the convective heat transfer coefficient, have a large influence on the temperature distribution in the SMA composite. It is therefore important to have accurate values for these parameters. The effect of the NiTi thermal parameters is of lesser importance, because of the small dimensions of the NiTi wires. The convective heat transfer coefficient depends on many variables, like the type and velocity of the surrounding medium, the geometry of the solid and its orientation. The values of the specific heat and conductivity of the PP matrix, and of the heat transfer
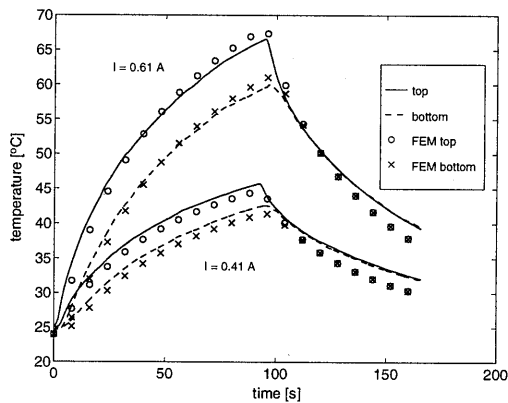
Figure 5.4: Experimentally and numerically obtained temperature at the top and bottom surface of an SMA composite beam

coefficient H were determined experimentally. The transient temperature at the centre of the top and bottom surface of the cantilever beam was measured during several minutes, while heating the two NiTi wires at the top with a constant current. These measurements were performed for several currents, ranging from 0.1 A to 0.61 A. The same process was simulated with the thermal part of the FEM model. The thermal parameters were then fitted on a trial-and-error basis. Figure 5.4 shows two experimental temperature transients, and the corresponding numerical results using the fitted parameters. The material properties are listed in Table 5.9. The convective heat transfer coefficient was determined to be 22 $W.m^{-2}.K^{-1}$.

5.3.3   Steady state response

First the steady state response of the beam was examined for different values of the electric current. Only the two upper wires were heated. Figure 5.5 shows the calculated stress and temperature along the top and bottom wires for electric currents of 0.3 A and 0.6 A. The graphs show a uniform temperature and stress distribution in the wires. Edge effects are limited to a small region. All generated heat flows perpendicular to the wires to the surface. Only in a very small region at the edges the heat also flows parallel to the wires towards the

Table **5.9**: Material parameters

material parameter	symbol	value		unit
		PP	NiTi	
Young's modulus	D	1.5		GPa
Poisson ratio	ν	0.3		-
mass density	ρ_o	900	6700	kg.m^{-3}
specific heat	c_p	2500	530	J.kg^{-1}.K^{-1}
thermal conductivity	κ	0.15	56	W.m^{-1}.K^{-1}
electric resistivity	r_{el}		1.5	$\times 10^{-6}$ Ω.m

surface. The tensile stress in the wires increases from zero at the ends to a constant value in the centre region. The length of the transient part, where the tensile stress changes noticeable with position, depends among others on the stiffness of wires and matrix, and their cross-sectional areas, as was demonstrated by Lagoudas and Tadjbakhsh (1992). They used the
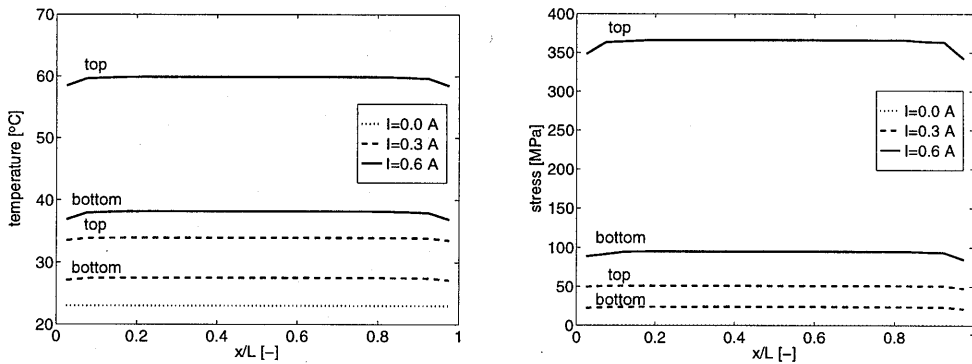
Figure **5.5**: Stress and temperature in SMA wires

so-called approximate analytical shear-lag model to determine the stress in an SMA wire that is embedded in a flexible rod. The length of the transient part calculated with their model, is in the order of several millimeters at maximum. Bideaux et al. (1995) investigated the axial stress build up in an SMA wire near the edges of the matrix material with a two-dimensional FEM model. They also concluded that the stress build up is concentrated in a very small region. The results found with the three-dimensional model in this thesis agree very well with literature.

The large stress in the top wires for $I = 0.6$ A is caused by the fact that the temperature

of the top wires (60°C) is above A_s and therefore the reverse MA transformation has started, yielding a high recovery stress.

Since the tensile stresses in the SMA wires are almost constant over the length of the beam, the entire beam is loaded with a constant bending moment, causing a constant curvature Ψ. Referring to Figure 5.6, equilibrium of the bending moments caused by the SMA wires,
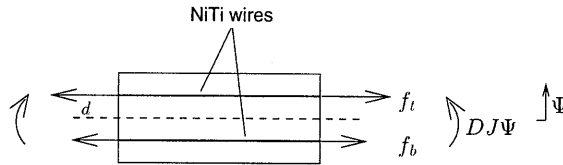
Figure 5.6: Bending moments acting on a cross-section

and by the matrix material, yields an expression for the curvature of the beam:

$$DJ\Psi = 2d\{f_t(\vartheta_t, \Psi) - f_b(\vartheta_b, \Psi)\} \tag{5.33}$$

where J is the area moment of inertia of the beam. The subscripts t and b refer to the top wires and the bottom wires, respectively. When the temperatures ϑ_t and ϑ_b are known, this equation
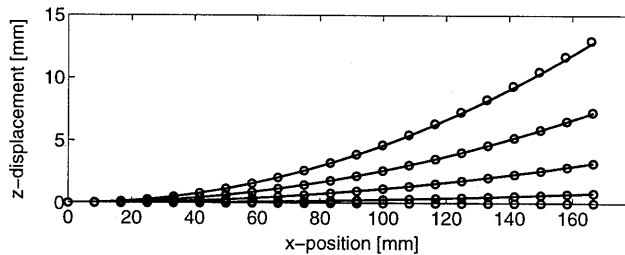
Figure 5.7: Analytical and FEM calculation of deformed beam

can be solved iteratively. The circles in Figure 5.7 represent the shape of the beam calculated with the three-dimensional FEM model for increasing values of the electric current, while the solid lines are obtained with Equation (5.33) and the constitutive model of SMA wires. The temperatures used for the second approach are the wire temperatures in the middle of the beam ($x = L/2$) calculated with the FEM model.

These results lead to the following conclusion: to determine the shape of the SMA composite cantilever beam, it is sufficient to calculate the 2D temperature distribution in a cross-section of the beam, and apply Equation (5.33) and the constitutive model of SMA wires. This approach has the advantage that the temperature can be calculated with a higher accuracy, because significantly more 2D elements can be used over a cross-section, than is possible with the 3D mesh. More important, the computing time drops tremendously, because the

time consuming mechanical part of the FEM calculation is replaced by one non-linear equation, that can easily be solved, for example with a Newton-Raphson procedure. Especially when computing an open loop current for a large number of time steps, a huge reduction in computation time occurs. Therefore the 2D approach is used in the following.

5.3.4   Transient response

In this section the transient response of the beam is examined, i.e. the temperature distribution and shape change in time as a result of a prescribed current. Figure 5.8 shows a photograph of
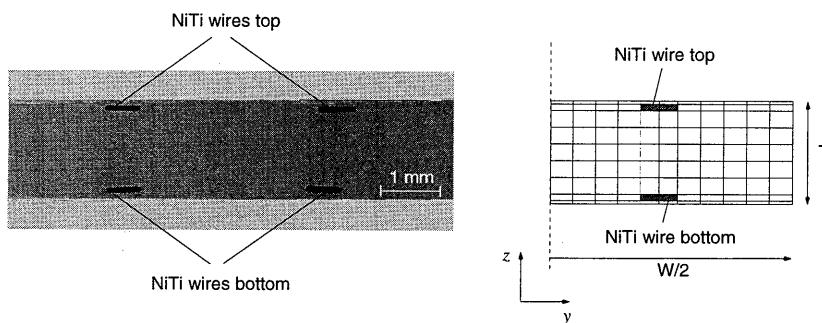
Figure 5.8: Left: photograph of cross-section of the cantilever beam. Right: FEM mesh
                 of half of the cross-section.

a cross-section of the beam, and the FEM mesh of one half of this cross-section. All elements are 8-node quadratic elements. The SMA wires consist of two elements each. During ten seconds an electric current of 0.7 A is supplied to the upper wires. After this period the current is supplied to the lower wires also during ten seconds. Figure 5.9 shows the temperature distribution in the cross-section of the strip at four consecutive moments. During the first ten seconds the temperature of the two upper wires rises very fast. The position of the wires is easily spotted by the two peaks. Because of the rather low conductivity of PP, large temperature gradients exist in the matrix material. After ten seconds no more heat is generated in the upper wires, causing their temperature to drop. At the same time the temperature of the lower wires increases, because of the supplied current. The lower two graphs of Figure 5.9 illustrate this process.

The temperature rise of the upper wires during the first ten seconds activates the shape memory effect. The stress in these wires increases with temperature and, because of the offset distance of the wires, a moment is generated, causing the beam to bend upwards. During the second stage the stress in the lower wires will exceed the stress in the upper wires. The result is an opposite bending of the beam. These findings are depicted in Figure 5.10. Current supplied to the top wires is positive, and it is negative for the bottom wires. The temperature and stress in the top and bottom wires are plotted against time (5.10b,c). Figure 5.10d shows the curvature of the beam.
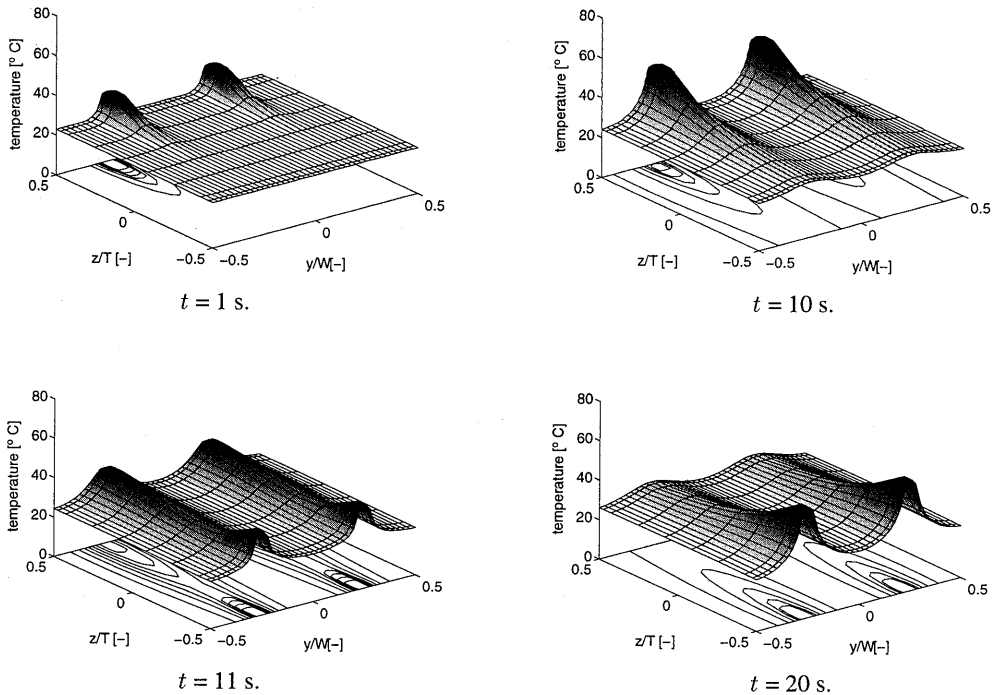
Figure 5.9: Temperature distribution in cross-section after 1 s, 10 s, 11 s, and 20 s.

5.4   Determination of open loop current

By controlling the electric current through the embedded SMA wires, it is possible to have the curvature of the beam follow a desired trajectory in time. The two control strategies that were applied for the systems in Chapters 3 and 4, being PI feedback control, and open loop plus PI feedback control, can also be used for SMA reinforced materials like the cantilever beam. Since a model of the SMA cantilever beam is available, an open loop current can be computed. Similar to the actuators in Chapters 3 and 4, the combination of two (parallel) SMA wires on top and two at the bottom is regarded as one actuator that is controlled by one input u. If u is positive, the upper wires are heated, a negative input implies heating of the bottom wires.

Suppose the curvature $\Psi(t)$ has to follow a desired trajectory $\Psi_d(t)$. To determine the desired or open loop input $u_{ol}(t)$, time is divided in increments $[t_{i-1}, t_i]$, $i = 1, \ldots, n_{inc}$. The desired curvature at $t = t_i$ is denoted by $\Psi_{d,i}$. The electric current that must be applied during increment i is determined with the inverse model of the SMA cantilever beam. It is very similar to the inverse models of the SMA actuators in Chapter 3, and the robotic finger in Chapter 4. However, for those systems, the temperature of the active and passive wires
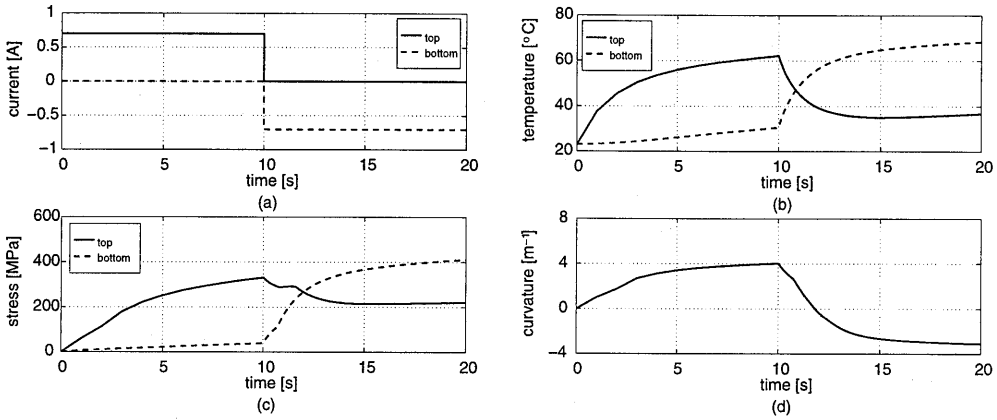
Figure 5.10: Calculated transient response of SMA composite beam: applied current (a), wire temperatures (b), wire stresses (c), and beam curvature (d)

were independent. When SMA wires are embedded in a host material, their temperatures are not independent. Determination of the open loop input must therefore be performed in an iterative way, and is done off-line.

The calculation of the open loop current in increment i is shown schematically below. The actuator output f is a bending moment, with $f = 2d\left(f_t - b\right)$.

System dynamics

$$f_{d,i} = DJ\Psi_{d,i}$$

Actuator dynamics

next iteration $j = j + 1$

$$u_j = u_{j-1} + \delta u_{j-1}$$

$$\{\tfrac{1}{\Delta t}\underline{C} + \underline{\Lambda}\}\underline{\vartheta}_j = \underline{R}_j(u_j) + \underline{Q}_j + \tfrac{1}{\Delta t}\underline{C}\underline{\vartheta}_{i-1}$$

$$\delta f_j = 2d\{f_{td}(\vartheta_{t,j}, \Psi_{d,i}) - f_{bd}(\vartheta_{b,j}, \Psi_{d,i})\} - f_{d,i}$$

$$\delta u_j = \left(\frac{\partial \delta f}{\partial u}\right)^{-1} \delta f_j$$

iterate until convergence

$$u_{ol,i} = u_j$$

The derivative $(\partial \delta f / \partial u)$ is approximated by

$$\frac{\partial \delta f}{\partial u} = \frac{f_{t,j-1} - f_{t,j-2} - f_{b,j-1} + f_{b,j-2}}{u_{j-1} - u_{j-2}} \qquad (5.34)$$

The iteration process is continued until the force residual δf is below a specified limit. Three iterations per increment are generally sufficient.

Figure 5.11 shows the result for two different desired curvatures. The increment time is 1/50 s. The two upper graphs (a,b) are the desired motions, the two lower graphs represent
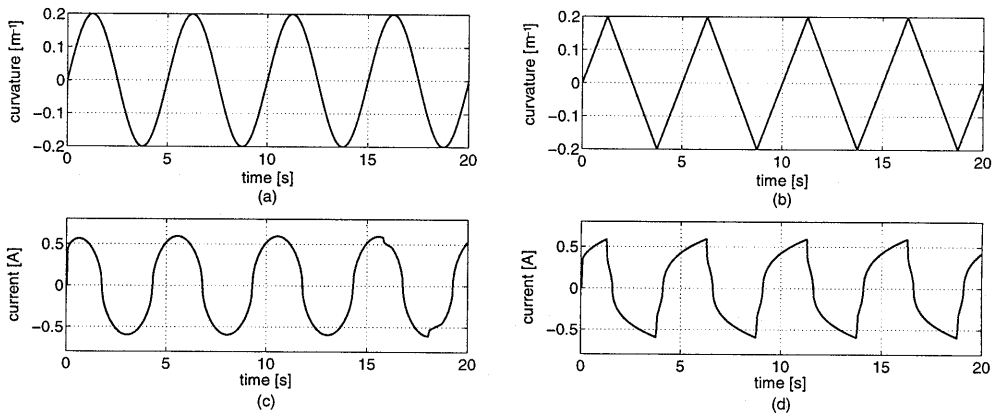
Figure 5.11: Two desired trajectories for the curvature (a,b), and the corresponding calculated open loop currents (c,d)

the corresponding currents (c,d).

5.5   SMA composite frame

For the cantilever beam only one curvature is of importance, but for structures like wings and antenna surfaces the shape must be controlled in two directions. Therefore a structure that extends in two directions was developed (see Figure 5.12). Essentially it is a frame consisting of four cantilever beams. Removal of the midsection is not necessary, but has the following advantages. First the bending stiffness of the matrix material is reduced drastically, yielding quite large deformations without the need for increasing the amount of SMA wires. Secondly, the temperature fields in the four beams only affect each other in the corners. When a massive plate with multiple SMA wires is considered, a full three-dimensional mesh is necessary to determine the temperature distribution in the plate. Even for a small plate the number of elements and required computation time increases tremendously. Since the temperature is not constant along the wires, the deformation of such a plate is complicated and might require a three-dimensional mesh for the mechanical part as well. Determination of open loop currents for the embedded wires becomes very difficult then, if not impossible.
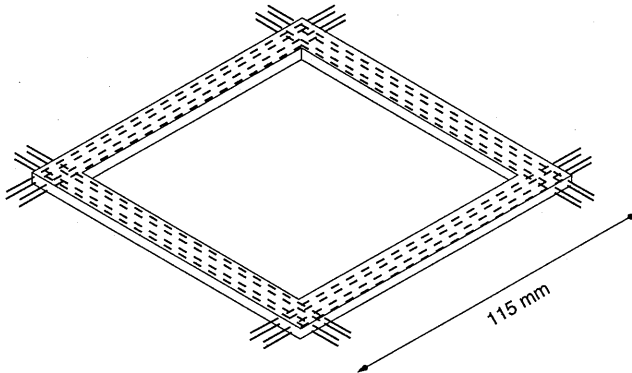
Figure 5.12: SMA composite frame

With appropriate boundary conditions, mechanical interaction can also be neglected. The frame is clamped in one corner. Under these conditions, the approach outlined in the previous sections can be applied for each beam, to calculate the open loop current for the respective wires.

5.5.1   Shape measurement

The shape of the frame is determined with an optical position measurement system. The system includes a CCD camera, that views the frame directly and indirectly through a mirror
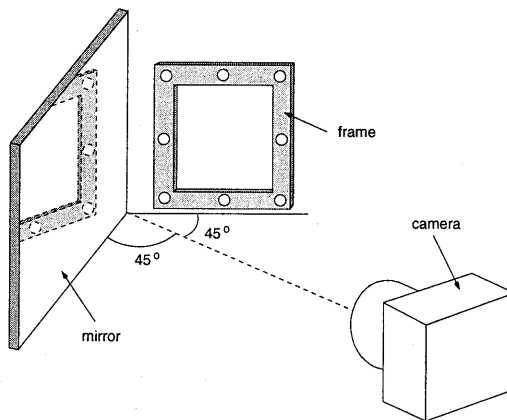
Figure 5.13: Camera setup

(see Figure 5.13), and an image processing part. Eight markers are attached to the frame at mutual distances of 52.5 mm along the edges. The SMA frame and its mirror image are

viewed by a CCD camera (Philips LDH 0701/10 1/2"). The image (512×512 pixels, see Figure 5.14a) is sent to a framegrabber (Data Translations). Each pixel has a gray scale value between 0 (white) and 255 (black). A marker is defined as a collection of pixels with gray scale values between 0 and 128. Before starting an experiment the entire image is scanned

(a)

(b)

(c)
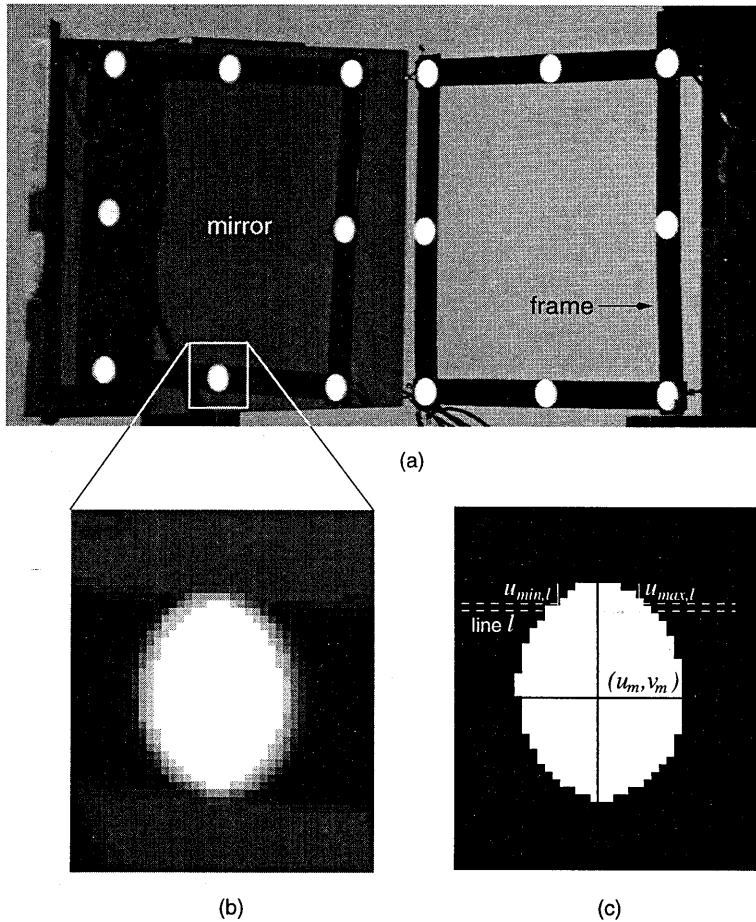
Figure 5.14: Frame and mirror image seen by the camera (a), scan window around a marker, showing the image pixels (b), digitized marker image after thresholding with calculated centre coordinates (c)

to trace all 16 markers. When they have been located, a search window is defined around each marker, see Figure 5.14a,b. The size of the windows depends on the expected maximum displacement of the markers in a time step. At each time step only the 16 windows are scanned to reduce processing time. Figure 5.14c shows a digitized image of a marker. The

position of the centre of marker image m, (u_m, v_m), is estimated by (see Peters, 1987)

$$u_m = \frac{\sum\limits_{l=v_{min}}^{v_{max}} \left(u_{max,l}^2 - u_{min,l}^2\right)}{2\sum\limits_{l=v_{min}}^{v_{max}} \left(u_{max,l} - u_{min,l}\right)} \quad ; \quad v_m = \frac{\sum\limits_{l=u_{min}}^{u_{max}} \left(v_{max,l}^2 - v_{min,l}^2\right)}{2\sum\limits_{l=u_{min}}^{u_{max}} \left(v_{max,l} - v_{min,l}\right)} \tag{5.35}$$

where $u_{min,l}$ and $u_{max,l}$ are the begin and end position of pixel line l, see Figure 5.14c. The other parameters have similar meanings.
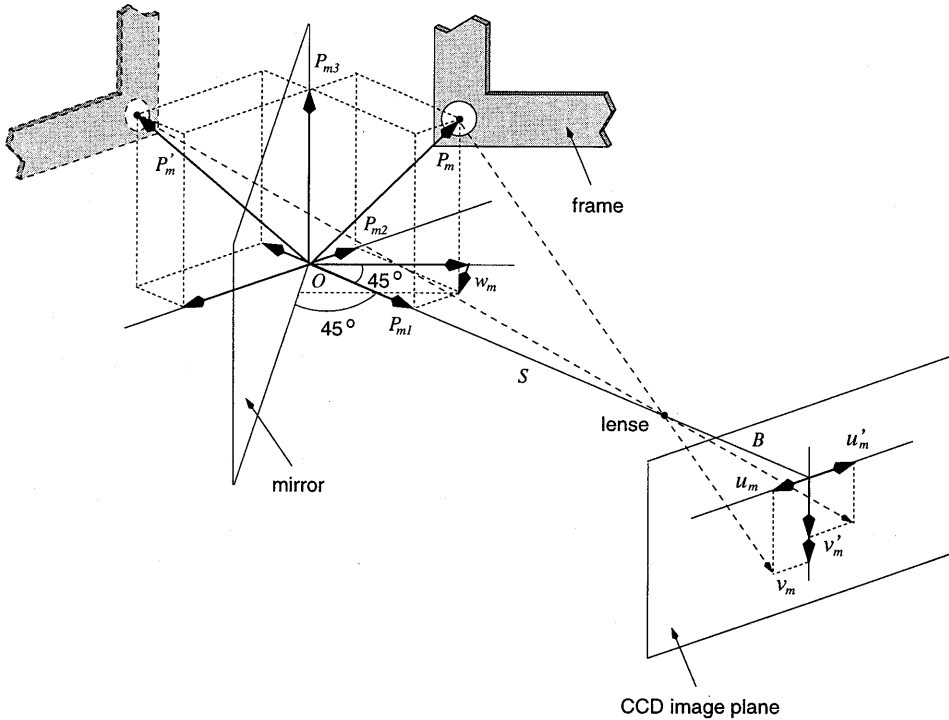
Figure 5.15: Camera - mirror setup

Each of the eight physical markers is described by four image coordinates (u_m, v_m, u'_m, v'_m), where $'$ refers to the mirrored image. The three-dimensional position $\underline{P}_m = \begin{bmatrix} P_{m1} & P_{m2} & P_{m3} \end{bmatrix}^T$ of marker m ($m = 1, \ldots, 8$), is related to the image coordinates by the following geometric

formulas (see Figure 5.15):

$$u_m = \frac{B P_{m2}}{S - P_{m1}} \quad ; \quad v_m = \frac{B P_{m3}}{S - P_{m1}}$$

$$u'_m = \frac{B P_{m1}}{S + P_{m2}} \quad ; \quad v'_m = \frac{B P_{m3}}{S + P_{m2}} \tag{5.36}$$

where $S = 1730$ mm is the distance between the camera lens and the origin O of the coordinate system, and $B = 50$ mm is the distance between the lens and the CCD plane. With these equations the unknown marker positions $\underset{\sim}{P}_m$ can be reconstructed. After some elaboration Equations (5.36) result in

$$\begin{bmatrix} u_m & B & 0 \\ v_m & 0 & B \\ B & -u'_m & 0 \\ 0 & -v'_m & B \end{bmatrix} \begin{bmatrix} P_{m1} \\ P_{m2} \\ P_{m3} \end{bmatrix} = \begin{bmatrix} u_m S \\ v_m S \\ u'_m S \\ v'_m S \end{bmatrix} \quad \text{or} \quad \underset{\sim}{A}\, \underset{\sim}{P}_m = \underset{\sim}{y} \tag{5.37}$$

This is a set of four equations for the three unknown components of $\underset{\sim}{P}_m$. The unweighted least squares solution is given by

$$\underset{\sim}{P}_m = (\underset{\sim}{A}^T \underset{\sim}{A})^{-1} \underset{\sim}{A}^T \underset{\sim}{y} \tag{5.38}$$

The position $\underset{\sim}{P}_m$ of all eight markers is determined this way. Since the frame is at an angle of $45°$ with respect to the optical axis of the camera, the out-of-plane displacement w_m of each marker is (see Figure 5.15):

$$w_m = \tfrac{1}{2}\sqrt{2}(P_{m1} - P_{m2}) \qquad m = 1, \dots, 8 \tag{5.39}$$

Because the beams that form the frame are loaded only by bending moments, the curvature of each beam is constant. The curvature of the four beams can be calculated from the out-of-plane displacements of the three markers on each of the beams. Defining the corner markers on a beam i as 1 and 3, and the centre marker as 2, with the markers located at mutual distances $L/2$, the curvature of the beam is

$$\Psi_i = \frac{4(w_{i1} - 2w_{i2} + w_{i3})}{L^2} \qquad i = 1, \dots, 4 \tag{5.40}$$

The distance between the corner markers L is 105 mm for all frame sides.

5.5.2   Accuracy

The obtained marker positions contain random errors. The standard deviation of the discretization error in the image plane coordinates u_m and v_m is (see Peters, 1987):

$$\sigma_u = \sqrt{\frac{S\, d_p^3}{22\, B\, d_m}} \tag{5.41}$$

where d_p is the width of a pixel at the CCD cell (11μm), and d_m is the diameter of a marker (7.0 mm). With these values the standard deviation of the discretization error in the image coordinates is 0.55μm. The effect of these errors on the 3D marker positions P_m follows from Equations (5.36). For large values of S/B (=34.6), the standard deviation for P_{m1}, P_{m2} is approximately $S/B\,\sigma_u$, while for P_{m3} it is $S/(\sqrt{2}B)\,\sigma_u$. For the present experimental setup these values become 19μm and 14μm. The standard deviation of the error in the value of the out-of-plane displacements w_m is also 19μm, using Equation (5.39), while for the curvatures it is $1.7 .10^{-4}$ m^{-1}, which is accurate enough for desired curvatures with amplitudes of 0.2 m^{-1}.

The discretization error gives an idea about the maximum accuracy that can be expected, when a perfect white marker on a black background is scanned. In practice additional effects influence the digitized marker image, like varying light intensity. Even when the light intensity is constant, charging of the CCD cells may vary. The result of these effects is that the gray scale value of the pixels forming the boundary of a marker may be above or below the threshold value. This process is quite random. The effect on the accuracy of the calculation of the marker centre is similar to the discretization effect. To verify this, a motionless marker image was scanned 50 times. The marker positions showed a standard deviation of 14.5 μm. This value is in good agreement with the theoretically derived value.

Table **5.10**: Desired curvatures

beam	curvature		
	sphere	cylinder	saddle
1	$\Psi_d(t)$	$\Psi_d(t)$	$\Psi_d(t)$
2	$\Psi_d(t)$	0	$-\Psi_d(t)$
3	$\Psi_d(t)$	$\Psi_d(t)$	$\Psi_d(t)$
4	$\Psi_d(t)$	0	$-\Psi_d(t)$

Table **5.11**: Control parameters

parameter	value	unit
K_p	20	A^2.m^{-1}
τ_i	140	A^2.m^{-1}.s^{-1}

5.6   Experimental results

The control objective was to have the curvature of the four beams $\Psi_i(t)$, $i = 1, \dots, 4$ follow a desired trajectory $\Psi_{d,i}(t)$, $i = 1, \dots, 4$. Three sets of curvatures, listed in Table 5.10, were chosen. When the frame is regarded as a 'plate with hole', these curvatures correspond with a spherical, cylindrical, and saddle shape of the plate. In the following these terms will be used for convenience. For the desired curvature Ψ_d as a function of time, a sinus and a sawtooth are chosen, both with an amplitude of 0.2 m^{-1}, and period times of 5 and 10 seconds. All shapes were controlled with three controller settings: open loop alone, feedback alone, and open loop plus feedback. The feedback controllers are independent of each other: the SMA

actuator in each beam is controlled by the tracking error of the curvature of the concerned beam. Since the thermal behaviour of the SMA cantilever beams cannot be modeled as a linear first order process with one time constant, but also spatial effects (conduction) are important, no attempts were undertaken to derive theoretical feedback controller parameters. The experimental values of the control gain and the integral time constant were equal for all beams during all experiments. They are listed in Table 5.11.

5.6.1   Open loop control

Ideally no feedback part would be necessary if the model used to determine the open loop currents is accurate enough, and initial conditions are equal to the desired initial conditions. In that case no measurement would be required, with the advantage of reduced weight, costs, and complexity. Therefore it was investigated if application of the open loop currents alone yields acceptable results. All desired frame shapes described above were tested. An example of the tracking results is shown in Figure 5.16, being the saddle shape, with sawtooth variation in time.

The tracking results are quite unacceptable. Although all beams move more or less in the desired way, the realized curvatures differ very much from the desired ones. Beams 2 and 4 respond in a symmetric way, but the amplitude is too small. Beams 1 and 3 tend to curve upwards. This may be caused by differences in the offset distance of the SMA wires on either side of the beams, by different initial strains or by deteriorated shape memory effect because of accumulated plastic deformation.

The conclusion is that shape control for an SMA reinforced material, based on open loop alone, is not applicable. It is hardly possible to predict the desired current accurately, and a feedback part is indispensable.
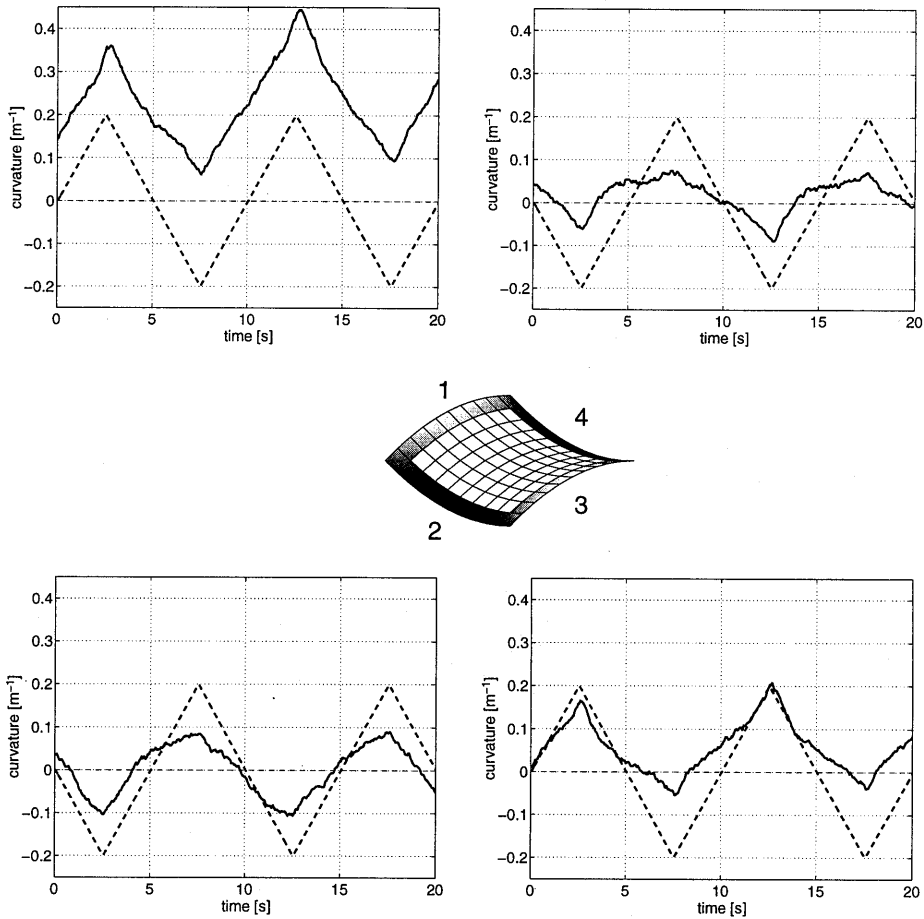
Figure 5.16: Open loop control of SMA reinforced frame, experimental results for saddle shape: desired curvatures (dashed), and realized curvatures (solid)

5.6.2   Closed loop control

In this section the feedback and the open loop plus feedback controller are compared. All desired shapes listed in Table 5.10 were applied. Figure 5.17 shows the tracking results for the saddle shape and sawtooth variation with a period time of 10 s, with the open loop plus feedback controller. In contrast with the open loop controller, the beams follow the desired curvatures rather well. Although the deviation between desired and realized curvature is at some moments as large as 20%, these errors are reduced quite fast. If the time period of the variation is increased, the errors become much smaller. It is surprising that, although
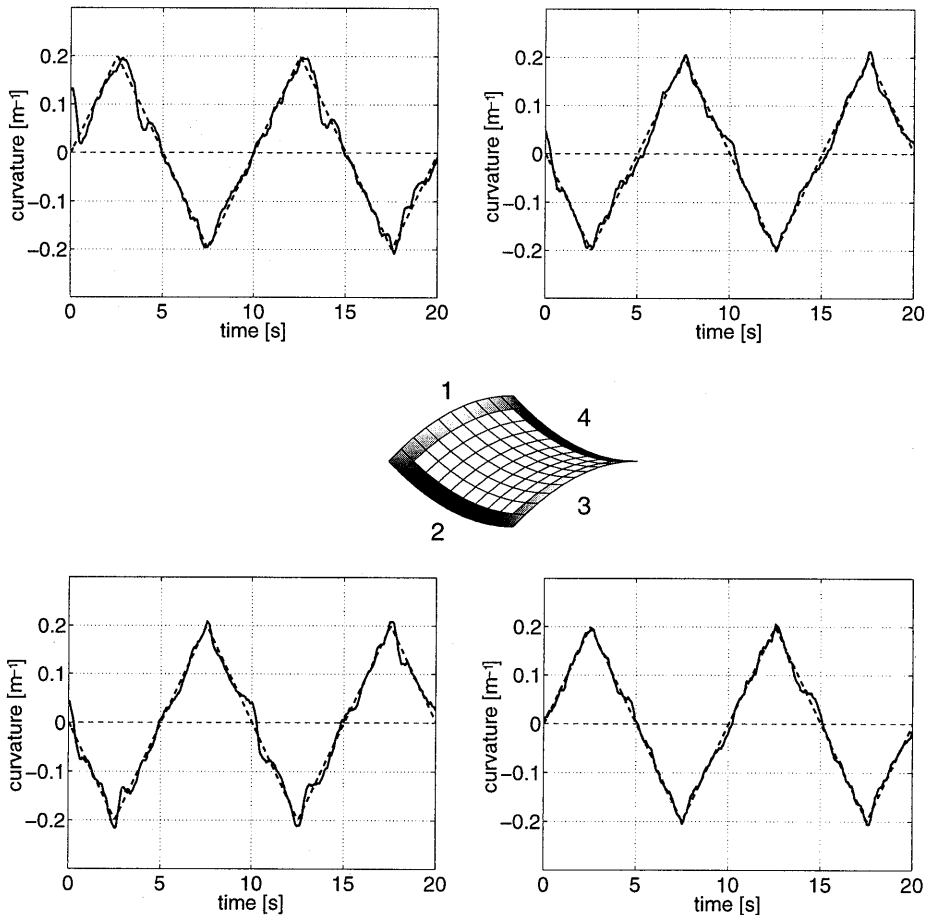
Figure 5.17: Shape control of SMA reinforced frame, experimental results for saddle shape: desired curvatures (dashed), and realized curvatures (solid)

the SMA wires are inside the host material, and heat must be transferred from the wires to that rather badly conducting matrix material, the bandwidth of the controlled system is in the same order as for the SMA actuators that are surrounded by air (Chapters 3 and 4). So the general opinion that embedding SMA actuators slows down severely their speed of operation, is not confirmed by these experiments. Figure 5.18 shows the electric currents corresponding
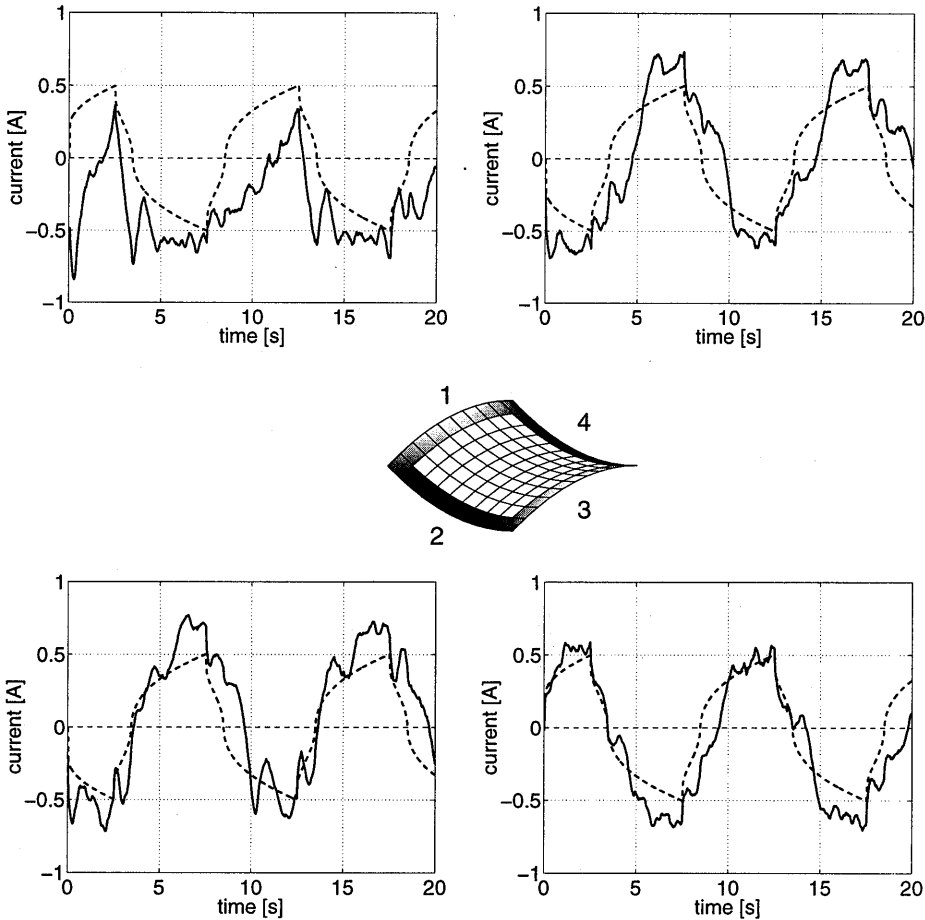
Figure 5.18: Shape control of SMA reinforced frame, experimental results for saddle shape: open loop currents (dashed), and realized currents (solid)

to the curvatures in Figure 5.17. It demonstrates that the magnitude of the open loop currents corresponds very well with the really supplied currents. The applied current in beam 1 is on average below zero, which is in accordance with the open loop response of beam 1, see Figure 5.16; apparently it takes more effort to bend beam 1 downwards, than to bend it

upwards.

The tracking results for all shapes are summarized in Figure 5.19. Each bar represents the RMS value of the tracking errors (averaged over the four beams) during the second cycle of a motion. The upper graph gives the results for a sinusoidal variation in time, the lower graph contains the RMS errors for a sawtooth. It is clear that for all experiments the open loop part improves the tracking accuracy of the beams. On average an improvement of a factor 1.5 to 2 holds. The RMS errors are lower for the cylinder shape, because two of the four beams have
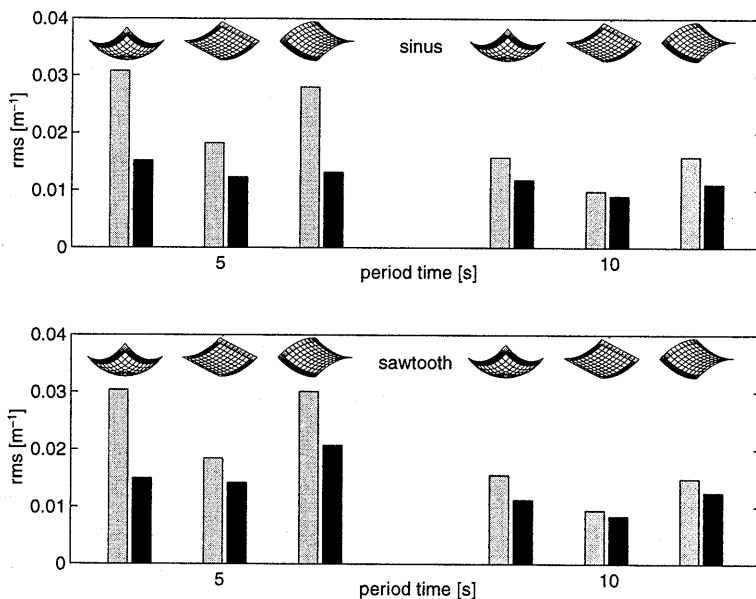
Figure 5.19: RMS values of the tracking error for various shapes, and sinus shaped variation (top), and sawtooth (bottom). The light bars represent feedback control, the dark bars open loop plus feedback

to remain straight, which is easier than moving up and down. The open loop term is zero for the two straight beams. No distinction can be found between the upper and lower graph.

5.7   Conclusions

Shape control of SMA reinforced structures was investigated in this chapter. A finite element model was developed to describe both the thermal and mechanical behaviour of a structure, that consists of SMA wires embedded in a host material. It was shown that large temperature

gradients exist in the cross-section of a cantilever beam. However, both temperature and wire stresses are almost constant along the length of the beam. These findings allow a drastic simplification of the three-dimensional model. Because of the heat conduction of the host material, the wire temperatures on either side of a beam are not independent. The open loop current must therefore be computed in an iterative way. Active shape control experiments were carried out on a frame consisting of four SMA reinforced beams. The control objective was to have the curvature of each beam track a desired path. Open loop control alone yields poor results. Feedback control is capable to perform the control task. Addition of the open loop term to the feedback controller yields the best results, improving tracking accuracy by a factor 1.5 to 2.

6   Conclusions and recommendations

Shape memory alloys have specific properties, that make them suitable as actuators. This thesis adresses the problems and possibilities associated with the motion and shape control of materials and structures using SMA actuators. Several mechanical structures have been developed, that contain attached or embedded SMA wires. The SMA wires are controlled by changing the supplied electric current. The control strategy consisted in all cases of a Proportional-Integral feedback (FB) control law. The usefulness of adding an open loop (OL) term to the controller has been examined. The open loop part is the predicted electric current, based on a model of the entire system, necessary to have the structure follow a desired motion. An essential part of the open loop part are the thermal dynamics and highly nonlinear constitutive behaviour of the SMA wires.

Simulation of structures containing SMA's requires a constitutive model of the thermomechanical behaviour of SMA's, relating stress, strain and temperature. An overview of existing 1D and 3D constitutive models is given. The models use almost exclusively the temperature as a known variable and either stress or strain as the unknown variable, since most numerical analyses aim at the determination of the deformation of a structure resulting from a temperature change in the SMA constituents. However, in this thesis a control method is proposed that requires an inverse constitutive model, having stress and strain as known variables, and temperature as the unknown variable. Since the available constitutive models were judged to be inappropriate, an alternative one-dimensional constitutive model was developed. It describes the main shape memory characteristics, being pseudoelasticity at elevated temperatures, (quasi) permanent deformation at lower temperatures, recovery of the initial shape upon heating and the existence of a hysteresis loop, and can be used both in the forward and the inverse way.

Heating an SMA wire results in motion in one direction. To enable motion in the opposite direction, the SMA wire must be loaded by an external force. This force can be provided by the mechanical system (gravity, elasticity), but generally an SMA actuator consists of an SMA wire and a second passive element, that stretches the SMA wire at lower temperatures. A general framework is presented on SMA actuators in mechanical systems, that serves as a basis for the systems described in Chapter 3, 4 and 5.

Control of SMA actuators implies changing the temperature of the SMA wires. This is usually achieved by resistive heating. The majority of control methods used in literature uses a Proportional- Integral-Derivative feedback control law or a variant. These approaches do not incorporate directly any knowledge about the system dynamics. However, tuning of the control parameters is aided with a (linearized) model of the controlled system. Since an SMA responds either elastically or by means of martensitic transformation, a linearized model of the shape memory behaviour was derived for both cases. Theoretical values for the control parameters have been derived for most mechanical systems in this thesis based on these linearized models. It was shown that a derivative action does not improve tracking performance, which was confirmed in all experiments. The behaviour during transformation is the limiting factor for the attainable control gain. The very low stiffness encountered during transformation results in a quite low resonance frequency, that is slightly damped. However, the tracking performance is worse during an elastic response, i.e. during crossing of the hysteresis, because the length of an SMA wire changes very little with temperature here. Summarizing, the achievable closed loop bandwidth is limited by both the transformation behaviour (control gain) and the elastic behaviour.

In the experiments often higher control gains could be applied then the theoretically derived values. This is probably due to the fact that the linearized transformation model uses the smallest possible stiffness, i.e. it is a 'worst case' model. In practice the material is generally stiffer, allowing a higher control gain. In some cases the theoretical and experimental values differ by a factor ten. It is therefore concluded that the linearized models are useful for understanding the problems associated with PID feedback control of SMA actuators, and that they give an indication about the magnitude of the control parameters. They are less suitable for the exact determination of the control parameters.

With a complete model of the mechanical structure including SMA actuators, it is possible to predict the electric current, that must be supplied to achieve a desired motion or shape. Adding this so-called open loop current to the feedback current may improve the performance of the controlled system. The derivation of the open loop current is explained in Chapter 2 in general and is specified for each system in the consecutive chapters. The first order heating dynamics and the chosen constitutive model result in sudden peaks in the electric current, which deteriorate the tracking performance enormously. Therefore the open loop current is adapted, such that the peaks disappear. This problem could also be avoided with a constitutive model, that describes the transition from elastic behaviour to transformation more smoothly. However, such model, that can be used inversely as well, does not exist at the moment.

Experiments with SMA actuators in several mechanical structures have been carried out. First, three translational systems with one-degree-of-freedom were analysed. The tensile force required to stretch the cooled SMA wire was provided by the weight of a mass, a helical spring (bias spring actuator), and a second SMA wire (differential actuator) respectively. In the differential actuator both wires can be activated. Tracking experiments with a number of test trajectories point out that adding an open loop term diminishes the tracking error in all cases. For the mass SMA system a decrease of the tracking error by a factor four in comparison with feedback control alone could be obtained. The effect was smaller for the

bias spring and the differential actuator, because in those cases a higher control gain could be applied, enhancing the effect of the feedback controller. The first order dynamics of the heating dynamics form an indispensable part of the open loop part. An open loop part based on steady state conditions has little effect. The open loop part is especially effective during crossing of the hysteresis, because the influence of the feedback controller is limited here. The overall performance of the bias spring actuator and the differential actuator was comparable. The advantage of the differential actuator is that the tensile forces in the SMA wires are smaller.

The differential actuator type was selected to actuate the joints of a robotic finger consisting of three links and two rotary joints. By controlling both joint angles, the finger tip can follow a desired trajectory. The two moving links were counterbalanced to avoid excessive loading of the SMA wires. The relatively large inertias of both links with respect to the stiffness of the SMA wires limit the attainable bandwidth severely. Therefore the finger tip was only able to follow quite slow motions: a circle could not be tracked faster than 100 s. Addition of an open loop term yielded better tracking performance for the joint angles. However, this did not automatically imply better tracking performance at the finger tip. The RMS value of the error in y-position of the finger tip even deteriorated. The open loop term diminished on average the joint angle tracking errors, but increased the angle tracking errors in the range where a small angle tracking error has a large effect on the y-position of the finger tip, resulting in an increase of the RMS value of the y-position tracking error.

The possibility to diminish the influence of externally applied loads at the finger tip was also investigated. Addition of an open loop term based on the (known) external disturbance load, resulted in a decrease of the position error of both angles. Especially joint 1 benefited from the open loop term, probably because the disturbance torque resulting from the tip load is higher for joint one than for joint two.

Active shape control of SMA reinforced materials was also investigated. A Finite Element Model was developed, that calculates the deformation and shape of SMA reinforced materials, when the SMA wires are heated electrically. The SMA wires were modeled as a series of one-dimensional trusses. The SMA behaviour was incorporated in the FE model using a subroutine that determines the stress and momentary stiffness, based on the martensite fraction, strain and temperature of the truss element. The shape change of a polypropylene cantilever beam containing four NiTi wires was computed. Both the axial stresses and temperatures in the SMA wires appeared to be almost constant along the length of the wires. This implies that the cantilever beam is loaded by a constant bending moment, and the deformation is described with a constant curvature. This fact allows for a simplification of the FE model. It suffices to calculate the temperature distribution in a cross-section of the cantilever beam and determine the curvature of the beam with a bending moment balance equation. The bending moments applied by the SMA wires depend on the curvature of the beam and on their temperature. This computationally much faster model was used for the calculation of open loop currents.

The structure used for active shape control experiments was a frame consisting of four cantilever beams. Two pairs of NiTi wires were embedded in each beam. By controlling

the electric currents through all four beams, the curvature of each beam could be changed actively. The curvatures of the four beams were measured by attaching markers to the structure, the position of which was measured by a camera and an image processing unit. The control task was to have the beam curvatures follow specified trajectories in time. Open loop currents were calculated for all beams. Application of the open loop currents alone revealed that feedback control and therefore a measurement system is indispensable. Two facts are responsible for the inability to obtain satisfactory tracking results by open loop control alone. First, the values of several parameters that influence the response of an SMA reinforced beam are difficult to determine or are not constant in time and space. Examples are the convective heat transfer coefficient, the thermal conductivity of the matrix material and the temperature of the surrounding medium. Errors are also made in the constitutive model of the SMA wires. Not only are the straight lines constructing the stress-strain-temperature envelope an approximation of the real behaviour, the constitutive parameters change during service as well due to, e.g., plastic deformation and a decrease of the transformation stresses. It is therefore very difficult to calculate the open loop current with a high accuracy. The second problem associated with open loop control is the narrow temperature region in which transformation occurs. The response of an SMA wire is very sensitive to small temperature variations during transformation. A small error in the calculation of the open loop current results in a slightly different temperature, but a large error in force or deformation. It is therefore concluded that open loop control alone is not a feasible method for active shape control.

The results presented give rise to recommendations for future research. The research in this thesis has focused on the application of SMA wires as actuators in different mechanical structures. Many questions are still unanswered. A more profound investigation of the problems encountered with each of the structures is certainly recommended. Especially control aspects deserve more attention. Two major problems were encountered using the open loop plus PI feedback control strategy. First, using PI feedback with constant parameters limits the attainable bandwidth due to the nonlinear constitutive behaviour. Second, the improvement in tracking accuracy achieved with the addition of an open loop term is less than expected. Alternative control methods might solve some of the problems. The SMA model is used in different ways then. Some suggestions are given here. The constant control parameters in the PI feedback controller can be replaced by non-constant parameters, that depend on the state (m, ξ, ϑ) of the SMA wires. The SMA model is used on-line to keep track of the state. This way it is possible to use different controller settings during transformation and elastic behaviour. This type of control is called *gain scheduling*. A *computed torque* control law cancels (ideally) the nonlinearities in the SMA behaviour by using the model *on-line*, i.e. *measured* quantities are used in the model as well, not only *desired* quantities. The compensation of nonlinearities implies that a large input results during (estimated) elastic behaviour, while a small input is calculated during transformation. In practice this may result in a large input during transformation, resulting in bad tracking performance and possibly causing instability. Addition of a *sliding mode* term in the control law improves the robustness against model errors. However, the chattering occuring with a usual sliding mode controller may excite the (slightly damped) resonance frequency, which should be avoided at all times.

To the author's expectation, *robust* controllers are very appropriate to control SMA actuators. The two linearized models, that were derived for all systems in this thesis, can be regarded as an upper bound (transformation), and a lower bound (elastic) for the constitutive behaviour. With these models an average model can be constructed with known error bounds. A robust controller can be designed then, that takes into account these model errors. Such controller can also be designed to be less active at the frequencies in the neighbourhood of the resonance frequency. Beyond the elastic resonance frequency it can be active again. Higher bandwidths can be achieved this way. This control approach is especially appropriate for structures with a very low resonance frequency like the robotic finger.

A subject that has not been adressed, is optimal control of SMA actuators. In this thesis, the actuators consisting of two SMA wires (differential actuators) are always controlled such that the electric current in one of the wires is always zero. It is also possible to heat *both* wires. In that case two inputs are available to control one degree of freedom. This redundancy can be exploited to optimize a variable, e.g. the response speed (by keeping both wires at an elevated temperature). Optimal control is also an issue for the robotic finger, when it consists of more then two links. The boundaries of the working range of SMA wires are given by $m = 0$ and $m = 1$. With more links available, the working range of each wire can be optimized by aiming at $m = 0.5$ for each wire.

The material used to manufacture an SMA reinforced composite was polypropylene, a thermoplastic. A limiting factor of thermoplastics is their melt temperature. The electric current through the SMA wires could not exceed 0.7 A for a longer time, because the material melted at higher currents. To avoid this drawback high T_g thermoplastics or thermosets should be used.

Measurement of the shape of SMA reinforced composites was performed with a digital camera and an image processing unit. A more practical alternative to measure the shape of a composite is offered by optical fibers (Michie, 1992). They are embedded in the composite and can measure strain, temperature etc. The incorporation of both actuators and sensors in a material is the next step towards a so-called smart material.

A   Robotic finger parameters

The dynamic parameters of the robotic finger are given here. They can be derived with Lagrange's method, see e.g. (Asada and Slotine, 1986).
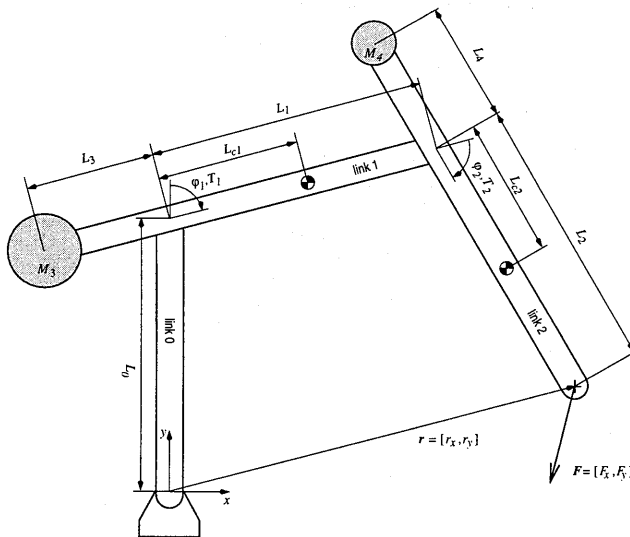
The equations of motion are written as

$$\underline{M}\ddot{\underline{q}} + \underline{B}(\dot{\underline{q}}) + \underline{g}(\underline{q}) = \underline{f} + \underline{w}$$

with

$$\underline{M} = \begin{bmatrix} M_{11} & M_{12} \\ M_{12} & M_{22} \end{bmatrix} \qquad ; \quad \underline{B} = \begin{bmatrix} b_1\dot{q}_1 - 2h\dot{q}_1\dot{q}_2 - h\dot{q}_2^2 \\ h\dot{q}_1^2 + b_2\dot{q}_2 \end{bmatrix}$$

$$\underline{g} = \begin{bmatrix} g_1 \\ g_2 \end{bmatrix} \qquad\qquad\qquad ; \quad \underline{f} = \begin{bmatrix} T_1 \\ T_2 \end{bmatrix}$$

The dynamic parameters are

$$
\begin{aligned}
M_{11} &= J_1 + J_2 + J_3 + J_4 + M_1 L_{c1}^2 + M_2(L_1^2 + L_{c2}^2 + 2L_1 L_{c2} c_2) + \\
&\quad + M_3 L_3^2 + M_4(L_1^2 + L_4^2 - 2L_1 L_4 c_2) \\
M_{12} &= J_2 + J_4 + M_2(L_{c2}^2 + L_1 L_{c2} c_2) + M_4(L_4^2 - L_1 L_4 c_2) \\
M_{22} &= J_2 + J_4 + M_2 L_{c2}^2 + M_4 L_4^2 \\
h &= M_2 L_1 L_{c2} s_2 - M_4 L_1 L_4 s_2 \\
g_1 &= -g s_1(M_1 L_{c1} + M_2 L_1 - M_3 L_3 + M_4 L_1) - g s_{12}(M_2 L_{c2} - M_4 L_4) \\
g_2 &= -g s_{12}(M_2 L_{c2} - M_4 L_4)
\end{aligned}
$$

where J_1 and J_2 are the inertias of link 1 and 2 with respect to their centre of gravity, and J_3 and J_4 are the inertias of the counterbalance masses 3 and 4. The distance of joint 1 and 2 to the centre of gravity of link 1 and 2, respectively, is L_{c1} and L_{c2}.

References

Abeyaratne R., S.-J. Kim and J.K. Knowles. A one-dimensional continuum model for shape-memory alloys. *Int. J. Solids and Struct.*, **31**(16):2229–2249, 1994.

Agrawal S.K., D. Tong and K. Nagaraja. Modeling and shape control of piezoelectric actuator embedded elastic plates. *J. of Intell. Mater. Syst. and Struct.*, **5**:514–521, July 1994.

Arai K., S. Aramaki and K. Yanagisawa. Feedback linearization for SMA (shape memory alloy). In *Proc. 34th SICE Annual Conf., July 26-28 1995, Hoikkaido Japan*, pages 1383–1386, SICE, Tokyo Japan, 1995.

Arai K., S. Aramaki and K. Yanagisawa. Continuous system modeling of shape memory alloy (SMA) for control analysis. In *Proc. 1994 IEEE 5th Int. Symp. on Micro Machine and Human Science, Oct 2-4 1994, Nagoya Japan*, pages 97–99, IEEE service center, Piscataway USA, 1994.

Aramaki S., S. Kaneko, K. Arai, Y. Takahashi, H. Adachi and K. Yanagisawa. Tube type micro manipulator using shape memory alloy (SMA). In *Proc. 1995 IEEE 6th Int. Symp. on Micro Machine and Human Science, Japan*, pages 115–120, IEEE, 1995.

Asada H. and J.-J.E. Slotine. *Robot analysis and control*. John Wiley & Sons, Inc., New York USA, 1986.

Ashley S. Getting a microgrip in the operating room. *Materials engineering*, **118**(9):91–93, September 1996.

Atluri S.N. On constitutive relations at finite strain: hypo-elasticity and elasto-plasticity with isotropic or kinematic hardening. *Comp. Meth. in Appl. Mech. and Eng.*, **43**:137–171, 1984.

Austin F., M.J. Rossi, W. van Nostrand and G. Knowles. Static shape control for adaptive wings. *AIAA Journal*, **32**(9):1895–1901, September 1994.

Barrett R. Active plate and wing research using EDAP elements. *Smart Mater. Struct.*, **1**:214–226, 1992.

Bathe K.-J. *Finite element procedures in engineering analysis*. Prentice-Hall, Inc., Englewood Cliffs, New Jersey USA, 1982.

Baz, A., K. Imam and J. McCoy. Active vibration control of flexible beams using shape memory actuators. *J. of Sound and Vibration*, **140**(3):437–456, 1990.

Baz A. and T. Chen. Torsional stiffness of Nitinol-reinforced composite drive shafts. *Composites Engineering*, **3**(12):1119–1130, 1993.

Baz A., S. Poh, J. Ro and J. Gilheany. Control of the natural frequencies of Nitinol-reinforced composite beams. *J. of Sound and Vibration*, **185**(1):171–185, 1995.

Baz A. and J. Ro. Optimal vibration control of Nitinol-reinforced composites. *Composites Engineering*, **4**(6):567–576, 1994.

Beauchamp C.H., R.H. Nadolink, S.C. Dickinson and L.M. Dean. Shape memory alloy adjustable camber SMAAC control surfaces. In *First European conference on smart structures and materials, 12-14 May 1992, Glasgow*, Culshaw B., editor, pages 189–192, Inst. of Physics Publ., 1992.

Besselink P.A. and R.C.L. Sachdeva. Applications of shape memory effects. *Journal de Physique IV, Coll. 8*, **5**:111–116, December 1995.

Bideaux J.-E., N. Bernet, C. Sarwa, J.-A.E. Månson and R. Gotthardt. Vibration frequency control of a polymer beam using embedded shape-memory-alloy fibres. *Journal de Physique IV, Coll. 8*, **5**:1177–1182, December 1995.

Bideaux J.-E., W.J. Yu, R. Gotthardt and J.-A.E. Månson. Modelling of the martensitic transformation in shape memory alloy composites. *Journal de Physique IV, Coll. 2*, **5**:543–548, February 1995.

Bondaryev E.N. and C.M. Wayman. Some stress-strain-temperature relationships for shape memory alloys. *Metall. Trans. A*, **19A**:2407–2413, October 1988.

Boyd J.G. and D.C. Lagoudas. Thermomechanical response of shape memory composites. *J. of Intell. Mater. Syst. and Struct.*, **5**:333–346, May 1994.

Brinson L.C. One-dimensional constitutive behavior of shape memory alloys: thermomechanical derivation with non-constant material functions and redefined martensite internal variable. *J. of Intell. Mater. Syst. and Struct.*, **4**:229–242, April 1993.

Brinson L.C., M.S. Huang, C. Boller and W. Brand. Analysis of controlled beam deflections using SMA wires. *J. of Intell. Mater. Syst. and Struct.*, **8**:12–25, January 1997.

Brinson L.C. and R. Lammering. Finite element analysis of the behavior of shape memory alloys and their applications. *Int. J. Solids and Struct.*, **30**(23):3261–3280, 1993.

Burdisso R.A. and R.T. Haftka. Optimal location of actuators for correcting distortions in large truss structures. *AIAA Journal*, **27**(10):1406–1411, October 1989.

Chadwick P. *Continuum mechanics: concise theory and problems*. Allen and Unwin, London UK, 1976.

Chandra R. and I. Chopra. Structural modeling of composite beams with induced-strain actuators. *AIAA Journal*, **31**(9):1692–1701, September 1993.

Chaudhry Z. and C.A. Rogers. Bending and shape control of beams using SMA actuators. *J. of Intell. Mater. Syst. and Struct.*, **2**:581–602, October 1991.

Chaudhry Z. and C.A. Rogers. Response of composite beams to an internal actuator force. *J. of Mechanical Design*, **114**:343–348, September 1992.

Chaudhry Z. and C.A. Rogers. Enhanced induced strain actuator authority through discrete attachment to structural elements. *AIAA Journal*, **31**(7):1287–1292, July 1993.

Chen P. and I. Chopra. Hover testing of smart rotor with induced-strain actuation of blade twist. *AIAA Journal*, **35**(1):6–16, January 1997.

Choi S.-B. and C.-C. Cheong. Vibration control of a flexible beam using shape memory alloy actuators. *J. Guidance, Control, and Dynamics*, **19**(5):1178–1180, 1996.

Donthireddy P. and K. Chandrashekhara. Modeling and shape control of composite beams with embedded piezoelectric actuators. *Computers & Structures*, **35**:237–244, 1996.

Duerig, T.W., K.N. Melton, D. Stöckel and C.M. Wayman, editors. *Engineering aspects of shape memory alloys*, Butterworth-Heinemann, London Great Britain, 1989.

Falk F. Model free energy, mechanics, and thermodynamics of shape memory alloys. *Acta metall.*, **28**:1773–1780, 1980.

Fu S., Y. Huo and I. Müller. Thermodynamics of pseudoelasticity - an analytical approach. *Acta metall.*, **99**:1–19, 1993.

Funakubo H. *Shape memory alloys*. Gordon and Breach science publishers, New York USA, 1987.

Furuya Y. and H. Shimada. Shape memory actuators for robotic applications, In *Engineering aspects of shape memory alloys*, Duerig, T.W., K.N. Melton, D. Stöckel, C.M. Wayman, editors, pages 338–355, Butterworth-Heinemann, London Great Britain, 1989.

Ghosh K. and R.C. Batra. Shape control of plates using piezoceramic elements. *AIAA Journal*, **33**(7):1354–1357, July 1995.

Gorbet R.B. and R.A. Russell. A novel differential shape memory alloy actuator for position control. *Robotica*, **13**:423–430, 1995.

Gorbet R.B. and D.W.L. Wang. General stability criteria for a shape memory alloy position control system. In *Proc. IEEE 1995 Int. conf. on robotics and automation, Nagoya Japan*, pages 2313–2319, IEEE, Piscataway USA, 1995.

Graesser E.J. and F.A. Cozarelli. A proposed three-dimensional constitutive model for shape memory alloys. *J. of Intell. Mater. Syst. and Struct.*, **5**:78–89, January 1994.

Grant D. and V. Hayward. Design of shape memory alloy actuator with high strain and variable structure control. In *Proc. IEEE 1995 Int. conf. on robotics and automation, Nagoya Japan*, pages 2305–2312, IEEE, Piscataway USA, 1995.

Harrison J.D. *Measurable changes concomitant with the shape memory effect*, In *Engineering aspects of shape memory alloys*, Duerig, T.W., K.N. Melton, D. Stöckel, C.M. Wayman, editors, pages 106–111, Butterworth-Heinemann, London Great Britain, 1989.

Hebda D.A., M.E. Whitlock, J.B. Ditman and S.R. White. Manufacturing of adaptive graphite/epoxy structures with embedded Nitinol wires. *J. of Intell. Mater. Syst. and Struct.*, **6**:220–228, March 1995.

Honma D., Y. Miwa and N. Iguchi. Application of shape memory effect to digital control actuator. *Bulletin of JSME*, **27**(230):1737–1742, August 1984.

Ikegami R., D.G. Wilson, J.R. Anderson and G.J. Julien. Active vibration control using Nitinol and piezoelectric ceramics. *J. of Intell. Mater. Syst. and Struct.*, **1**:189–206, April 1990.

Ikuta K. Micro/miniature shape memory alloy actuator. In *Proc. 1990 IEEE Int. conf. on robotics and automation, May 13-18 1990, Cincinnati USA*, pages 2156–2161, IEEE, Piscataway USA, 1990.

Ivshin Y. and T.J. Pence. A thermomechanical model for a one variant shape memory material. *J. of Intell. Mater. Syst. and Struct.*, 5:455–473, July 1994.

Jost, E. and E. Hornbogen. *The martensitic transformation in science and technology*, DGM Informationsgesellschaft, Oberursel Germany, 1989.

Jost N., K. Escher, K. Halter and E. Hornbogen. Modell eines Roboters aus Formgedächtnismetall. *Forschung im Ingenieurwesen - Engineering Research*, 58(3):46–49, 1992.

Kobayashi J., K. Yamauchi, I. Miyashita, ohkata, S. Narumi and Y. Suzuki. Recent activities of association of shape memory alloys (ASMA) in Japan. *Journal de Physique IV, Coll. 8*, 5:1159–1163, December 1995.

Koconis D.B., L.P. Kollár and G.S. Springer. Shape control of composite plates and shells with embedded actuators. I. Voltages specified. *J. of Comp. Mat.*, 28(5):415–458, 1994.

Koconis D.B., L.P. Kollár and G.S. Springer. Shape control of composite plates and shells with embedded actuators. II. Desired shape specified. *J. of Comp. Mat.*, 28(3):262–285, 1994.

Kohl M., K.D. Skrobanek, E. Quandt, P. Schloßmacher, A. Schüßler and D.M. Allen. Development of microactuators based on the shape memory effect. *J. Physique IV, Coll. 8*, 5:1187–1192, December 1995.

Kreith F. and M.S. Bohn. *Principles of heat transfer*. Harper & Row Publishers, Inc., 1986.

KrishnaKumar K. and L. Montgomery. Adaptive neuro-control for large flexible structures. *Smart Mater. Struct.*, 1:312–323, 1992.

Kuribayashi K. Millimeter-sized joint actuator using a shape memory alloy. *Sensors and Actuators*, 20:57–64, 1989.

Kuribayashi K. A new servo motor using shape memory alloy. In *15th Ann. Conf. of IEEE Industr. Electr. Soc., Nov 6-10 1989, Philadelphia USA, Part 1*, pages 238–243, 1989.

Kuribayashi K. Improvement of the response of an SMA actuator using a temperature sensor. *Int. J. of Robotics Research*, 10(1):13–20, February 1991.

Lagoudas D.C., J.G. Boyd and Z. Bo. Micromechanics of active composites with SMA fibers. *J. Eng. Mat. and Techn.*, 116:337–347, July 1994.

Lagoudas D.C. and I.G. Tadjbakhsh. Active flexible rods with embedded SMA fibers. *Smart Mater. Struct.*, 1:162–167, 1992.

Lammering R. Optimal placement of piezoelectric actuators in adaptive truss structures. In *First European conference on smart structures and materials, 12-14 May 1992, Glasgow*, Culshaw, B., pages 317–320, Inst. of Physics Publ., 1992.

Lashlee R., R. Butler, V. Rao and F. Kern. Robust control of flexible structures using multiple shape memory alloy actuators. *J. of Intell. Mater. Syst. and Struct.*, 5:702–712, September 1994.

Lashlee R., R. Damle, V. Rao and F. Kern. Identification and robust control of flexible structures using shape memory actuators. In *Proc. SPIE, Vol. 1919, Smart structures and materials 1993, Bellingham USA*, pages 271–282, 1993.

Liang C. and C.A. Rogers. One-dimensional thermomechanical constitutive relations for shape memory materials. *J. of Intell. Mater. Syst. and Struct.*, 1:207–234, April 1990.

Liang C. and C.A. Rogers. A multi-dimensional constitutive model for shape memory alloys. *J. Eng. Math.*, 26:429–443, 1992.

Lipscomb I.P. and L.D.M. Nokes. *The application of shape memory alloys in medicine*. Mechanical Engineering Publications, Ltd., Bury St. Edmonds UK, 1996.

Lu L.-Y., S. Utku and B.K. Wada. On the placement of active members in adaptive truss structures for vibration control. *Smart Mater. Struct.*, 1:8–23, 1992.

Maclean B.J., J.L. Draper and M.S. Misra. Development of a Shape Memory material actuator for adaptive truss applications. *J. of Intell. Mater. Syst. and Struct.*, 2:261–280, July 1991.

Madill D.R. and D. Wang. The modelling and L_2-stability of a shape memory alloy position control system. In *Proc. IEEE 1994 Int. Conf. on Robotics and Automation, San Diego USA*, pages 293–299, IEEE, Piscataway USA, 1994.

Martins de Carvalho J.L. *Dynamical systems and automatic control*. Prentice Hall, New York USA, 1993.

MARC manual. MARC Analysis Research Corporation, Palo Alto USA, 1994.

Matlab, version 4.2c . The Mathworks, Inc., 1994.

Michie W.C., B. Culshaw and D. Uttamchandani. Optical fibre techniques for structural monitoring in composites. In *Proc. of Smart Structures for Aircraft and Spacecraft, Oct 5-7 1992, Lindau Germany*, pages 8/1–8/9, AGARD, 1992.

Müller I. Description and simulation of shape memory. In *Martensitic transformation and shape memory properties, Proc. of European Symp., September 16-18 1991*, Guenin G., editor, Journal de Physique IV, Coll. 4, 1:47–60, 1991.

Müller I. and H. Xu. On the pseudo-elastic hysteresis. *Acta metall. mater.*, 39(3):263–271, 1991.

Nakazato Y., T. Kato and T. Masuda. Control of push-pull-type shape memory alloy actuator by fuzzy reasoning. *Trans. Japan Soc. Mech. Eng., Part C*, 59(568):3830–3836, December 1993.

Nakazato Y., T. Kato and T. Masuda. Position control of SMA actuator by fuzzy reasoning. *Trans. Japan Soc. Mech. Eng., Part C*, 59(565):2733–2738, September 1993.

Paine J.S.N. and C.A. Rogers. The response of SMA hybrid composite materials to low velocity impact. *J. of Intell. Mater. Syst. and Struct.*, 5:530–535, July 1994.

Paine J.S.N. and C.A. Rogers. Adaptive composite materials with shape memory alloy actuators for cylinders and pressure vessels. *J. of Intell. Mater. Syst. and Struct.*, 6:210–219, March 1995.

Paradies R., M. Hertwig and W.J. Elspass. Shape control of an adaptive mirror at different angles of inclination. *J. of Intell. Mater. Syst. and Struct.*, 7:203–210, March 1996.

Perkins, J. *Shape memory effects in alloys*, Plenum Press, New York USA, 1975.

Peters G. *Tools for the measurement of stress and strain fields in soft tissue*. PhD thesis, Eindhoven University of Technology, Netherlands, 1987.

Poulek V. Testing the new solar tracker with shape memory alloy actors. In *Proc. 1994 IEEE First world conf. on photovoltaic energy conversion, Dec 5-9 1994, Hawaii USA*, pages 1131–1133, IEEE, Piscataway USA, 1994.

Reynaerts D. *Control methods and actuation technology for whole-hand dexterous manipulation*. PhD thesis, Catholic University of Leuven, Belgium, 1995.

Reynaerts D. and H. van Brussel. Development of a SMA high performance robotic actuator. In *Proc. IEEE MEMS '91, Jan 30-Feb 2, Nara Japan*, pages 61–66, 1991.

Reynaerts D. and H. van Brussel. A SMA high performance actuator for robot hands. *Journal de Physique IV, Coll. 4*, **1**:157–162, November 1991.

Rhee S.-W. *Robust control of smart structures*. PhD thesis, University of Missouri, USA, 1992.

Rhee S.W. and L.R. Koval. Comparison of classical with robust control for SMA smart structures. *Smart Mater. Struct.*, **2**:162–171, 1993.

Ro J. and A. Baz. Nitinol-reinforced plates: part I. Thermal characteristics. *Composites Engineering*, **5**(1):61–75, 1995.

Ro J. and A. Baz. Nitinol-reinforced plates: part II. Static and buckling characteristics. *Composites Engineering*, **5**(1):77–90, 1995.

Ro J. and A. Baz. Nitinol-reinforced plates: part III. Dynamic characteristics. *Composites Engineering*, **5**(1):91–106, 1995.

Rogers, C.A., D.K. Barker and C.A. Jaeger. Introduction to smart materials and structures. In *Smart materials, structures, and mathematical issues, Sep. 15-16 1988, Blacksburg USA*, Rogers C.A., editor, pages 17–28, Technomic, Lancaster USA, 1988.

Rogers C.A., C.R. Fuller and C. Liang. Active control of sound radiation from panels using embedded shape memory alloy fibers. *J. of Sound and Vibration*, **136**(1):164–170, 1990.

Rogers C.A., C. Liang and J. Jia. Structural modification of simply-supported laminated plates using embedded shape memory alloy fibers. *Computers & Structures*, **38**(5/6):569–580, 1991.

Ropponen T. *Actuation redundancy in a closed-chain robot mechanism*. PhD thesis, Helsinki University of Technology, Finland, 1993.

Russell R.A. A robotic system for performing sub-millimetre grasping and manipulation tasks. *Rob. and Auton. Syst.*, **13**:209–218, 1994.

Saravanos D.A., V. Birman and D.A. Hopkins. Micromechanics and stress analysis of composites with shape memory alloy fibers in uniform thermal fields. In *AIAA/ASME/ASCE/AHS Structures, Structural Dynamics and Materials Conf.*, **1**:433–443, AIAA, New York USA, 1995.

Saunders W.R., H.H. Robertshaw and C.A. Rogers. Structural acoustic control of a shape memory alloy composite beam. *J. of Intell. Mater. Syst. and Struct.*, **2**:508–527, October 1991.

Shahin A.R., P.H. Meckl and J.D. Jones. Modeling of SMA tendons for active control of structures. *J. of Intell. Mater. Syst. and Struct.*, **8**:51–70, January 1997.

Slotine J.-J.E. and W. Li. *Applied nonlinear control*. Prentice-Hall International, Inc., Englewood Cliffs, New Jersey USA, 1991.

Spies R.D. An algorithm for simulating the isothermal hysteresis in the stress-strain laws of shape memory alloys. *J. Mat. Sci.*, **31**:6631–6636, 1996.

Stevens T. Structures get smart. *Materials engineering*:18–20, October 1991.

Stöckel, D.   Shape memory actuators for automotive applications. *Materials & Design*, **11**(6):302–307, December 1990.

Sullivan B.J.   Analysis of properties of fiber composites with shape memory alloy constituents. *J. of Intell. Mater. Syst. and Struct.*, **5**:825–832, November 1994.

Sun Q.P. and K.C. Hwang. Micromechanics modelling for the constitutive behavior of polycrystalline shape memory alloys - I. Derivation of general relations. *J. Mech. Phys. Solids*, **41**(1):1–17, 1993.

Sun Q.P. and K.C. Hwang. Micromechanics modelling for the constitutive behavior of polycrystalline shape memory alloys - II. Study of the individual phenomena. *J. Mech. Phys. Solids*, **41**(1):19–33, 1993.

Tanaka K. A phenomenological description on thermomechanical behavior of shape memory alloys. *J. Pressure Vessel Technology*, **112**:158–163, 1990.

Tanaka K., S. Kobayashi and Y. Sato. Thermomechanics of transformation pseudoelasticity and shape memory effect in alloys. *Int. J. Plasticity*, **2**:59–72, 1986.

Tanaka K., F. Nishimura, T. Hayashi, H. Tobushi and C. Lexcellent. Phenomenological analysis on subloops and cyclic behavior in shape memory alloys under mechanical and/or thermal loads. *Mech. of Mat.*, **19**:281–292, 1995.

Tanaka K., F. Nishimura and H. Tobushi. Phenomenological analysis on subloops in shape memory alloys due to incomplete transformations. *J. of Intell. Mater. Syst. and Struct.*, **5**:487–493, July 1994.

Documentation on TCE modules. WFW Report 94.050, Eindhoven University of Technology, Eindhoven Netherlands, 1994.

Trochu F. and Y.-Y. Qian. Nonlinear finite element simulation of superelastic shape memory alloy parts. *Computers & Structures*, **62**(5):799–810, 1997.

Wijst M., Van der and P. Schreurs. The numerical modelling of a smart structure in a control algorithm. In *Proc. ECCM-7 Smart Composites Workshop, Sept. 21-22 1993, Bordeaux France*, 1993.

Wada B.K., J.L. Fanson and E.F. Crawley. Adaptive structures. *J. of Intell. Mater. Syst. and Struct.*, **1**:157–174, April 1990.

Wayman, C.M. Some applications of shape-memory alloys. *J. of Metals*, pages 129–137, 1980.

Yoshida K. and Y. Umetani. Cosmo-lab concept: a cooperation of space robots and structures. In *Proc. Fifth Int. Conf. on Adaptive Structures*, pages 59–76, 1994.

Zienkiewicz O. and R. Taylor. *The finite element method, fourth edition.* McGraw-Hill Book Company, London UK, 1989.

Summary

In recent years much attention is focused on the development of adaptive or smart materials, whose mechanical behaviour can be changed during service to meet certain functional or structural requirements. To control actively the properties of such materials, actuators must become an integral part of them.

Among others Shape Memory Alloys (SMA's) form an important class of such built-in actuators. One of the best studied and most used SMA's is a nickel-titanium (NiTi) alloy. By raising the temperature of an unconstrained, previously deformed NiTi wire, its length can be reduced. Strains of about 8% can be recovered. If the wire is clamped at both ends during heating, a high stress develops (up to 800 MPa), and a large force can be exerted. This behaviour is due to a change of the micro structure, more specifically a phase transformation.

In the research presented here NiTi wires have been applied as actuators in several mechanical systems. The driving variable that has to be controlled is the temperature. Electric current is used for heating. The magnitude of the electric current is prescribed by a control law. Two control strategies have been chosen for all systems. First, a PI controller has been applied. In that case the electric current depends on the difference between the desired and realised value of certain variables. Second, an open loop term has been added, representing the current, that is necessary to achieve the desired goal. It is calculated with a model of the entire system. An important part of this model is the constitutive behaviour of NiTi wires, that describes the non-linear relation between stress, strain and temperature. A constitutive model has been developed, that enables calculation of each of the three constitutive variables when the other two are known. Therefore the model is very useful to determine the open loop current, because both stress and temperature can be the unknown variable. The open loop model also consists of the heating and cooling behaviour of the total system and the mechanical and thermal interaction between wires and surroundings.

First, attention was focused on three systems with one degree of freedom: a mass suspended by a NiTi wire, a spring and a wire in series and two serially connected NiTi wires. In the first two cases the NiTi wire shrinks during heating, thereby lifting the mass and stretching the spring, respectively. In the third system the heated wire shrinks and stretches the other

wire. This principle was subsequently applied to a robotic finger with two rotational degrees of freedom, that are each controlled by two shape memory wires. By heating the two pairs of wires properly the finger tip can follow a desired path.

Finally a beam has been made, consisting of a polypropylene matrix with NiTi wires embedded at the upper and lower side. Heating a wire on one side results in an increasing stress in the wire. Since the wires are positioned off-axis, the beam bends. An important difference with the former systems is the fact that the temperature of the wires on both sides are coupled due to the heat conduction in the matrix material. Included in the model that determines the open loop current is a finite element model to calculate the temperature field in the material. The shape of a frame consisting of SMA reinforced polypropylene beams has been controlled actively. The effect of the open loop term has been investigated in these experiments.

The control gain of the PI controllers is limited mainly by the behaviour of NiTi wires during transformation. This results in reduced tracking performance during elastic behaviour of the wires, because temperature changes have little effect there. Improved tracking performance was achieved for almost all systems, when an open loop term was added. The open loop term anticipates the lower sensitivity to temperature variations during elastic behaviour.

Samenvatting

De afgelopen jaren vinden we een groeiende aandacht voor materialen waarvan de eigenschappen tijdens gebruik actief kunnen worden aangepast aan de omstandigheden. Deze materialen hebben geïntegreerde actuatoren en/of sensoren en worden veelal aangeduid met *adaptive* of *smart*.

Bij de actuatoren spelen geheugenmetalen een belangrijke rol. Geheugenmetalen zijn in staat om een initiële vorm te onthouden en daarin na deformatie terug te keren bij temperatuurverhoging. Dit gedrag wordt veroorzaakt door een verandering van kristalstructuur. Eén van de meest gebruikte en onderzochte geheugenmetalen is een nikkel-titanium (NiTi) legering. Door de temperatuur van een onbelaste, vooraf opgerekte NiTi draad te verhogen, krimpt de draad tot z'n oorspronkelijke lengte. Op deze manier kunnen rekken tot 8% teniet worden gedaan. Als de opgerekte draad wordt ingeklemd tijdens verwarmen treden zeer grote spanningen (tot 800 MPa) in de draad op. Door dit gedrag kunnen geheugenmetalen in een willekeurige geometrie als actuator worden toegepast.

In het hier beschreven onderzoek zijn NiTi draden toegepast als actuator in een aantal mechanische systemen. De grootheid waarmee NiTi actuatoren worden aangestuurd is de temperatuur, die door middel van elektrische stroom kan worden voorgeschreven gebruikmakend van een regelwet. Bij de verschillende systemen zijn twee regelwetten toegepast. Allereerst alleen een PI regelaar, waarbij de elektrische stroom afhankelijk is van het verschil tussen de gewenste en gerealiseerde waarde van bepaalde variabelen. Vervolgens is hier een open loop term aan toegevoegd. Deze open loop term is de stroom die volgens een model van het totale systeem nodig is om het gewenste resultaat te bereiken. Een belangrijk onderdeel van dit model is het constitutieve gedrag van NiTi draden, dat de niet-lineaire relatie tussen spanning, rek en temperatuur van een draad beschrijft. Er is een constitutief model ontwikkeld, waarmee relatief eenvoudig elk van de drie constitutieve variabelen bepaald kan worden als de andere twee gegeven zijn. Het model is daardoor zeer bruikbaar bij het bepalen van de open loop term, omdat daar zowel spanning als temperatuur als onbekenden kunnen optreden. Het open loop model bevat ook het opwarm- en afkoelgedrag van het totale systeem en de mechanische en thermische interactie tussen draden en omgeving.

In eerste instantie is de aandacht gericht op drie systemen met één graad van vrijheid: een massa aan een NiTi draad, een veer in serie met een draad en twee in serie geschakelde NiTi draden. In de eerste twee gevallen krimpt de NiTi draad bij verhitten en trekt daarbij de massa omhoog c.q. rekt de veer uit. Bij het derde systeem wordt bij verhitten en daardoor krimpen van de ene draad de andere afkoelende draad uitgerekt. Dit principe is vervolgens toegepast op een robotvinger met twee rotatievrijheidsgraden, die elk worden geregeld door twee geheugendraden. Door de twee paar NiTi draden op de juiste manier te verhitten kan de vingertop een gewenste baan volgen.

Tenslotte is een balk ontwikkeld bestaande uit een polypropeen matrix met NiTi draden ingebed aan de boven- en onderzijde. Door een draad aan één zijde te verhitten treedt een grote spanning in de draad op, resulterend in een momentwerking, die buiging tot gevolg heeft. Een belangrijk verschil met de eerder genoemde systemen is dat de temperatuur van de draden aan beide zijden gekoppeld is door de warmtegeleiding in het matrixmateriaal. Het model waarmee de open loop stroom wordt bepaald bevat in dit geval een eindige elementen model om de temperatuurverdeling in het materiaal te berekenen. Er zijn experimenten uitgevoerd waarbij de vorm van een frame bestaande uit vier gekoppelde balken actief is geregeld. Ook hier is het effect van de open loop term onderzocht.

De versterking van de PI regelaars wordt met name beperkt door het gedrag van de NiTi draden tijdens transformatie. Dit resulteert in een slecht volggedrag van de geregelde systemen tijdens elastisch gedrag, omdat een geheugenmetaal daar nauwelijks reageert op een temperatuurverandering. Bij vrijwel alle onderzochte systemen werd een beter resultaat verkregen indien de open loop term werd toegevoegd. Dit komt vooral omdat de open loop term anticipeert op de lagere temperatuurgevoeligheid van geheugendraden tijdens elastisch gedrag.

Dankwoord

Aan dit proefschrift hebben een aantal mensen al dan niet bewust een zodanige bijdrage geleverd dat ik hen daarvoor op deze plaats wil bedanken.

Piet Schreurs heeft in de loop der jaren de grote lijn in de gaten gehouden, zodat ik me naar hartelust kon storten op allerlei details. Bij het schrijven van dit proefschrift waren de rollen omgekeerd. Samen met Frans Veldpaus heeft hij begrippen als 'helder' en 'bondig' extra betekenis gegeven.

Experimenten kosten veel tijd. Dat weten ook de inmiddels ex-studenten Marco Moens en Jasper Zuidervaart, die een groot aandeel hebben gehad in respectievelijk de hoofdstukken vier en vijf. Het heeft me veel voldoening gegeven deel uit te maken van het driekoppige Shape Memory Alloy Research Team.

De experimenten waren ook niet tot stand gekomen zonder de hulp van Toon van Gils, die de robotvinger bouwde, Karel Koekkoek, die er voor zorgde dat er stroom op de juiste manier door alle geheugendraden kon gaan, en Jos Banens, die het geheel op onnavolgbare wijze aan elkaar knoopte met software.

Bijdragen op geheel ander vlak zijn geleverd door mijn kamergenoten Annemarie, André, Carla, Jeroen, Lars en Paul. Zij zorgden vrijwel altijd voor een optimale (werk) sfeer, waarbij koffie en voor de dames thee een vooraanstaande rol speelden.

Leonardo, ti ringrazio per le lezioni piú o meno italiane-olandesi.

Mijn ouders wil ik graag bedanken voor het scheppen van de juiste randvoorwaarden gedurende vele jaren. Kort gezegd: huiswerk is belangrijker dan afdrogen.

Natuurlijk kan er maar één als laatste worden genoemd: Margot. Het feit dat zij het ontwerp van de omslag voor haar rekening heeft genomen valt in het niet bij haar andere bijdragen.

Bedankt allemaal!

<div align="right">

Marc van der Wijst
Veldhoven, 3 april 1998

</div>

Curriculum Vitae

January 16, 1969	Born in Nuenen, The Netherlands
1981-1987	Gymnasium β, Augustinianum, Eindhoven
1987-1993	Masters degree at the Department of Mechanical Engineering, Eindhoven University of Technology
1993-1998	Research assistant at the Department of Mechanical Engineering, Eindhoven University of Technology
February 1, 1998 -	Mechanical Designer at ASM Lithography, Veldhoven